ION BEAM WRITING AND MODIFICATION FOR INTEGRATED OPTICS

SUDHEER KUMAR VANGA

(M.Sc. UNIVERSITY OF HYDERABAD, INDIA)

A THESIS SUBMITTED

FOR THE DEGREE OF DOCTOR OF PHILOSOPHY

DEPARTMENT OF PHYSICS

NATIONAL UNIVERSITY OF SINGAPORE

2013

DECLARATION

I hereby declare that this thesis is my original work and it has been written by me in its entirety. I have duly acknowledged all the sources of information which have been used in the thesis.

This thesis has also not been submitted for any degree in any university previously.

Name: Sudheer Kumar Vanga
Date: 25 Janury 2013

Acknowledgements

It is with immense gratitude that I acknowledge the support and guidance from my supervisor Asst.Prof. Andrew Bettiol, without whom this thesis would be a dream. I am deeply indebted for his invaluable guidance and encouragement throughout the PhD career. His unwavering scientific enthusiasm and keen physical intuition have been a constant source of motivation and inspiration for me. His innovative ideas to introduce sessions like "crazy ideas" in group meetings made me think beyond the scope of my research and helped enhancing my creative thinking.

I had a great pleasure working with members of CIBA who made the lab environment friendly, caring and supportive. Firstly, I would like to thank Prof. Frank Watt and Assc. Prof. Thomas Osipowicz for leading the whole lab with their scientific and managerial expertise. I would also like to thank Prof. Mark Breese, Asst. Prof. Jereon van Kan and Dr. Chammika Udalagama for their willingness to help in any scientific problem.

I share the credit of my work with Dr. Teo Ee Jin, who first introduced me to proton beam writing facility and waveguide characterization set-up. Her expertise in the field and her scientific contribution motivated me to develop interest for ion beam writing in optical applications. I would also like to thank the research staff in CIBA, Dr. Piravi Perumal Malar, Dr. Chan Taw Kuei, Dr. Pattabiraman Santhana Raman and Dr. Ren Minqin for their support and helpful discussions. I would like to thank Mr. Choo Theam Fook and Mr. Armin Baysic De Vera for their contiguous help in the experimentation with accelerator facility.

With great pleasure I would like to thank my colleagues from OMAD, Dr. Yan Yuanjun, Mr. Shuvan Prashant Turaga, Mr. Yang Chengyuan and Mr. Choi Kwan Bum for making the lab lively all day with fruitful and helpful discussions. Special thanks to Mr. Shuvan Prashant Turaga and Mr. Choi Kwan Bum for proofreading my thesis.

I would like to extend my heart felt thanks to my senior students Dr. Siew Kit, Dr. Chen Xiao and Ms. Sara Azimi for their help and guidance in my experiments. I would also like to thank all my fellow students Ms. Xiong Boqian, Mr. Mallikarjuna Rao Motapothula, Mr. Liang Haidong, Ms. Dang Zhiya, Ms. Song Jiao, Mr. Wu Jian Feng, Mr. Wang Yinghui, Mr. Liu Fan, Mr. Yao Yong, Mr. Mi Zhaohong and Mr. Liu Nan Nan for providing me a positive working environment.

At this juncture I would like to acknowledge my collaborators Prof. Feng Chen from Shandong University, China, Prof. Aaron Danner from National University of Singapore, Singapore, Prof. Paolo Olivero from University of Torino, Italy and Dr. Soma Venugopal Rao from University of Hyderabad, India for giving me the opportunity to work with them. I would like to appreciate Dr. Venkatram Nalla for his technical assistance in laser characterization. I would like to thank Mr. Deng Jun for help in Lithium Niobate related work and Ms. Dang Zhiya and Mr. Liang Haidong for help in silicon micromachining.

I wish to thank all my friends from Singapore who made this PhD journey, an unforgettable memory. I would like to extend special thanks to Ms. GuruGirijha Rathnasamy and Mr. Shuvan Prashanth Turaga for their every day company and gratifying discussions which encouraged me to learn things beyond the research. I would also like to thank Dr. Venkatesh Mamidala, Mr. Anil Annadi, Mr. Durga Venkata Mahesh Repaka, Mr. Bharath Ramesh and Ms. Sandhya Chintalapati.

I would like to thank all my bachelors and masters degree friends for their support and encouragement. I am greatly thankful for everyone who supported me directly or indirectly during the course of PhD.

Finally, I would like to thank my family members for their support, encouragement and the freedom that they offered me to learn many things in life.

Contents

Abstract

Light ion beams (like hydrogen and helium) can be used for lithographically defining structures in resist, or for directly modifying materials. When used for lithography, focused proton beams are able to achieve structures with straight and smooth sidewalls with high aspect ratio, free from proximity effects.

The focused proton beam writing (PBW) was employed to fabricate optical components for integrated optics. A whispering gallery mode (WGM) microdisk resonator was fabricated using PBW and optically characterized at telecommunications wavelengths. We demonstrate that they can be potentially used as resonators and for wavelength filters. The same microresonator was fabricated in dye doped polymer to investigate active lasing under optical pumping. The microlaser designs based on circular WGM resonators showed omni-directional lasing which is undesirable for the practical applications. To make the WGM based microlasers directional, a variety of cavity designs were explored. Further, to improve the threshold input pump fluence, three dimensional suspended microlasers were also fabricated using PBW.

Ion beam irradiation was used to modify the optical characteristics of several single crystal materials. Optical waveguides were fabricated using PBW in single crystal type IIa CVD grown Diamonds and the waveguide characteristics, ion beam induced effects were characterized spectroscopically. The proton and helium ion beam writing was used to define optical waveguides and lasers in various nonlinear crystals. The performance of these optical components will be discussed in detail.

List of Tables

List of Figures

Abbreviations

AFM	**A**tomic **F**orce **M**icroscopy
APF	**A**ll **P**ass **F**ilter
CCD	**C**harge **C**oupled **D**evice
CEM	**C**hannel **E**lectron **M**ultiplier
CIBA	**C**entre for **I**on **B**eam **A**pplications
CMOS	**C**omplementary **M**etal **O**xide **S**emiconductor
CRIT	**C**oupled **R**esonator **I**nduced **T**ransparency
CROW	**C**oupled **R**esonator **O**ptical **W**aveguide
CVD	**C**hemical **V**apor **D**eposition
DAC	**D**igital to **A**nalogue **C**onverter
DAQ	**D**ata **AQ**uisition
DC	**D**irect **C**urrent
DIC	**D**ifferential **C**ontrast **I**nterference
DPA	**D**efect **P**er **A**tom
DPSS	**D**iode **P**umped **S**olid **S**tate laser
DUV	**D**eep **U**ltra **V**iolet
EBL	**E**lectron **B**eam **L**ithogrphy
FDTD	**F**inite **D**ifference **T**ime **D**omain
FEM	**F**inite **E**lement **M**ethod
FIB	**F**ocused **I**on **B**eam
FSR	**F**ree **S**pectral **R**ange
FWHM	**F**ull **W**idth at **H**alf **M**aximum
GBL	**G**amma **B**utyro **L**actone
HeBW	**H**elium **B**eam **W**riting
HF	**H**ydro **F**luoric acid
HRBS	**H**igh **R**esolution **RBS**
HVEE	**H**igh **V**oltage **E**ngineering **E**uropa
ICP	**I**nductively **C**oupled **P**lasma

IR	**I**nfra **R**ed
KeV	**K**ilo **e**lectron **V**olt
LED	**L**ight **E**mitting **D**iode
LN	**L**ithium **N**iobate
MEMS	**M**icro-**E**lectro-**M**echanical **S**ystems
MeV	**M**ega **e**lectron **V**olt
MV	**M**ega **V**olt
NA	**N**umerical **A**perture
Nd:YAG	**N**eodymium doped **Y**ttrium **A**luminum **G**arnet
NIL	**N**ano **I**mprinting **L**ithography
NIR	**N**ear **I**nfra **R**ed
NV	**N**itrogen **V**acancy
OM	**O**xford **M**icrobeams
OPO	**O**ptical **P**arametric **O**scillation
PBW	**P**roton **B**eam **W**riting
PEB	**P**ost **E**xposure **B**ake
PIF	**P**roton **I**nduced **F**luorescence
PIXE	**P**article/textbfProton **I**nduced **X**ray **E**mission
PL	**P**hoto **L**uminescence
PMMA	**P**oly **M**ethyl **M**eth **A**crylate
RBS	**R**utherford **B**ackscattering **S**pectroscopy
RF	**R**adio **F**requency
Rh6G	**R**hodamine **6G** laser dye
RhB	**R**hodamine **B** laser dye
RIE	**R**eactive **I**on **E**tching
SEM	**S**canning **E**lectron **M**icroscopy
SHG	**S**econd **H**armonic **G**eneration
SIMNRA	A **SIM**ulation program for **N**uclear **R**eaction **A**nalysis
SRIM	**S**topping and **R**ange of **I**ons in **M**atter
SRR	**S**plit **R**ing **R**esonator
STIM	**S**canning **T**ransmission **I**on **M**icroscopy
TE	**T**ransverse **E**lectric
TM	**T**ransverse **M**agnetic
UV	**U**ltra **V**iolet
WGM	**W**hispering **G**allery **M**ode
ZPL	**Z**ero **P**honon **L**ine

Symbols

ω_0	laser beam waist	μm
E	average laser energy	J
F	pump laser fluence	μJ/mm^2
ϕ	ion fluence	ions/cm^2
α	absorption loss coefficient	cm^{-1}
λ	wavelength of the light	nm
R	radius of microresonator	μm
n	refractive index	
Q	quality factor	
m	azimuthal mode number	
L	propagation loss	dB/cm
Θ	angular deflection	degree

Dedicated to my family and friends

Chapter 1

Introduction

Proton beam writing (PBW) was first developed at the Centre for Ion Beam Applications (CIBA), National University of Singapore in 1997 [1, 2]. A beam line dedicated to lithography was later developed in 2003. In the years since commissioning of the PBW beam line, continuous improvements have been made to the system, including the beam resolution. The current state-of-the-art resolution is 25 nm [3]. These improvements have made PBW useful for a variety of applications, including optics and photonics applications [4–8]. Currently the technique has matured and many optical components have been fabricated in the last decade by both researchers at the CIBA and in other groups. Various materials have been used for optical components. However the majority of the structures that have been fabricated using PBW have been passive optical elements made in polymer [9].

Direct write lithography and materials modification using light ions has some unique features that sets it apart from other forms of lithography. In particular, PBW has attracted increasing interest in recent years due to its ability to fabricate high aspect ratio, high density three dimensional micro/nano structures that are free from proximity effects. This makes PBW an attractive technique when it comes to fabricating structures for optical applications.

In the field of integrated optics, whispering gallery mode resonators have attracted a lot of research in recent years because of the high quality factors that can be achieved, and the potential applications [10–12]. These high-Q microresonators can be fabricated in different materials including low index contrast materials such as polymers [13].

The work in this thesis is motivated by the fact that PBW has the unique capability of being able to fabricate smooth 3D structures at the micro and nano level. PBW has been used to fabricate optical microresonators based on whispering gallery mode resonators in polymer. The microresonators are integrated with optical waveguides and doped with laser dyes for integrated optics applications. Three dimensional microresonators were fabricated by making use of the fact that an ion beam has a well defined range in a material that depends on its energy which could be varied in order to precisely irradiate different depths of material, thus allowing for 3D fabrication.

Ion beam writing (H and He) is also employed for the modification of the optical properties of materials. As MeV ions has precise range in a material, a region at the end of range of ion's path can be modified (change in refractive index [14]) in order to make optical components like waveguides and the waveguide lasers. Due to emerging applications in the field of diamond photonics, particular emphasis is placed on the fabrication of waveguides in single crystal diamond [15, 16]. Various experiments were performed to better understand the mechanism for refractive index modification in diamond, including detailed propagation loss measurements that have been performed for the first time in such structures.

1.1 Objectives

The objective of this thesis is to make use of the unique capabilities of PBW for the fabrication of novel active optical devices that have potential applications in integrated optics. Based on this the major aims in this thesis are

- The fabrication and the optical characterization of whispering gallery mode microresonators in polymeric materials. Making use of the unique properties of the PBW technique to achieve optical grade smoothness in the microresonator structures. Also to realize the suspended microresonators in different (both polymer and non-polymer) materials through proton and helium beam writing.
- Utilizing the microresonator structures to fabricate microlasers from laser dye doped polymers and to characterize their emission properties. Study various cavity designs to achieve directionality in WGM microlasers and attempt to reduce the threshold pump fluence in the case of directional cavities.
- To fabricate and characterize buried waveguides in single crystal substrates. To investigate the effects caused by the ion implantation and to understand the fundamental mechanisms for the change in refractive index. Utilize the implantation method for making active devices such as waveguide lasers.

1.2 Thesis organization

The thesis focuses on applications of microstructures fabricated using PBW and making use of such structures in the field of integrated optics. Chapter 2 describes in detail the CIBA accelerator facility and the PBW fabrication procedure. This chapter also discusses the current status of PBW at CIBA and reviews the past research work related to the field of optics and photonics. Chapter 3 presents a

brief review on whispering gallery mode resonators which includes theory, commonly used lithographic techniques for the fabrication and some of the applications based on WGM resonators. The coupled mode theory is implemented to obtain the important resonator parameters and reviews the performance of the WGM resonators. Chapter 4 illustrates the fabrication of planar WGM microdisk resonators in SU-8 polymer using PBW. Optical characterization of the microdisk resonator in the telecommunication band revelaed that high quality factors could be achieved from the PBW fabricated polymer microresonators. The chapter also discusses one of the applications of WGM microcavities, which is microdisk lasers made from the laser dye doped SU-8 polymer. Laser emission from the commonly used circular whispering gallery mode microlasers are omni-directional which is the main limitation for such high quality factor microlasers. Novel designs of WGM resonators are implemented to achieve directionality in the WGM microlasers. Chapter 5 discusses the fabrication of suspended three dimensional microcavities in various materials using ion beam techniques. The suspended microlaser characteristics are obtained and a comparison is drawn between the planar and the 3D microlasers of different designs of the laser cavity. Chapter 6 concentrates on the optical modification of single crystal materials by direct ion beam writing. The ion implanted region in certain single crystal materials (diamond, KTP and Nd:GGG) showed an increase in refractive index which helps to form buried channel waveguides. Also a waveguide laser is demonstrated from the waveguide formed in Nd:GGG crystal. Chapter 7 summarizes and concludes the work with some future directions and goals.

Chapter 2

Proton beam writing

Proton beam writing (PBW) is a direct write ion beam based lithographic technique capable of fabricating micro/nano structures, particularly well known for polymer microstructures. PBW uses high energy protons (MeV) for fabrication. Such high energy protons penetrate deep (several 10's of microns) into a material enabling fabrication of high aspect ratio structures. Microstructures fabricated with PBW have smooth and straight sidewalls. Three dimensional structures can also be fabricated with PBW using different ion energies. The sub-micron focused proton beam is capable of patterning different materials such as polymers, semiconductors and inorganic crystals. All these advantages made the technique applicable for fabricating variety of micro/nano structures for various applications including optics and photonics. This chapter describes the details of PBW facility at the Centre for Ion Beam Applications (CIBA) followed by a discussion on previous work done using PBW. Emphasis is given for the applications in the field of optics and photonics.

2.1 Centre for Ion Beam Application (CIBA)

High energy (100 keV - 3.0 MeV) ion beams of hydrogen and helium ions from Singletron accelerator are used for different applications at CIBA [17–21]. There are a total of five beamlines that are currently in operation, located at 10°, 20°, 30°, 45°, and 90° to the ion beam direction after the analyzer magnet. A switcher magnet has been placed in the path of the ion beam after the analyzer magnet that can deflect the ion beam to + or - 45°. Using this switcher magnet the beam is deflected to 10°, 20°, 30°, 45° beamline target chambers. The 90° beamline is constructed by introducing another switcher magnet in the path of the 45° beamline. Each beamline in CIBA has been optimized for a different application. The 10° beamline is a proton beam writer dedicated to lithographically defining micro/nano structures for different applications like microfluidics, optics and photonics. Most of the work in this thesis was performed using the 10° beam line. The 20° beamline is the second generation proton beam writer. It is designed and constructed to obtain a beam spot size of 10 nm in both horizontal and vertical directions. The 30° beamline is a cell and tissue imaging ion microscope and is specifically designed and constructed for cell imaging using ion beams at sub-diffraction limited resolutions. Material characterization using Rutherford back scattering spectroscopy (RBS), ion channeling experiments and the large area ion implantation is performed regularly on the 45° beamline which has a nuclear microscope. The 90° beamline is a dedicated high resolution RBS (HRBS) facility. Using this a 0.9 keV FWHM energy resolution RBS spectrum can be obtained for thin film material. A schematic diagram and the top view image of the accelerator facility can be seen in Figure 2.1.

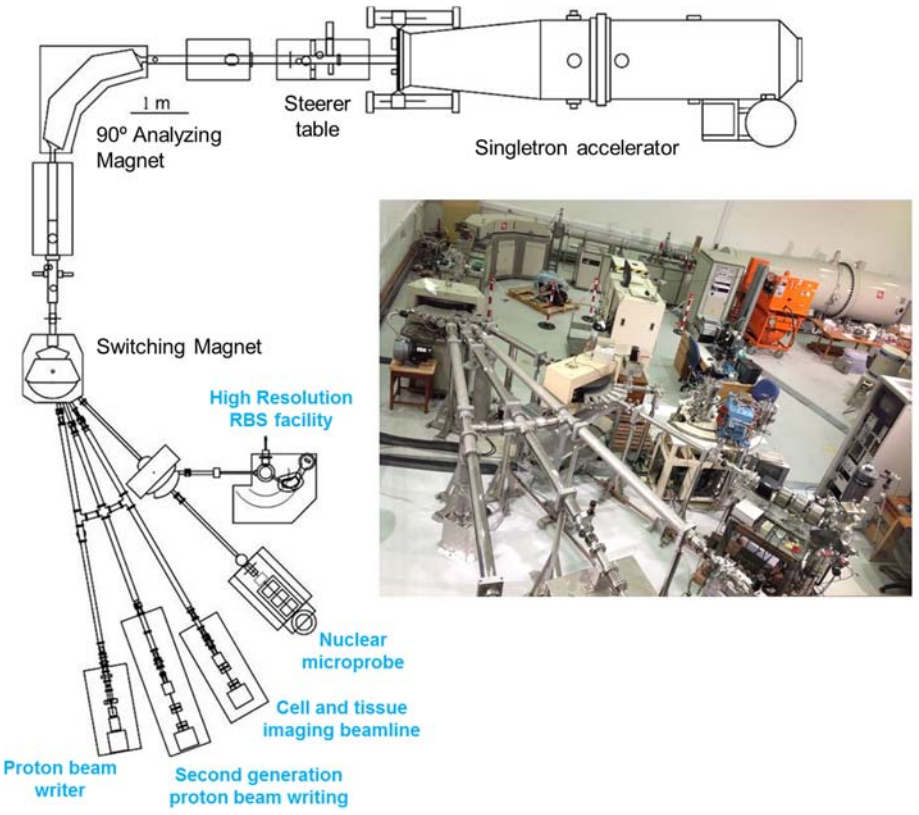

FIGURE 2.1: Schematic of the accelerator facility at the CIBA showing all the beamlines along with picture of the accelerator facility

2.2 Basics of Ion solid interactions

When an energetic ion beam enters a material it undergoes a series of collisions with target nuclei and electrons. In this process the energetic ion loses energy by transferring its kinetic energy to the nuclei and electrons of the target [22]. The main mechanisms of ion energy loss are electronic energy loss and nuclear energy loss.

Electronic energy loss:

The incident ions lose energy by inelastic collisions with target electrons, for which the incident ion excites or ionises the target electrons. This process causes small energy loss and negligible deflection of ion trajectory.

Nuclear energy loss:

The incident ions lose energy by elastic collisions with target nuclei which results in large discrete energy loss and significant deflection in ion trajectory.

Consider an ion with initial energy E_0 incident on the target material, upon traversing a distance of Δx in the material loses an energy ΔE. The amount of energy loss depends on material density, ion species and energy. The energy loss of the ions is commonly referred as stopping power $S = \frac{1}{N}(dE/dx)$. The total stopping power can be written as

$$S = \frac{1}{N}\frac{dE}{dx}|_{electronic} + \frac{1}{N}\frac{dE}{dx}|_{nuclear} \tag{2.1}$$

where N is the density of the target material.

The energy loss process primarily depends on the velocity of the ion. For velocities less than the Bohr velocity of the atomic electrons v_0, ions become neutralized by capturing electrons from the solid, and nuclear stopping dominates. For higher velocities the nuclear stopping decreases by $(1/E)$ and the electronic stopping dominates. At high energy, the electrons on the ion are stripped by the sample and the process of energy loss can be modelled by assuming that interactions between the incident ion (of mass M_1, charge Z_1e and velocity v_1) and a stationary sample atom (of mass M_2 and charge Z_2e) only slightly perturb the trajectory of ion. If this is the case, momentum transfer occurs perpendicular to the particle direction. The well known result for electronic stopping calculated by Bethe and Bloch [23, 24] is given by the formula

$$\left(\frac{dE}{dx}\right)_e = NZ_2\left[\frac{4\pi(Z_1e^2)^2}{m_e v_1^2}\right]L, \tag{2.2}$$

where L is the stopping number which is calculated by Bethe quantum mechanically as

$$L = ln(2m_e v_1^2/I) \tag{2.3}$$

In equation 2.3, I is the energy averaged over the excitations and ionisations of the electrons of the sample atoms.

The rate of energy loss of a fast charged particle (proton or electron) does not depend on its energy but on its velocity ($\frac{dE}{dS} \propto \frac{z^2}{v^2}$). Although the same velocity proton or electron will suffer the same energy loss, the kinetic energy of the electrons depletes more quickly compared to that of protons since the electron mass is much less when compared to proton. Since the elastic scattering cross-sections supposed to be larger at low energies, the electrons tend to participate in more scattering which results in high proximity effects compared to protons.

The ions that penetrate the material eventually comes to rest inside the sample as the cross-section for large angle Rutherford scattering to occur is small. The average depth at which the ions comes to rest inside the material is called the ion range R is given by

$$R = \int_0^{E_0} \left(\frac{dE}{dx}\right)^{-1} .dE \tag{2.4}$$

2.3 Proton beam writing facility

The proton beam writer, 10° beamline is designed and constructed for applications of the PBW method. A typical PBW procedure and the working principles behind some of the important components are discussed in this section.

2.3.1 Accelerator

The high brightness proton beam is generated from the radio frequency (RF) ion source containing hydrogen gas, which is placed inside the 3.5 MV High Voltage Engineering Europa (HVEE) Singletron™ ion accelerator [25]. The ion source is excited by a radio frequency oscillator capacitively coupled to the gas bottle. The output from the ion source is optimized by controlling the source gas pressure and oscillator load. The HVEE Singletron™ accelerator tube is constructed by sandwiching titanium electrodes between the circular glass insulator rings. These

electrodes have a central hole through which the high brightness ion beam passes through. The high voltages in this accelerator are generated electronically using the Cockroft-Walton voltage multiplier circuit which consists of ladder network of capacitors and diodes. When the AC power supply given to this circuit, the orientation of the network of diodes causes the capacitors to be charged up during the half cycle and for the other half cycle the diode acts as open circuit and the capacitors are effectively in series. At each step the potential adds up to the final terminal voltage over the series of charged capacitors [26]. This particular particle accelerator has high energy stability compared to single-ended accelerators such as Van De Graaff accelerators, which is one of the prerequisites for PBW.

2.3.2 Beamline

The positive ion beam is extracted from the ion source and is accelerated. A 90° analyzer magnet is used to bend the accelerated ion beam towards the switcher magnet which is placed in a perpendicular direction to the Singletron accelerator and after the object slits. The magnetic field generated by the analyzer magnet selects the different species of the ion beam, in case of the hydrogen gas proton beam H^+ or molecular beam H_2^+. To monitor the beam current at different locations along the beam path, from the accelerator to the switcher magnet, Faraday cups are incorporated in the beam path. Faraday cup 1 is placed after the beam steerers and Faraday cup 2 is placed before the switcher magnet. To centralize the beam in the beam pipe a beam profile monitor is placed after the 90° analyzer magnet. Two sets of object slits in both X and Y directions are placed in the beam path to adjust the beam size. After the object slits, the ion beam enters the switcher magnet from where we direct the ion beam to different beamlines. The 10° beamline consists of a set of collimator slits, magnetic quadrupole lenses for the focussing of the ion beam, electrostatic and magnetic scanning system and the target chamber which consists

of three axis translational stage and various detectors. The Figure 2.2 shows the end station of 10° beamline.

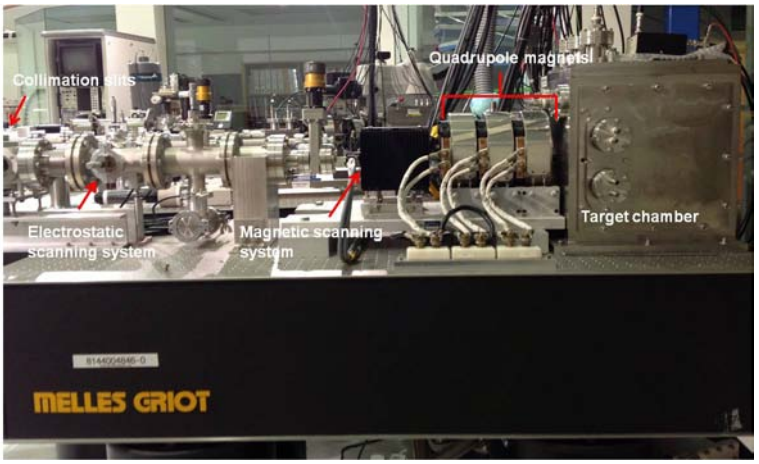

FIGURE 2.2: The picture shows the end station of the 10 degree beamline with different components indicated

2.3.3 Target chamber

The target chamber at the end station of the 10° beamline is routinely operated under vacuum less than 1.8×10^{-5} *mbar*. The target chamber is custom made with several detectors placed inside for specific purposes. The inside view of the target chamber is shown in Figure 2.3. The target chamber and the focusing system are installed on an optical table to minimize the vibrations during the experiment. The sample along with a quartz target that is used to observe and focus the beam, and a Ni grid used for measuring the beam focus, are placed on the sample holder which is mounted onto a computer controlled Exfo Inchworm XYZ translational stage. The translational stage is capable of travelling 25 mm in each direction with a step resolution of 20 *nm*. An annular RBS detector is mounted in the beam path to collect the backscattered ions at a scattering angle of 170° from the sample. This detector is connected to a preamplifier which is placed outside the chamber. The preamplifier is then connected to data acquisition hardware in order to digitize the

FIGURE 2.3: The interior view of the proton beam writer target chamber (1) annular RBS detector placed in the path of the proton beam (2) CEM detector to collect the secondary electrons induced by the proton beam upon interacted with the sample, which uses for imaging (3) XYZ piezo translational stage on which the sample holder is mounted (4) Optical microscope to view the sample for sample alignment during the experiment (5) LED light illumination for the microscope

information. A channel electron multiplier (CEM) detector is placed in the chamber to collect the proton induced secondary electrons with which the Ni grid is imaged to calculate the spot size of the proton beam. An optical microscope connected to a CCD camera is also installed to monitor the position of the sample. Sample illumination is achieved using an array of yellow LEDs placed inside the chamber.

2.3.4 Focusing system

The proton beam is focused using three compact magnetic quadrupole lenses (Oxford Microbeams OM52) arranged in the Oxford Triplet configuration [27]. The

quadrupole lenses are installed before the target chamber and are placed on a vibration isolation optical table. Three individual quadrupole lenses are arranged in a converging-diverging-converging configuration with the first two lenses connected so as to carry the same current. The present quadrupole lens system in the proton beam writer beamline is operating with an object aperture distance of 6.4 *metres* from the lens system. The image plane is 70 *mm* from the lens system. With this geometry the beam transmitted through the object aperture experience a demagnification factor of 228 in the horizontal direction and 60 in the vertical direction. With this quadrupole configuration, the first world record spot size 35 $nm \times 75\ nm$ was achieved [28] in 2003.

2.3.5 Scanning system

For patterning complex structures using these focused proton beams, a beam scanning sytem is required. In order to pattern different structures two different scanning methods were used.

2.3.5.1 Beam scanning

Beam scanning can be achieved in two ways, one is by applying the magnetic field to scan the beam and the other to use the electric field to control the beam scanning. In the current 10° beamline we generally employ magnetic scanning to control the beam path with a set of magnetic scan coils which are conveniently placed outside the vacuum, just before the quadrupole lenses. The currents applied to these scan coils are controlled by OM40e scan-controller. However the speed at which the proton beam can be scanned laterally across the sample is limited due to hysteresis in the magnetic scan coils [29]. To solve this issue, an electrostatic scanning system is incorporated in the beam path. An improvement of two orders of magnitude in

the scanning speed [30] is achieved by using electrostatic scanning. Using these scan systems the proton beam can be scanned in an area of 0.6×0.6 mm^2.

2.3.5.2 Stage scanning

Although beam scanning can be employed for patterning structures with PBW, there is a limitation to the scan area. Beam scanning can be used to pattern scan fields upto 0.6×0.6 mm^2, and stitching can be employed to join the scan fields to make larger structures. This scanning method suffers from stitching errors and can cause discontinuities in the structures. This is especially undesirable for optical components as it causes large scattering losses. To solve this issue and to fabricate longer structures like waveguides with lengths greater than 1 cm, stage scanning was introduced. For stage scanning, the sample stage is moved in one direction (either horizontal or vertical) and the beam is magnetically scanned perpendicular to the direction in which the stage moves [31]. In this method the structure length is only limited by the stage translation.

2.3.6 Beam blanking system

For the fabrication of complex structures a flexible beam scanning system alone is not sufficient. When the desired structure has discontinuities, a method of rapidly deflecting the beam is required in order to avoid unwanted exposure of the resist. To gain control over the scanning, an electrostatic blanking system has been employed to deflect the proton beam from its path which allows the beam on and off at will. To deflect the proton beam, a strong electrostatic field is applied between two plates positioned close to the switcher magnet. The power supply for the electric field is a fast switching amplifier that can be turned on and off remotely by computer, allowing fast beam blanking [29].

2.3.7 Software Control

To control the scanning of proton beam on the sample, a home built software IonScan has been used which was developed at CIBA [32]. The IonScan suite of programmes is developed using the C++ programming language in the dotNET environment. IonScan controls the scan amplifier and the blanking system, while monitoring the beam current. The information of the desired patterns for irradiation are included in the "EPL" file format which is defined solely for IonScan. The IonScan suite also has a software component called IonUtils which can be used to convert files of different formats to the EPL format. Bitmap files and the text files which contain the information of the coordinates to be irradiated can be converted to EPL file format using IonUtils. IonUtils can also be used to generate some basic scan patterns. Stage control is also included in the program which provides the flexibility to use the software for the stage scanning as well. This software also reads multiple EPL files for batch exposure. The IonScan software suite is the backbone of the proton beam writing process. It is responsible for all aspects of PBW and file conversion processes including beam scanning, beam blanking, stage scanning and control, dose normalization and batch exposure.

The hardware controlled by IonScan includes computer data acquisition (DAQ) cards from National Instruments. Presently IonScan is using either 16 bit PCI 6731 or the 12 bit 6711 cards. Using these cards the IonScan controls the beam manipulation, beam blanking and the signal normalization. The digital to analogue (DAC) converters on the card are utilized for beam movement and blanking, and a counter for signal monitoring and normalization.

2.3.8 Dose Normalization

The proton dose normalization can be performed in several ways. The commonly used method is by calibrating the back scattered ions. In each experiment a section

of the sample is used to collect the RBS spectrum and this spectrum is fit to a theoretical curve using the SIMNRA software package. It allows the user to obtain the ions-steradian information. A typical RBS spectrum of 5 μm thick SU-8 on SiO_2/Si substrate can be seen in Figure 2.4. The annular RBS detector in the 10° beamline has a solid angle of 62 msr. From the incident number of protons and the backscattered counts a calibration constant can be calculated. From the area of irradiation and the fluence required one can calculate the number of protons required for the irradiation. This proton number multiplied by the calibration factor gives the backscattered counts required per unit time during the experiment. Other methods that can be used to calculate the fluence include the direct measurement of incident protons using a PIN a diode (STIM) for very low proton current, or Ionoluminescence [33].

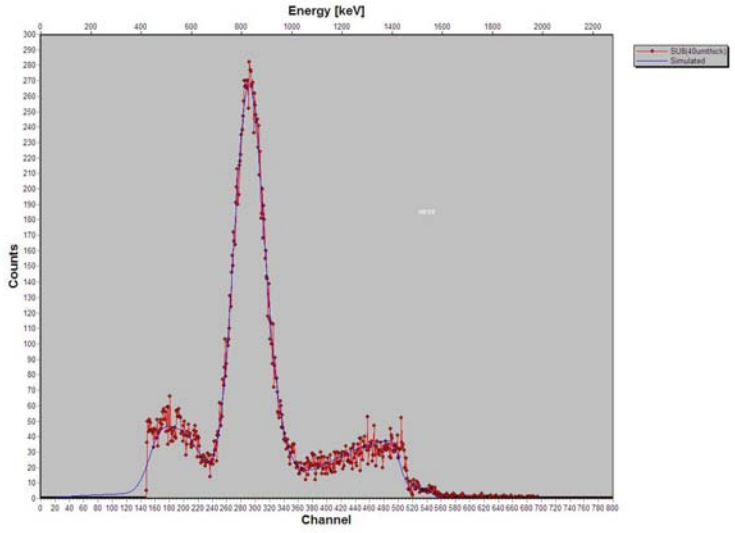

FIGURE 2.4: The RBS spectrum of 5 μm thick SU-8 collected using the annular RBS detector and is fit with SIMNRA software program

2.4 State-of-the-art performance

The proton beam writer in the 10° beamline is currently utilizing a focusing system which consists of a set of three high excitation quadrupole lenses (OM52-Oxford

Microbeams) for high demagnification. With this system the world record beam spot size of 35 nm× 75 nm was achieved. The next generation proton beam writer consists of four magnetic quadrupole lenses which are positioned in such a way that they can be quickly rearranged to test different lens configurations. The new system can be seen in Figure 2.5. The current performance test using a spaced quadrupole triplet configuration has set a new world record proton beam spot size of 19 nm × 29.9 nm [3]. The quadrupole magnetic lenses are arranged to obtain a high system demagnification. The current system has demagnification of 857 × 130 in X and Y respectively. The proton beam spot sizes can potentially be further reduced to sub-10 nm with further optimization.

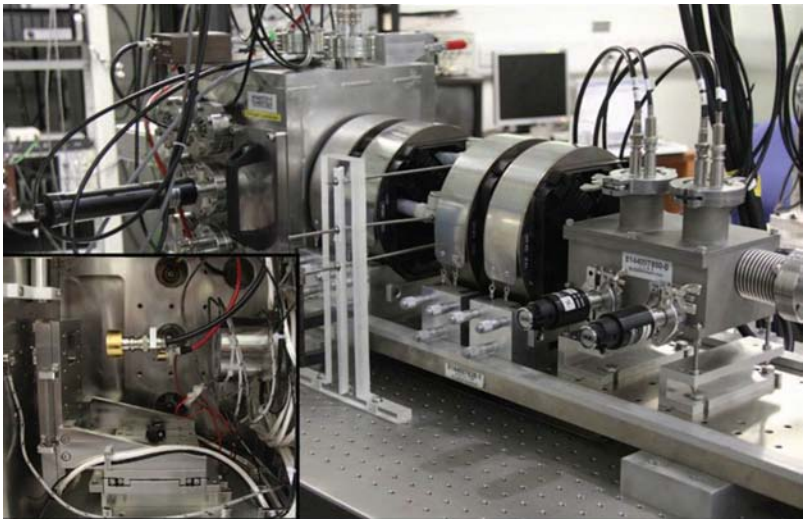

FIGURE 2.5: The image showing the next generation proton beam writer with the electrostatic scanning system and the focusing system consists of four magnetic quadrupole lenses, the inset is the inside view of the target chamber

2.5 Comparison with other fabrication technologies

It is useful to compare PBW with other established fabrication technologies in order to better appreciate the unique capabilities of PBW. A comparison is made between

proton beam writing, focused ion beam milling, electron beam lithography and photolithography (shown in Figure 2.6) [34]. The figure shows simulations carried out with different radiation on PMMA photoresist. It is clear from the figure that the proton beam can go deeper in the material without much proximity effects when compared to other fabrication techniques. In case of focused ion beam milling the surface layer is milled and some of the heavy ions used in the process redeposit on the material, in case of electron beams the electrons can not penetrate deep into a material since the electron-electron interactions cause large scattering. EBL is therefore not suitable for high aspect ratio structures. Though in photolithography and X-ray lithography the exposed radiation can reach deeper in the material, the exposure is nonuniform. From this simulation, it can be concluded that proton beam writing is ideal for the fabrication of high aspect ratio structures. Aspect ratios of 160 have been achieved [35] using PBW in photo resist SU-8.

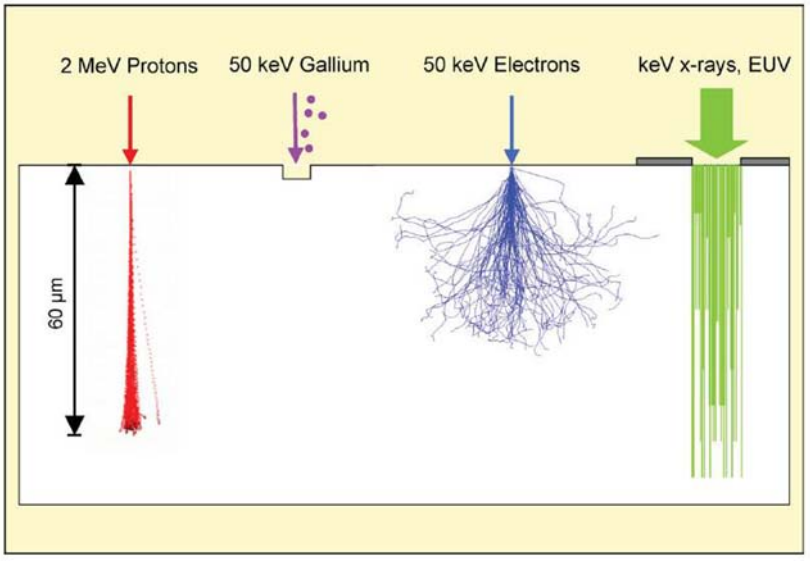

FIGURE 2.6: Comparison of the PBW with other fabrication technologies, image taken from [34]

The basic parameters of interest for any lithography are (1) surface quality of the fabricated structure, (2) mass producibility, (3) resolution of the technique, (4) ease of use and (5) post processing compatibility.

(1) Surface quality of the fabricated structure:

PBW is capable of producing straight and smooth sidewall structures in polymers. The atomic force microscopy measurements performed on the sidewalls of the microstructures fabricated using PBW revealed the sidewall roughness as low as 3.8 nm [36].

(2) Mass producibility:

Proton beam writing itself is limited in terms of the mass producibility because of the limitation of the beam scan area and the stage translation. The proton beam written microstructures can be replicated using electroplating and nanoimprinting techniques [37]. The electroplating technique generates the inverse structures produced by PBW in the metal (typically Nickel) and this metal can act as mold for nanoimprinter. The Ni mold can be used to mass produce the desired microstructures using nanoimprinting technique.

(3) Resolution:

As mentioned earlier, proton beams can be focused using magnetic quadrupole lenses to spot sizes as low as 35 $nm \times 75$ nm using the current facility at the 10° beamline. The next generation proton beam writing facility aims to achieve spot sizes below 10 nm. Presently the beam spot size of 19 $nm \times 29.9$ nm has already been achieved.

(4) Ease of Use:

Currently the proton beam writing is limited to the dedicated facilities which have accelerators. Although the focusing system and automation of the PBW is well established there are no commercial proton beam writing systems available in the market due to the lack of high brightness ion sources. Research on achieving the high brightness sources is currently in progress [3].

(5) Post processing compatibility:

PBW is applicable to a variety of materials which requires different post fabrication processing to achieve the final microstructures. PBW is compatible with the existing post processing facilities. in case of the polymers chemical development is required, whereas for the silicon electrochemical etching is required. These post

processing methods are widely used in CMOS technology [38].

Although the proton beam writing is lagging behind the other fabrication techniques when considering the resolution and ease of use, it has the potential to overcome these drawbacks in the near future. Apart from these considerations, PBW has several advantages over conventional lithographic techniques. It is a maskless lithographic technique and protons create damage in the material which can result in a change in the material's electronic, magnetic and optical properties. So PBW is not just limited to lithography but is also capable of material modification.

2.6 Previous work in photonics

Proton beam writing has been used to fabricate a variety of optical components in different materials, polymers being the main interest. Some of them are discussed in this section.

2.6.1 Optical waveguides

Any integrated optical circuit requires basic components like waveguides for the transfer of information within the chip. Optical waveguides have been fabricated in different materials using PBW. Optical channel waveguides were fabricated in polymer SU-8 and in silicon. A low propagation loss of 0.19 dB/cm [31] was achieved as a result of the smooth sidewall characteristics of the proton beam written waveguides in SU-8. A variety of waveguides have been fabricated in silicon with the aid of different ion energies and fluence. An extensive study was done to optimize the propagation loss. A loss as low as 1 dB/cm has been achieved. Channel waveguides fabricated in silicon on oxidized porous silicon showed a propagation loss of 1.1 dB/cm [39] and all silicon single mode Bragg cladding waveguide showed propagation loss of as low as 0.7 dB/cm [40]. Protons of two different energies were utilized

to fabricate free standing waveguides in silicon with the support from the substrate [41]. All these waveguides can be seen from Figure 2.7.

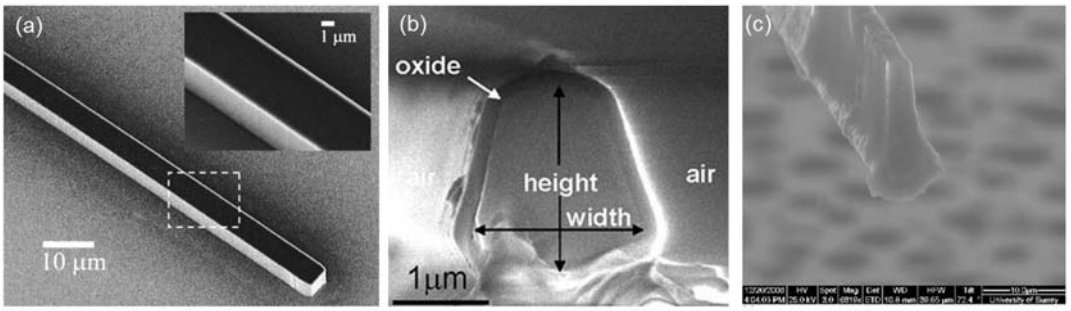

FIGURE 2.7: Channel waveguides fabricated in (a) SU-8 photoresist (b) silicon (c) free standing waveguide fabricated in silicon using two different proton energies

Proton beam writing was utilized to modify the material optically to form the buried waveguides in the polymer PMMA and in Forturan glass material [42]. The buried waveguides formed in PMMA allowed single mode propagation with refractive index increment reported in the range of 3×10^{-3} [14] and showed a propagation loss of 1.4 dB/cm [43]. Similarly an increase in refractive index of 1.6×10^{-3} and waveguide propagation loss of 8.3 dB/cm were reported in case of the Forturan glass [44]. The buried waveguides in PMMA and Forturan glass and the corresponding optical mode can be found in Figure 2.8.

2.6.2 Optical gratings

Optical gratings were fabricated successfully in both positive and negative photoresists, PMMA and SU-8 [45, 46]. The gratings with varied line spacing and line width were fabricated in the same resist for different film thickness. Figure 2.9(a) shows the grating with line width of 700 nm with a line spacing of 500 nm in 800 nm thick photoresist, Figure 2.9(b) shows the same grating in 2 μm thick PMMA

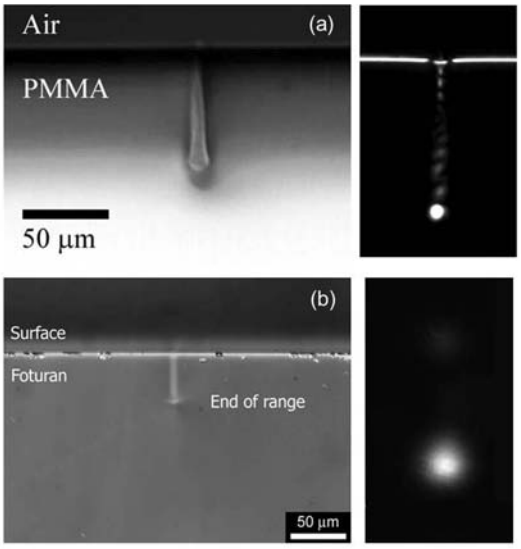

FIGURE 2.8: Buried waveguides fabricated in (a) PMMA and (b) Forturan glass along with their propagating mode in the waveguide

resist with a grating line width of 590 nm and line spacing of 390 nm. The Figure 2.9(c) shows the same grating in 1 μm thick SU-8.

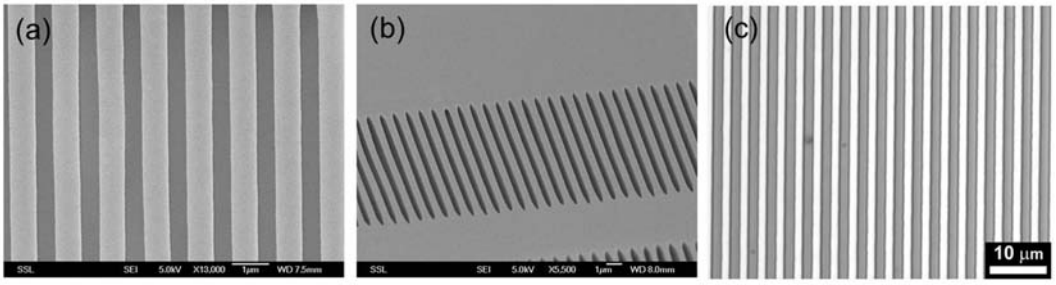

FIGURE 2.9: Optical gratings fabricated in positive resist of different thickness and the grating parameters (a) grating with 700 nm line width and 500 nm line spacing on 800 nm thick resist (b) grating with line width 590 nm and a spacing of 390 nm in 2 μm thick PMMA resist and (c) grating formed in 1 μm thick negative resist SU-8

2.6.3 Microlens array

Microlens arrays were generated in 4 μm thick PMMA. For the fabrication of the microlens, first PBW was performed on PMMA to make the micropillars of 20

μm diameter cylindrical structures. Once the structures were fabricated in PMMA and the sample was heated above the glass transition temperature of the polymer. The polymer starts to reflow and forms the spherical microlens because of the surface tension. The optimized maximum temperature used for the fabrication of the microlens array in PMMA is 200 °C. The fabricated microlens array can be seen from Figure 2.10. Depending on the diameter and thickness of the microlens, the focal length can be controlled [34] which gives the freedom to fabricate the desired microlens in an array [47].

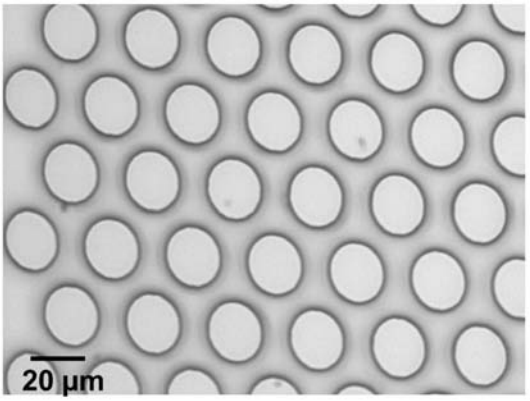

FIGURE 2.10: Microlens array formed in PMMA fabricated with PBW and thermal reflow technique, the figure shows the optical micrograph of the fabricated micro lens of 20 μm diameter in 12 μm thick PMMA

2.6.4 Metamaterials

Metamaterials is an interesting field in which the optical properties of a material result from its physical structure rather than the material characteristics. Metamaterials are artificial structures with engineered electromagnetic properties [48]. These structures are typically composed of an array of sub-wavelength metallic structures with strong electromagnetic resonances at specific wavelengths which can be designed using commercial software packages. Split ring resonators (SRR) are the basic design used for many metamaterials. They consists of two concentric

conducting rings each split by a gap situated oppositely, as illustrated in Figure 2.11. The SRR structures were fabricated using PBW together with gold electroplating [49]. PBW was used to fabricate the latent image of the SRR in 12 μm thick PMMA on metalized silicon substrate. This PMMA latent image serves as the template for gold electroplating. After electroplating, the seed layer is removed using chemical etching which leaves the gold SRR as shown in Figure 2.11. High aspect ratio SRR structures fabricated using PBW and electroplating were utilized to tune the resonance frequencies of the fabricated SRR with applied dielectric over layer ($\epsilon = 2.7$). The resonance was observed to shift from 640 GHz by nearly 120 GHz. This property can be useful for sensing applications [50].

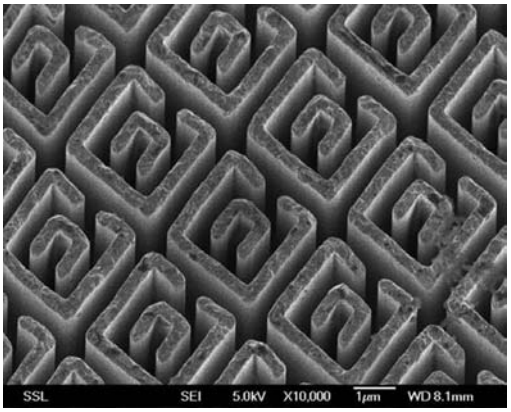

FIGURE 2.11: The figure shows the fabricated high aspect ratio Au SRR fabricated using PBW together with electroplating

Chapter 3

Review of optical microresonators

Whispering gallery modes (WGM) are specific modes of a wave field that are confined along the circumference of the resonator with smooth edges. The whispering gallery modes circulate along the resonator boundary as a result of continuous total internal reflection occurs at the boundary of the resonator. Due to this high confinement of the wave field, these resonators possess exceptional properties such as ultra-high quality factors, narrow resonance linewidths, small feature sizes and operation at optical wavelengths. Because of these incredible properties, WGM resonators are found in a plethora of applications. Their ability to operate at optical wavelength and the feasibility of smaller sizes using advanced fabrication techniques enables the on chip integration of WGM resonators. In this chapter, a brief review of WGM resonators and coupled mode theory applied to such resonators, general fabrication methods and some applications is presented.

3.1 Whispering gallery modes

Whispering gallery modes were first discovered in the form of sound waves that was observed in St.Paul's cathedral in London. It was reported that a sound (whisper) made by a person at one point of the cathedral dome can still be heard loudly by a person standing at the other end of the dome far away. This whispering effect was explained by Lord Rayleigh in 1910. He named the sound waves as whispering gallery waves [51]. The explanation that Lord Rayleigh came up with was that the sound waves stick to the walls of the dome and propagate inside a narrow layer near the surface of the concave walls of the gallery. The intensity of sound in free space is inversely proportional to the square of the distance from the source, whereas in the case of WGM the sound intensity is inversely proportional to the distance from the source. Because of which the sound wave could propagate longer distances similar to that observed in St. Paul's cathedral. The optical analogue of the acoustic whispering gallery wave phenomenon was realized at the start of the 20^{th} century but much attention toward the research and applications was garnered only at the end of the 20^{th} century. [52].

Optical whispering gallery modes were first observed in 1961 in the form of WGM solid state lasers based on microspheres [53]. After the optical WGM demonstration, research on the WGM resonators gained momentum. In the case of optical whispering gallery modes, the mode confinement near the boundary is due to the total internal reflection, a well known optical phenomenon, that occurs continuously along the boundary of the resonator. Theoretically the whispering gallery mode behavior is well studied using coupled mode theory. WGM behavior was observed in a variety of resonator geometries including cylinders [54], spheres [55], rings [56], triangular [57], and hexagonal [58] geometries. Almost all the geometries of closed structures support the whispering gallery modes, among them circular resonators attracted much attention because of their lower losses which results in higher Q-factors. Because of the high confinement of optical fields and ultra high quality

factors these resonators were readily accepted for variety of applications in different fields.

3.2 Theory

The theory of WGM resonators is well established using the coupled mode theory [59]. The important microresonator parameters are extracted by solving the coupled mode equations.

The resonator geometry which consists of a planar microring resonator and a waveguide on each side of the resonator with electric field components in the different regions are shown in Figure 3.1.

The electric field components are

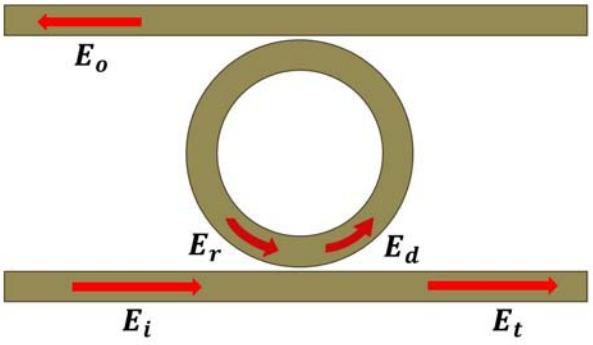

FIGURE 3.1: Microring resonator coupled to the waveguides, the different electric field components are indicated

E_i Incident electric field in the waveguide

E_d Electric field at the output of the first waveguide

E_r Electric field after one complete round trip in the resonator

E_t Through port electric field

E_o Electric field at the output of the second waveguide

The electric field components E_d, E_t can be written as a function of E_i and E_r. The coupled equations are

$$E_t = r_1 E_i + i t_1 E_r \tag{3.1}$$

$$E_d = i t_1 E_i + r_1 E_r \tag{3.2}$$

The electric field at the output of second waveguide can be written as

$$E_o = i t_2 E_d \tag{3.3}$$

where r_1,r_2 are the electric field reflection coefficients and the t_1,t_2 are the electric field transmission coefficients.

When the coupling between the waveguide and the resonator is lossless

$$|r_1|^2 + |t_1|^2 = 1 \tag{3.4}$$

$$|r_2|^2 + |t_2|^2 = 1 \tag{3.5}$$

For one round trip in the resonator, the electric field can be written as

$$E_r = r_2 e^{-\alpha \pi R} e^{i 2\pi \beta R} E_d = k e^{i 2\pi \beta R} E_d \tag{3.6}$$

where $\beta = \frac{2\pi n_{eff}}{\lambda}$ is the mode propagation constant.

k is the electric field transmission for one round trip in the resonator

$$k = e^{-\alpha \pi R} \tag{3.7}$$

where α is the intensity loss coefficient which depends on different factors which causes the loss in the resonator, R is the radius of the resonator and n_{eff} is the effective refractive index of the propagating mode.

$$\alpha = \alpha_a + \alpha_r + \alpha_s \tag{3.8}$$

where

α_a = absorption losses from the material

α_r = radiation losses from the bending of the resonator

α_s = scattering losses due to the sidewall roughness

On substituting equation 3.6 into 3.2, the drop port electric field can be written in terms of the incident electric field as follows

$$\frac{E_d}{E_i} = \frac{it_1}{1 - kr_1r_2e^{i\phi}} \tag{3.9}$$

where $\phi = 2\pi\beta R$.

The intensity of the drop port is

$$\frac{I_d}{I_i} = \frac{(1 - r_1^2)}{1 + k^2r_1^2r_2^2 - 2kr_1r_2\cos(\phi)} \tag{3.10}$$

The through port electric field can also be derived as a function of incident electric field which is

$$\frac{E_t}{E_i} = e^{i(\pi+\phi)}\frac{kr_2 - r_1e^{-i\phi}}{1 - kr_1r_2e^{i\phi}} \tag{3.11}$$

and the intensity of the through port can be written as

$$\frac{I_t}{I_i} = \frac{k^2r_2^2 + r_1^2 - 2kr_1r_2\cos(\phi)}{1 + k^2r_1^2r_2^2 - 2kr_1r_2\cos(\phi)} \tag{3.12}$$

Similarly the electric field at the output of the second waveguide can be derived from equation 3.3

$$\frac{E_o}{E_i} = \frac{(it_1)(it_2)}{1 - kr_1r_2e^{i\phi}} \tag{3.13}$$

and the corresponding intensity at the output is

$$\frac{I_o}{I_i} = \frac{t_1^2t_2^2}{1 + k^2r_1^2r_2^2 - 2kr_1r_2cos(\phi)} \tag{3.14}$$

Since the coupling between the waveguide and the resonator is phase-matched reflection coefficients r_1, r_2 and the transmission coefficient t_1, t_2 are real quantities. The resonance takes place when the electric field after one complete round trip in the resonator is in phase with the incident electric field launched in the waveguide. The resonance occurs when the phase $\phi = 2m\pi$ where m is an integer. Rewriting the phase-matching condition

$$2\pi\beta R = 2m\pi$$
$$R(\tfrac{2\pi n_{eff}}{\lambda}) = m$$

reforming the equation

$$m\lambda = 2\pi R n_{eff} \tag{3.15}$$

This is the resonance condition of the microresonator, where the resonance occurs for all wavelengths which satisfy the above condition.

At the resonance, the intensities at the through port and the output port will become

$$\frac{I_t}{I_i} = \frac{(kr_2 - r_1)^2}{(1 - kr_1r_2)^2} \tag{3.16}$$

$$\frac{I_o}{I_i} = \frac{t_1^2 t_2^2}{(1 - kr_1r_2)^2} \tag{3.17}$$

Critical coupling can be realized when $k = \frac{r_1}{r_2}$ where the intensity at the through port becomes zero and the electric field is confined only to the resonator. From equation 3.17, the maximum intensity that can be achieved at the output port when the critical coupling occurs is

$$\left(\frac{I_o}{I_i}\right)_{max} = \frac{1 - r_2^2}{1 - k^2 r_2^2} \tag{3.18}$$

3.2.1 Figures of merit

The important parameters for resonators are the Q-factor, the free spectral range and the finesse. The Q-factor is defined as 2π times the energy stored in the resonator to the energy lost in each round trip within the cavity. The free spectral range is defined as the spectral separation between two consecutive resonance frequencies/wavelengths. Finally the finesse of the resonator is defined as the ratio of the free spectral range to the full width at half maximum of the resonance which represents the spectral distinguishability.

3.2.1.1 Q-factor

The Q-factor can be written as the ratio of the resonance wavelength to the FWHM of the resonance

$$Q = \frac{\lambda_0}{\Delta\lambda_{FWHM}} \tag{3.19}$$

In order to calculate the FWHM the equation 3.14 can be rewritten as

$$\frac{I_o}{I_i} = \frac{t_1^2 t_2^2}{(1 - kr_1r_2)^2 + 4kr_1r_2\sin^2(\frac{\phi}{2})} \tag{3.20}$$

The half maximum of the output intensity happens when

$$\sin\left(\frac{\phi_{\pm(\frac{1}{2})}}{2}\right) = \pm\frac{1 - kr_1r_2}{\sqrt{4kr_1r_2}} \tag{3.21}$$

At the resonance $\phi = 2m\pi$, $\sin(\phi)$ can be approximated as ϕ

$$\phi_{\pm(\frac{1}{2})} = \pm\frac{1 - kr_1r_2}{\sqrt{kr_1r_2}} \tag{3.22}$$

$\Delta\phi$ at the FWHM is

$$\Delta\phi = \frac{1 - kr_1r2}{\sqrt{kr_1r_2}} \tag{3.23}$$

Using the equations of ϕ and β the above equation can be written in terms of the wavelength

$$\Delta\lambda_{FWHM} = \frac{(1 - kr_1r_2)\lambda_0^2}{2\pi^2 R n_{eff}\sqrt{kr_1r_2}} \tag{3.24}$$

where the dispersion of n_{eff} is neglected.

By including the coupling losses, the loaded Q factor obtained from equation 3.19 is

$$Q_L = \frac{2\pi^2 R n_{eff}\sqrt{kr_1r_2}}{\lambda_0(1 - kr_1r_2)} \tag{3.25}$$

In the case of a single waveguide coupled resonator, the Q-factor can be obtained with $r_2 = 1$ and the unloaded Q-factor can be calculated by simply setting r_1 =r_2 =1. In such cases the round trip loss is small $k \approx 1$

$$1 - k = 1 - \exp(-\alpha\pi R) \approx \alpha\pi R$$

With these approximations the unloaded Q-factor can be written as

$$Q_U = \frac{2\pi n_{eff}}{\alpha\lambda_0} \tag{3.26}$$

The usual measurement of α is in dB/cm, and considering λ in terms of μm, then the unloaded Q-factor can be written as

$$Q_U \approx \frac{2.73 \times 10^5 n_{eff}}{\alpha\lambda_0} \tag{3.27}$$

3.2.1.2 Free spectral range

The free spectral range is the separation between the resonance wavelengths.

From the resonance condition, we have

$$m = \tfrac{2\pi R n_{eff}(\lambda)}{\lambda_m} \text{ and } m + 1 = \tfrac{2\pi R n_{eff}(\lambda)}{\lambda_{m+1}}$$

The free spectral range can be written as

$$FSR = \lambda_{m+1} - \lambda_m = \frac{\lambda_0^2}{2\pi R n_{eff}} \tag{3.28}$$

3.2.1.3 Finesse

The finesse, F of a resonator is

$$F = \frac{FSR}{\Delta\lambda_{FWHM}} \tag{3.29}$$

substituting equations 3.28 and 3.24 into 3.29 the finesse can be written as

$$F = \frac{\pi\sqrt{kr_1r_2}}{1 - kr_1r_2} \tag{3.30}$$

The finesse of an unloaded resonator will be

$$F_U = \frac{\pi\sqrt{k}}{1-k} = \frac{1}{\alpha R} \tag{3.31}$$

again expressing α in dB/cm and R in μm then the finesse will be

$$F = \frac{8.68 \times 10^4}{\alpha R} \tag{3.32}$$

From the experiments if one measures the finesse, $\frac{I_t}{I_i}$ and $\frac{I_o}{I_i}$, then k,r_1 and r_2 can be extracted from the resonance spectrum.

3.3 Fabrication Techniques

The microresonators are fabricated using both commercially available and research laboratory techniques. Some of the most common lithography techniques used for the fabrication of microresonators are discussed in this section.

3.3.1 Photolithography

Photolithography is commonly used in microfabrication technology to create the microstructures in photosensitive polymers. In this lithographic technique, an ultra violet light (deep ultra violet DUV i.e. 150-300 nm to near UV -i.e. 350-500 nm) is to used to chemically modify the photopolymer. The micro structures patterned on the photo mask are directly transferred to the polymer. Thus, this fabrication technique is used for mass production of desired structures. Since it is a pattern transfer technique, the lithography is limited to 2D microstructuring of polymers and is often used in the semiconductor industry. The polymer microring resonators fabricated using UV lithography and embedded in low index material achieved high quality factors of about 10^5 [60].

3.3.2 Electron Beam Lithography

Electron beam lithography (EBL) is a well known, commercially available lithography system, used to pattern thin photoresist material sensitive to the electron beam. The electron beam can generate structures as small as sub-10 nm for isolated structures and 30 nm for an array of dense structures. The main advantage of the EBL is its high resolution. However, EBL is limited to patterning the thin resist material because of high proximity effects. The electron beam therefore is incapable of fabricating high aspect ratio structures. This fabrication technique is also used to generate masks for ion etching techniques. The microring resonators made by EBL in polymers also achieved high quality factors [61].

3.3.3 Two Photon Polymerization

Two photon polymerization (TPP) is relatively new fabrication method for micro structuring the polymers, which uses femtosecond laser pulses. In this intensity

dependent technique, ultrashort laser pulses are focused in photopolymer which absorbs two photons simultaneously and polymerizes at the focal point. One can achieve resolution below the diffraction limit because of the nonlinearity of the two photon absorption process. This fabrication method is capable of producing 3D microstructures by controlling the focal point of the laser using precise stage control and the computer aided design (CAD) file. TPP has been used to fabricate micro resonators in polymers [62].

3.3.4 Reactive Ion Etching

Reactive ion etching is a microfabrication technology used in MEMS (Micro-Electro-Mechanical Systems). In this fabrication technology, high energy ions from a plasma are used to sputter the material deposited on the wafer surface. By applying a strong radio frequency electromagnetic field in the gas environment at low pressure/vacuum, the gas molecules gets ionized and generates a plasma. The high energy ions from this plasma are used to chemically react with the wafer surface. The etch conditions in reactive ion etching depend on the process parameters like gas pressure, type of gas and RF power. The etch parameters differ for different materials of interest. Microresonators are fabricated on various materials using this technique [63].

3.3.5 Nano-imprinting lithography

Nano-imprinting lithography (NIL) is a low cost, high throughput and high resolution lithographic technology. Generally, this lithography is used to replicate the nanometric structures onto the polymer materials. The mould with the inverse nano/micro structures is generated from the master pattern, which is fabricated using the high resolution lithographic techniques such as electron beam writing/proton

beam writing and electro plating technique. This mould, which has the inverse pattern, is utilized to imprint the nano structures. By applying pressure onto a polymer film, which is preheated above its glass transition temperature, the pattern is impressed upon the polymer film. Then the system cools back to the room temperature which solidifies the nano/micro structures on the polymer film. The fast processing of imprinting makes it compatible for mass production. Nanoimprinting lithography was used to reproduce polymer microresonator with high quality factors [64].

3.4 Performance

Owing to the advancements in fabrication techniques, microresonators are being fabricated in a variety of geometries and in different materials. The precise control of the geometrical parameters of the resonators using advanced lithographic techniques results in improved performance of the microresonators. In this section, a number of microresonator geometries are introduced along with their best performances achieved so far.

The performance of microresonator varies with the resonator geometry and the material in which the resonator is made. So here the emphasis is given only for the highest Q-factors reported in each resonator geometry. Microsphere resonators of dimension 500 μm to 1000 μm were fabricated in high-purity fused silica using an oxygen-hydrogen microburner and it was reported that quality factors as high as 0.9×10^{10} were achieved at 633 nm [65]. The commonly used form of WGM resonators is microring geometry which is reported in a variety of materials. For example microring resonators fabricated in Si_3N_4 on Si substrates using TriPLEX technology [66] achieved highest Q-factor of about 2.8×10^{7} at 1310 nm wavelength [67]. The other commonly used geometry is the cylindrical cavity based microresonator. Microdisk resonators can be found in wide range of materials and the highest quality factor achieved using microdisk resonator is reported for Si_3N_4 which is

greater than $4{\times}10^6$ at 655 *nm* wavelength [68]. Microtoroidal resonators are the new form of WGM resonators first introduced by Vahala et.al [69]. The cavities are fabricated from a suspended microdisk resonator by thermal reflow technique. As a result of surface tension, the resonators form toroidal shape at their boundaries. The surface smoothness of such resonators reduces the scattering losses which results in ultrahigh quality factors. Figure 3.2 gives a summary of different WGM resonators with their highest quality factors achieved.

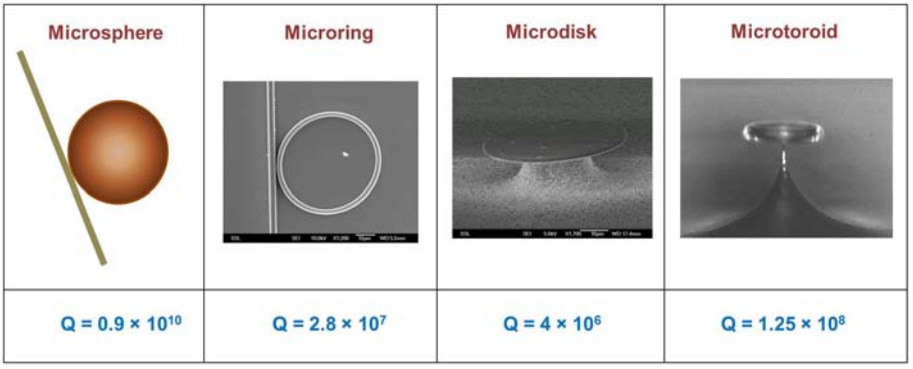

FIGURE 3.2: The whispering gallery mode microresonator geometry with its highest quality factor achieved (a) microsphere (b) microring (c) microdisk (d) microtoroid (microtoroid image taken from Ref [70])

3.5 Applications

WGM microresonators find many applications as a result from their ultrahigh quality factors and their resonance wavelength shift with slight variations in effective refractive index of the propagating mode and the physical dimensions. WGM resonators found applications in different fields like optical and bio-sensing [11], telecommunications[71], high sensitivity ultra sound detection [72], integrated optics [73], nonlinear optics [74] and cavity quantum electrodynamics [75]. Some of these applications are discussed in this section.

3.5.1 Microring modulator

The microring modulator was realized by fabricating microring resonator in an electro-optic polymer (CLD1/APC). The microresonator and the electrical contacts to the resonator were lithographically patterned by photolithography. Several other polymers were also used for the processing of the device to enable vertical coupling of light from the waveguide to the microring resonator. The top view image and the cross-sectional schematic of the final device are shown in Figure 3.3. The resonance wavelength of microring modulator modulates at the rate of 0.82 GHz/V. From the experiments, it was reported that the modulator has a bandwidth larger than 2 GHz [76].

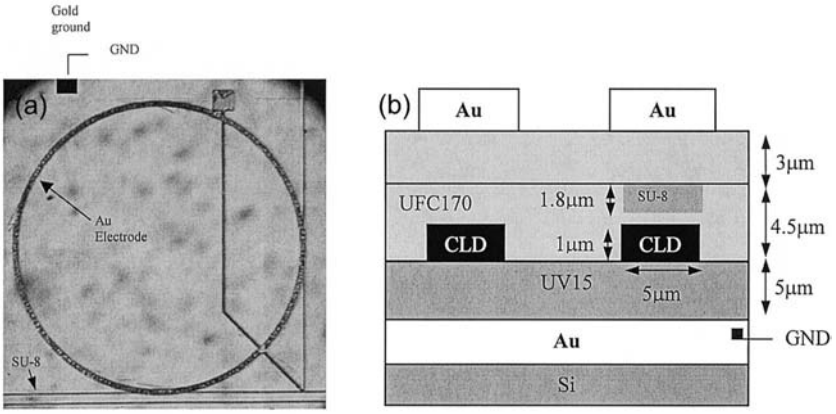

FIGURE 3.3: Microring modulator fabricated in electro optic polymer (a) top view image of the fabricated device (b) schematic showing the cross-sectional view of the final device, image from Ref [76]

3.5.2 Optical buffers

The high Q-factor of the resonator represents higher optical energy stored compared to the resonator losses. This opens up an application to make optical delay lines which helps delaying the optical signals using WGM resonators. The optical buffers are useful devices to control the speed of the optical signals. With the use of

optical delay lines, we can avoid congestion of information traffic in an optical chip [77]. The compact optical buffer was fabricated in silicon-on-insulator. The coupled resonator optical waveguides (CROW) [78] and all pass filter (APF) configurations were implemented to obtain the optical delay lines. Figure 3.4 shows the fabricated device. Using APF configuration with a footprint below 0.09 mm^2 consisting of 56 microring resonators, an optical group delay of more than 500 ps was reported.

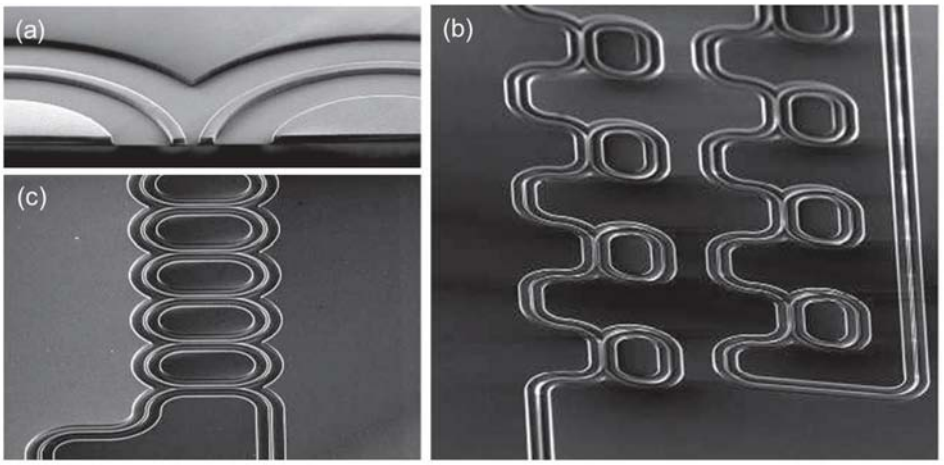

FIGURE 3.4: The optical buffers fabricated in silicon on insulator platform (a) showing the cross section of the microring and waveguide (b) optical buffer with all pass filter (APF) configuration (c) optical buffer with coupled resonator optical waveguide (CROW) configuration, image taken from Ref [77]

3.5.3 Whispering gallery mode biosensors

The spectral characteristics of the WGM resonators are sensitive to the fractional change in the effective index of the propagating mode in the resonator. This sensitivity of the WGM resonator was used as a bio-sensing tool to detect single molecules without any labels attached to the biological materials. As described in [79], the light from a tunable laser source through a tapered optical fiber is coupled to the WGM resonator (microsphere) containing the antibodies. The transmission spectrum of the WGM resonator is collected with photodetector which shows sudden drop in the transmission intensity which corresponds to the resonance wavelength

(λ_r) and the full width at half maximum of the resonance represents the linewidth $\delta\lambda_r$ which are indicated in Figure 3.5(a). When the analyte molecules binds to the antibodies, the effective index of the propagating mode changes, which results in resonance wavelength shift as can be seen in Figure 3.5 (a) and (c). When each molecule binds, the resonance shifts in the form of steps which makes single molecule detection possible. This can be seen from the inset of Figure 3.5(c).

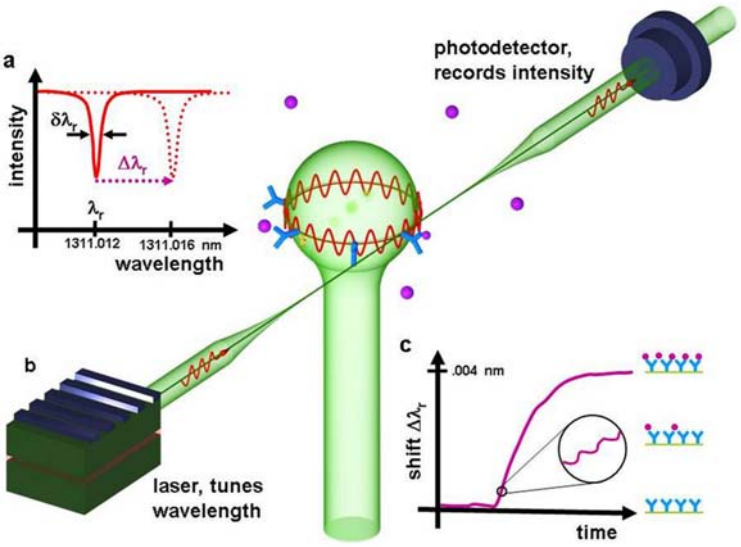

FIGURE 3.5: The biosensor model showing the working principle to detect the single molecules (a) resonance shift upon molecular binding (b) general description of obtaining transmission spectrum of a WGM microresonator (c) graph showing the wavelength shift as a function of time, inset shows the step formation upon binding each molecule, image taken from Ref [79]

Chapter 4

Planar polymer microresonators

Microresonators exhibit high quality factors as a result of the high confinement of the optical fields within the geometry of the cavity in the form of whispering gallery modes, modes that circulates along the circumference of the cavity. Because of the highly confined optical fields within the small modal volume, these cavities have found many applications in various fields from fundamental physics to applied sciences. Planar microresonators are simpler to fabricate compared to three dimensional resonators using current fabrication technologies. Furthermore, planar microresonators have the advantage of direct integration to photonic integrated circuits. Although the quality factors reported are low in polymer materials compared to semiconductors, polymers have some advantages compared to materials. Polymers are having the advantages like ease of use, compatible with the current fabrication technologies, easy engineering of materials, low cost and the availability of various refractive indices. In this chapter, a new fabrication technology, proton beam writing (PBW) is introduced which has been utilized to fabricate such polymer microresonators. The spectral responses of microresonators are discussed along with experimental demonstration of some applications.

4.1 Microdisk resonator

As discussed in Chapter 3, whispering gallery modes can be supported by many geometries however the main focus in the literature has been devoted to the circular geometries: mainly microdisk and microring resonators [80–82]. The quality factor of a WGM resonator coupled to a waveguide is classified into two components, the intrinsic quality factor $Q_{intrinsic}$ and coupling quality factor $Q_{coupling}$. The $Q_{intrinsic}$ is primarily limited by the optical losses in an isolated resonator from radiation, absorption and surface scattering [13]. Thus, the microresonator's overall quality factor can be written as

$$\frac{1}{Q_{total}} = \frac{1}{Q_{intrinsic}} + \frac{1}{Q_{coupling}} = \frac{1}{Q_{rad}} + \frac{1}{Q_{abs}} + \frac{1}{Q_{scatt}} + \frac{1}{Q_{coupling}} \tag{4.1}$$

where Q_{rad}, Q_{abs} and Q_{scatt} are the quality factors related to radiation, absorption and suface scattering respectively. In the case of microdisk and microring resonators fabricated from the same material and of same resonator dimension, the radiation and absorption losses are similar for the two resonators whereas the scattering loss is almost double for microring resonator when compared to microdisk becuase the microring has two boundaries which results in higher surface roughness. Hence it is straightforward to expect that the microdisk resonators exhibit higher quality factors compared to microring resonators [83]. In order to obtain high quality factors, microdisk resonators are better than microring resonators. Therefore, the main focus in this thesis is devoted to microdisk resonators.

4.1.1 Fabrication

The WGM microresonators are fabricated using the high resolution lithographic technique, proton beam writing in photoresist SU-8. SU-8 is an epoxy based chemically amplified, negative tone, near UV photoresist introduced by IBM in 1989 and commercially available from Micro Chem Corporation [84]. SU-8 is a highly functionalized molecule with 8-epoxy groups. The photoresist is polymerized by cationic photo-polymerization under UV illumination. Subsequent heating during post-exposure bake (PEB) activates cross-linking and also regenerates the acid catalyst which causes significant enhancement of the resist sensitivity and results in high mechanical strength and thermal stability of the structure [85]. The chemical structure of the SU-8 monomer is shown in Figure 4.1.

SU-8 has excellent optical transparency from 400 nm to near infrared wavelengths.

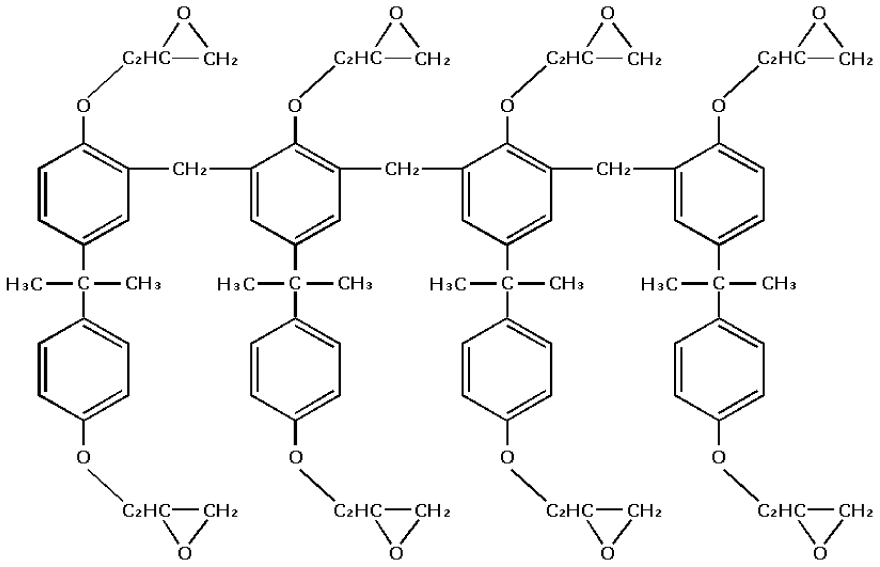

FIGURE 4.1: Chemical structure of SU-8 molecule

SU-8 has high refractive index of 1.596 at 633 nm and 1.575 at 1550 n [31]. Owing to its optical properties various optical components like optical waveguides, bragg gratings, splitters, photonic band gap structures, optical pressure sensors, on-chip light sources and optofluidic systems are realized in SU-8 photoresist [86–92]. Cross-linked SU-8 photoresist is highly resistant to a large number of acids,

bases and solvents. Due to its unique physical, chemical, mechanical, electromagnetic and bio-compatible properties, it has been reported in diverse fields of MEMS manufacturing, not only as a resist but also as the core structural material. Since cross-linked SU-8 is highly stable, high aspect ratio structures can be fabricated in SU-8. Nanostructures fabricated in SU-8 using proton beam writing showed high aspect ratio of 160 [35]. Optical waveguides fabricated in SU-8 using PBW showed low propagation losses [31]. In the present case, SU-8 photoresist has been chosen as the resonator material and the microresonators have been fabricated using PBW. The fabrication of microresonators using PBW has three major processing steps: the sample preparation with the desired thickness of the photoresist, followed by patterning the resonator structures in SU-8 using proton beam writing and finally the chemical development of the irradiated sample.

4.1.1.1 Sample preparation

The SU-8 photoresist has a refractive index of 1.575 at 1550 nm, in order to guide the optical fields in the core material SU-8 the substrate has to be lower index material. A 4 μm thick thermally grown SiO_2 on silicon is chosen as the substrate material. First the substrate is cleaned using piranha etching to remove any organic residue present on the substrate. Then commercially available SU-8 2005 photoresist is spin coated on the substrate to get a film thickness of 5 μm with the spin conditions shown in Table 4.1. After spin coating, the sample is soft baked at 95 °C for 3 min to evaporate the solvent in the photoresist. To avoid contamination of the polymer film with the dust particles present in the ambient atmosphere, the complete sample preparation process is performed in the Class 1000 clean room.

4.1.1.2 Proton beam irradiation

For the fabrication of microresonators in 5 μm thick SU-8 polymer, protons of 2 MeV energy are chosen and the proton irradiation has been carried out using the accelerator facility at Centre for Ion Beam Applications (CIBA), NUS. According to the Stopping and Range of Ions in Materials (SRIM) Monte Carlo simulations [93], 2 MeV protons can penetrate 65 μm deep into SU-8 as shown in Figure 4.2. Although it is not required to use such high energies for patterning 5 μm thick SU-8 resist, 2 MeV protons are chosen to ensure that there is no lateral spreading of the protons in the material which usually results in straight and vertical sidewall microstructures. The vertical sidewalls with smooth edges of structures helps in reducing scattering losses [94], generally resulted from surface roughness. The high energy proton beam is focused using magnetic quadrupole lenses to spot sizes less than 100 nm both in horizontal and vertical directions. This focused proton beam is then spirally scanned using magnetic scan coils. The beam scanning is controlled through the software IonScan. The proton fluence calculation is done using the backscattered spectrum obtained using annular RBS detector. The focused proton beam is used to fabricate the 50 μm diameter disk resonator using the beam scanning. A 1 cm long, 3 μm wide waveguide is also fabricated in the vicinity of the microdisk with a separation of 400 nm from the edge of the disk by line scanning of proton beam. The schematic of the proton beam writing process and the spiral scanning pattern is shown in Figure 4.3. For both the microstructures, the optimum proton fluence used is 40 nC/mm^2 (2.5×10^{13} $ions/cm^2$).

Step	Spin speed (rpm)	Time (sec)
1	500	10
2	3000	35
3	0	10

TABLE 4.1: Spin conditions to obtain 5 μm thick SU-8 film

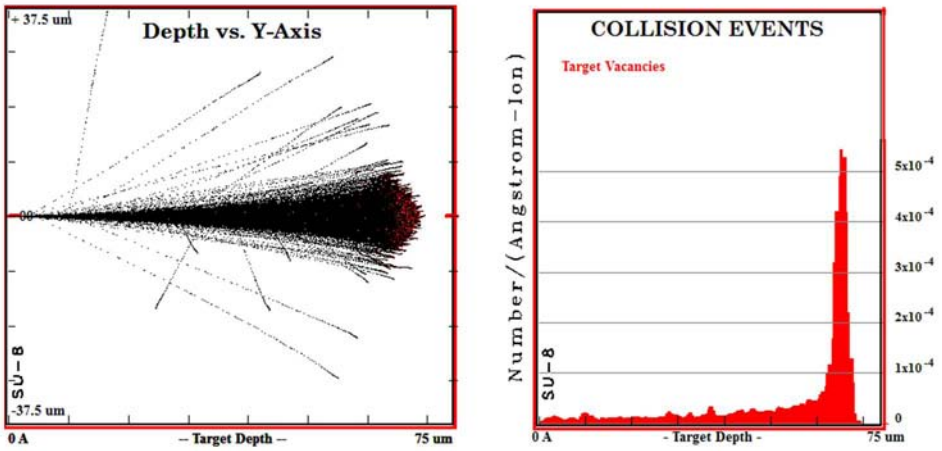

FIGURE 4.2: 2 MeV proton track in the SU-8 photoresist calculated from SRIM simulations

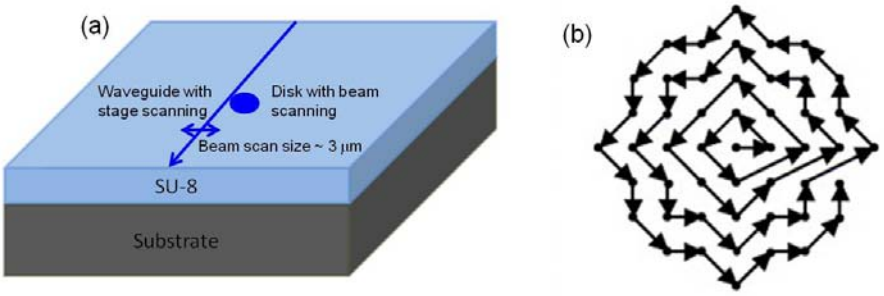

FIGURE 4.3: (a) The schematic representation of the fabrication of microresonator with PBW, (b) spiral scanning pattern of the resonator

4.1.1.3 Chemical development

After the proton irradiation, the sample is chemically developed using the commercially available SU-8 developer (1-Methoxy-2-propanol acetate) to remove the unexposed photoresist which leaves the proton irradiated region; that is the micro disk resonator along with the integrated waveguide. In terms of the chemical development procedure, common fabrication techniques require post-exposure bake to generate the photo acids which are essential to cross-link the polymer. Whereas in the case of the PBW post-exposure bake is not required since the protons are able to generate the photo acids during the irradiation itself which reduces a processing

step compared to other fabrication techniques. The sample is placed in the SU-8 developer for longer time in order to remove the unirradiated polymer in the small gap between the structures. The resulting microdisk and microring resonators along with integrated waveguide can be seen in Figure 4.4.

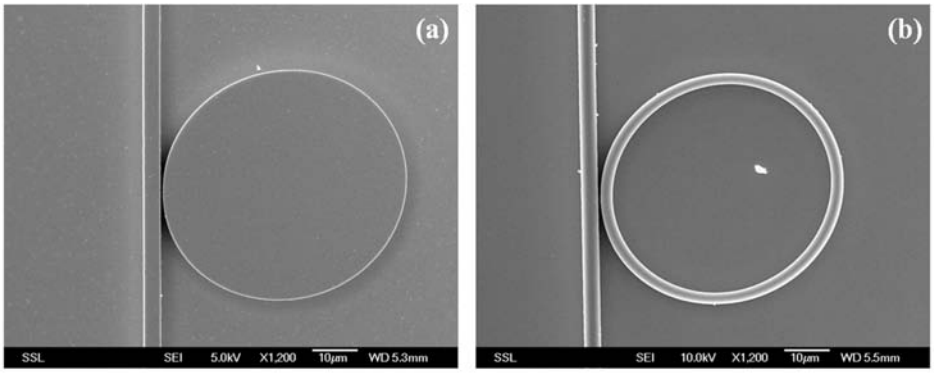

FIGURE 4.4: Micro resionators fabricated in SU-8 using PBW (a) microdisk resonator of 50 μm diameter with 3 μm waveguide fabricated at a separation of 400 nm from the disk (b) microriong resonator of the same parameters as microdisk with a microring width of 2 μm

4.1.2 Optical Characterization

The spectral response of an optical resonator is expected to show a sudden change in transmitted or reflected power at the resonance wavelengths. The transmission spectrum shows a sudden decrease in transmitted power for resonance wavelengths and a maximum transmission for all non-resonant wavelengths, whereas the reflection spectrum shows the opposite, an increased power at the resonance wavelengths and a minimum power at all other non-resonant wavelengths. The spectrum can be obtained in two ways. First and the simplest scenario is to use the spectrometer to collect the transmitted (reflected) power from the resonator by broadband laser illumination [95]. Second and the more precise method is to measure the transmitted power by continuously tuning the incident laser wavelengths which results in transmission spectrum [96]. In the present work, the second approach is used

since the whispering gallery mode resonators generally exhibit high quality factors. For polymers, it is in the range of 10^3 to 10^5. Spectrometer with such high spectral resolution is not available in the near infrared wavelength regime. In order to measure the transmission spectrum, tunable laser light is coupled into the optical waveguide fabricated in SU-8 and the transmitted output power from the waveguide is measured using a power meter. Since the optical waveguide is patterned close to the microdisk, the evanescent optical fields from the waveguide can couple to the microdisk. In the transmission spectrum, a sudden drop in the transmission power is expected for the microdisk resonance wavelengths. The optical properties of the microdisk resonator were experimentally measured with the aid of the end-fire coupling setup.

The optical characterization set up is shown in Fig 4.5. For the present case, the microdisk resonator is characterized within the telecommunication wavelength regime. The output of tunable laser source (Agilent TLS-81980A) is fiber-coupled to a 40x microscope objective lens placed on a three-axis nanopositioner translational stage (ThorLabs NanoMax) to collimate the laser beam. In the path of the laser beam, a polarized cube beam splitter and the half waveplate is placed to select the incident polarization of the light coupled into the optical waveguide. The polarized light is fed into the 60x microscope objective lens which is then focused onto one end-facet of the optical waveguide. An objective lens (20x) is used to collect the light from the other end-facet of the waveguide. The collected light is collimated and directed to the power meter (Agilent 81619A) to measure the transmission power. The two objective lens are placed on three-axis nanopositioner stages to precisely align laser beam and to control the angle of incidence, which is essential to achieve the total internal reflection condition. To make the waveguide alignment convenient, two important optical components are included in the set-up. A high sensitivity InGaAs camera (Xeva 756) is mounted on top to observe the scattered light from the sample to better know the position of the focused spot of the laser. Another IR camera (Vidicon Electrophysics MicronViewer) is used to observe the output mode

of the waveguide which is placed perpendicular to the path of laser beam. With the inclusion of 45° flip mirror in the path of the laser, we can direct the laser beam to reach either the camera or the power meter. Simultaneously, this set up can also be used for tapered lensed fiber coupling by replacing the input objective lens with a tapered lensed fiber. For the selection of input state of polarization, a fiber polarization controller (ThorLabs FB51) is included between the tunable diode laser and the tapered lensed fiber. The tunable diode laser and the power meter are controlled using the LabVIEW program for acquiring the transmission spectrum.

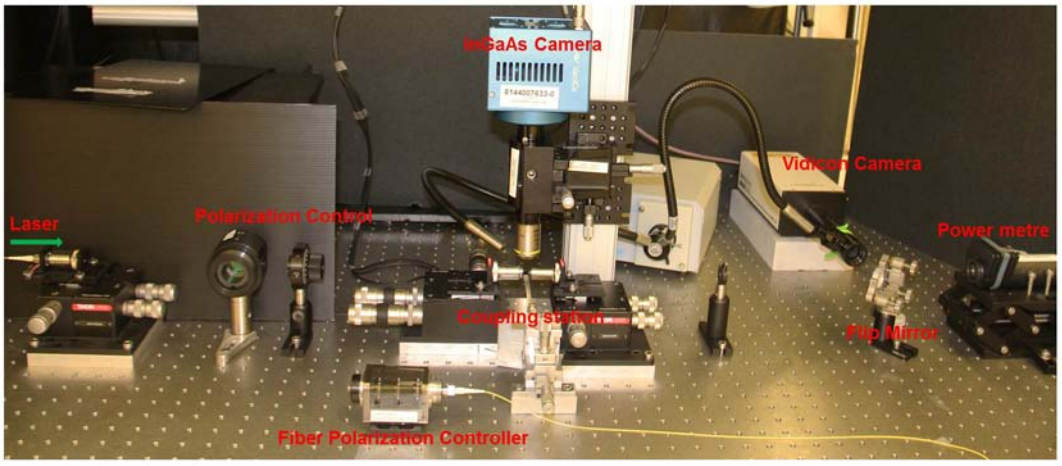

FIGURE 4.5: End fire coupling set-up showing the important components in the set-up

With the current optical set-up, it is easy to couple the laser beam into the waveguide by observing the scattered light from the top-view InGaAs camera and by monitoring the output mode through the Vidicon IR camera. The absence of these two components poses greater difficulty to couple light into optical components like waveguides.

4.1.3 Results and Discussion

The fabricated 50 μm diameter microdisk resonator is optically characterized using the free-space end-fire coupling set-up. The transmission spectrum of the microdisk resonator is obtained by collecting the transmitted power from the waveguide which is evanescently coupled to the microdisk. The experimental transmission spectrum of the micro disk resonator for the incident TE polarized light is shown in Figure 4.6 within the wavelength band of 12 nm from 1544 nm to 1556 nm. As expected the transmission spectrum showed a sudden drop in power at the resonance wavelengths. The resonance wavelengths are calculated theoretically using equation 3.15. The calculated resonance wavelengths are well matched with the experimental resonance wavelengths for the fundamental mode with azimuthal mode numbers 165 and 166. The experimental transmission spectrum also showed a broad resonance in between the sharp fundamental resonances which might correspond to the higher order cavity mode that is excited from one of the higher order modes of the fabricated multimode waveguide.

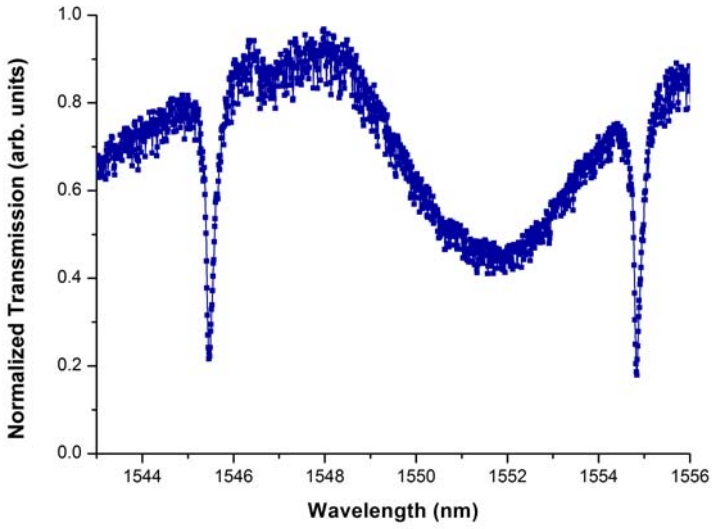

FIGURE 4.6: The experimental transmission spectrum of 50 μm diameter microdisk resonator showing the two fundamental resonances

Resonance wavelength (nm)	Q-factor
1545.49	8085
1554.85	10800

TABLE 4.2: Resonance wavelengths and the corresponding Q-factor

4.1.3.1 Quality factor

From the experimental transmission spectrum, each resonance is fit with a Lorentzian function to find the full width at half maximum (FWHM) of the resonance and the resonance wavelength. From the resonance wavelength and the FWHM, the Q-factor of the microdisk is calculated using the equation 3.19. The Q-factor calculated at the different resonant wavelengths is tabulated in Table 4.3. The highest quality factor obtained is $1.1\times\ 10^4$ at the resonance wavelength of 1554.85 nm with a FWHM of 0.14 nm. The obtained quality factor is high for polymers. Usually to achieve high quality factors for polymer microresonators, thermal reflow technique is used to smoothen the resonator sidewall, whereas in the present case no additional step is included to smoothen the polymer resonator sidewall.

4.1.3.2 Free spectral range

The free spectral range of the fabricated microdisk resonator is 9.31 nm calculated from theoretical equation 3.28. The experimental transmission spectrum also showed the separation between the resonance wavelengths to be 9.36 nm which is in close agreement with the theoretical value.

4.1.3.3 Cavity Loss calculation

The experimentally obtained transmission spectrum is fit with the theoretical transmission equation 3.12 to obtain the amplitude attenuation factor k and the electric field reflection coefficient r. The theoretical transmission spectrum is obtained from

the sum of fundamental and the higher order resonances which is shown in Figure 4.7. The extracted parameters from the theoretical fit are

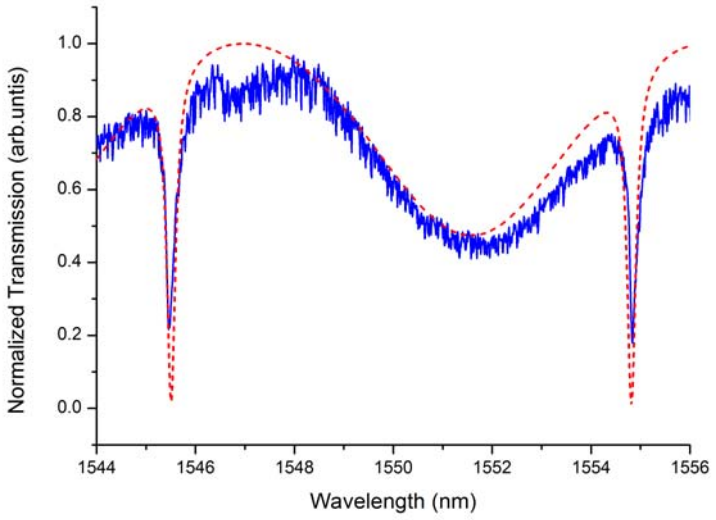

FIGURE 4.7: The theoretical fit for the transmission spectrum for the two modes excited in the resonator

$$k = 0.95$$

$$r = 0.98$$

The cavity loss can be obtained from the amplitude attenuation factor. From the equation 3.7,

$$\alpha = 24.6\ dB/cm$$

Thus,the SU-8 microdisk resonator fabricated using proton beam writing has a loss of 24.6 dB/cm.

From the above extracted values, the figures of merit can be calculated using the theoretical equations derived in Chapter 3. All the parameters calculated through theoretical equations and from the experimental transmission spectrum are tabulated in Table 4.3

Resonance wavelength (nm)	Q-factor		FSR		Finesse	
	Exp	Theory	Exp	Theory	Exp	Theory
1545.49	8085	7294				
1554.85	10800	7294	9.36 nm	9.31 nm	66	61

TABLE 4.3: Cavity parameters calculated from the experimental transmission spectrum

4.1.3.4 Two dimensional FDTD Simulations

Two dimensional FDTD simulations [97] are carried out with the experimental parameters in order to confirm the results obtained from the experiments. The dimension of the microdisk resonator and the integrated waveguide is extracted from the SEM micrograph. The optical mode information is obtained from the mode simulator using Rsoft FemSIM software [98], which uses the finite element method to calculate the optical modes in the waveguide. The TE polarized light pulse is launched into the waveguide. The evanescent optical field from the propagating mode in the waveguide is coupled to the microdisk which then circulates in the microdisk. The simulation is carried out for time scales much larger than the time required to complete one round trip in the resonator. The spectral response of the resonator is obtained from the transmitted electric field components. The transmission spectrum of the microdisk resonator obtained from the simulation and the experiments is plotted together and can be seen in Figure 4.8.

The simulation result showed that the fundamental resonances are well matched with the one that obtained from the experiments. It is also clear from the simulations that the fabricated resonator supports more than one cavity mode.

As mentioned earlier, with the present characterization set-up we are able to capture the scattered light image using top-view camera. Figure 4.9 shows the experimentally obtained scattered light image at resonance along with the simulated field distribution within the resonator obtained for the same resonance wavelength (1554.85 nm).

All the required parameters which determine the quality of the resonator are

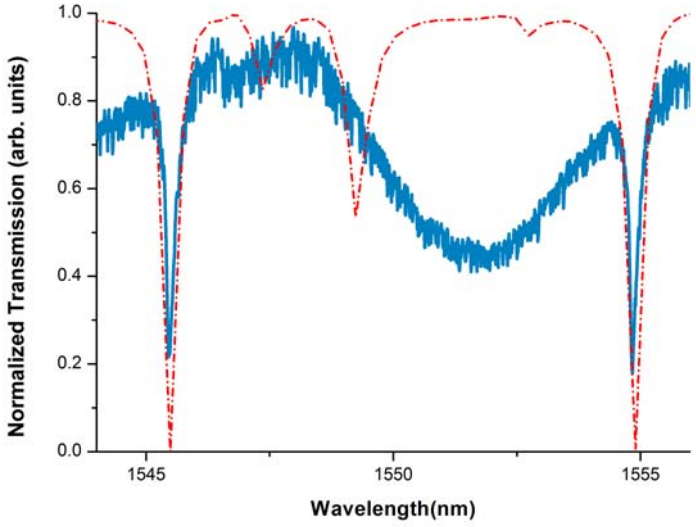

FIGURE 4.8: The transmission spectrum for the microdisk resonator obtained through experiment (solid blue line) and the FDTD simulation (dash-dot red line)

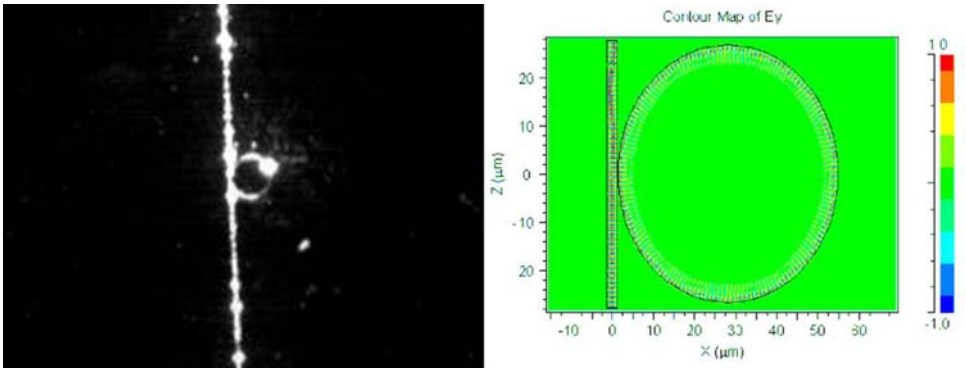

FIGURE 4.9: The optical mode in the resonator obtained from (a) experiment and (b) simulation

extracted experimentally and as well as theoretically. The obtained results are verified using the FDTD simulations and the results are in close agreement with the experiments.

4.1.4 Application of microdisk resonator as wavelength filter

The optical wavelength filters are useful elements in photonic integrated circuits. Different wavelengths can be used for different applications to increase the processing speeds in telecommunication networks. Whispering gallery mode resonators are well suited for this application because of the narrow resonance linewidth which helps in reducing the cross talk between the different wavelengths [99]. For the whispering gallery mode microdisk resonators, the resonance wavelengths and the free spectral range can be predefined according to the application. To obtain single wavelength transmission in C-band, the cavity dimensions can be reduced in order to increase the free spectral range. To demonstrate the wavelength filtering, the same microdisk of 50 μm diameter is employed to filter 4 spectral lines in the C-band. The experimental transmission spectrum shown in Figure 4.10 clearly shows the wavelength filtering and the four spectral lines can be easily observed since the Q-factor is high, the spectral lines can be resolved within 0.3 nm range. In order to observe a single resonance line in the C-band, the resonator diameter should be reduced to less than 14 μm.

4.2 Whispering gallery mode microlaser

Whispering gallery mode micro resonators are ideal candidates for laser devices because of the high quality factors and narrow spectral line characteristics. As a result of these characteristics, microlasers based on WGM resonators generally yield lasing with low thresholds and low laser linewidths [100]. Compared to other types of microlasers such as distributed feedback lasers [101] and lasers based on photonic crystal cavities [102], WGM lasers resulted in superior performance. Although WGM based micro lasers are superior, the emission from such cavities is

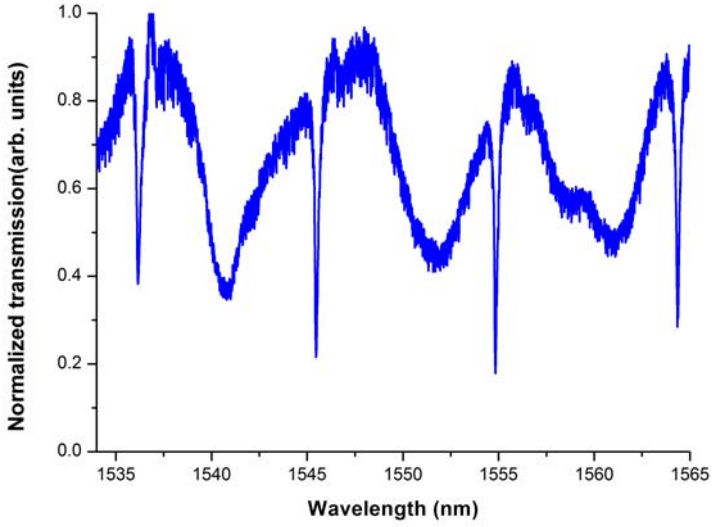

FIGURE 4.10: The experimental spectrum showing the wavelength filtering effect by filtering 4 different resonance lines of the 50 μm disk resonator

omni-directional rather than uni-directional because of the inherent circular symmetry. In recent years, much attention is devoted to make such cavities directional by deforming the circular design which resulted in various geometrical designs of micro lasers [103–108]. Polymer materials offer flexibility in fabrication of active cavities with dissolution of laser dye in the polymer. In this section, dye-doped polymer microlasers based on whispering gallery mode resonators are experimentally demonstrated different geometrical designs of the cavities to make WGM based microlasers directional.

4.2.1 Review of planar microlasers

High Q-factors obtained in WGM resonators is the key feature responsible for the superior microlaser performance compared to the other cavities like fabry perot cavity, distributed feedback lasers, and photonic crystal cavities [109–114]. Distributed feedback lasers fabricated in dye-doped SU-8 polymer matrix generally result in laser thresholds of the order of hundreds of $\mu J/mm^2$ [115]. Photonic crystal cavity

based microlasers require hundreds of μJ energy per pulse [116] in order to show lasing behavior. The WGM based dye-doped polymer microlasers showed a range of lasing thresholds vary from few hundred μJ per pulse to few nJ per pulse [117–120]. In this section, planar whispering gallery mode microlaser cavities of different cavity designs with pump fluence in the range of few $\mu J/mm^2$ are discussed.

The basic components of the laser are gain medium, pumping source and resonant cavity. The active gain medium serves as the photon source in the laser. The pumping source excites the atoms to the higher energy levels which then relax to their more stable lower energy levels by releasing photons. Finally the resonant cavity directs these emitted photons back into the gain medium in which the amplification of the stimulated emitted photons occurs. Once the system achieves the population inversion condition, higher number of atoms in the excited states compared to its ground state, lasing takes place. In the present case, the whispering gallery mode resonator serves as resonant cavity and the pumping mechanism is optical excitation using Nd:YAG laser and the gain medium is an organic dye-doped polymer.

4.2.2 Fabrication

4.2.2.1 Gain medium preparation and characterization

The dye-doped polymer is prepared by dissolving the laser dye into the polymer. The polymer of interest is SU-8 photoresist which is also used for the fabrication of the whispering gallery mode micro disk resonator. In the present work, two Rhodamine laser dyes are used namely, Rhodamine B (RhB) and Rhodamine 6G (Rh6G).

RhB and Rh6G are out of the Rhodamine family which are fluorene based dyes. Rhodamine dyes are dissolved in solvents like water, methanol and ethanol. These laser dyes dissolved in solvent are used as laser gain medium in dye lasers. Rhodamine dyes have the higher quantum yields of 0.75, 0.78 in solid matrix PMMA

for Rhodamine B and Rhodamine 6G respectively [121].

The commercially available RhB and Rh6G perchlorate laser grade dyes are obtained from Sigma Aldrich [122] and the chemical structures of both the dyes are shown in Figure 4.11.

For the preparation of the dye doped polymer films, first commercially available

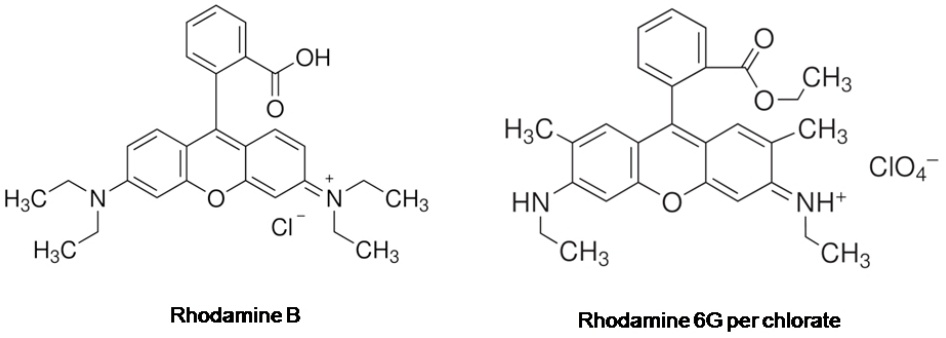

FIGURE 4.11: Chemical structure of Rhodamine B and Rhodamine 6G perchlorate

RhB (Rh6G) laser dye is dissolved in negative resist thinner GBL (Gamma ButyroLactone). When the dye is completely dissolved into the GBL, the resulting solution is then added to the SU-8 2005 resist and ultra sonicated for few hours to completely dissolve the dye solution in the SU-8 polymer matrix. Different weight percentages varying from 0.25 % to 2% of the RhB (Rh6G) dye in SU-8 was prepared to study the spectral characteristics of the dye-doped polymer films. The dye dissolution process is highlighted in Figure 4.12.

The cross-linked dye-doped polymer films are prepared to investigate the optical characteristics of the different dye concentrations in the polymer. The resulting RhB (Rh6G) doped SU-8 polymer is spin coated with the same spin conditions given in Table 4.1 in order to get 5 μm thick films on microscope cover slip. The samples are then soft baked at 95 °C for 3 *min* to evaporate the solvent. The films are then exposed under UV light for 15 *min* in order to cross link the polymer films, after which the sample is post baked at 95 °C for 2 *min*. The schematic of preparation of the dye-doped polymer films is shown in Figure 4.13. Different concentrations

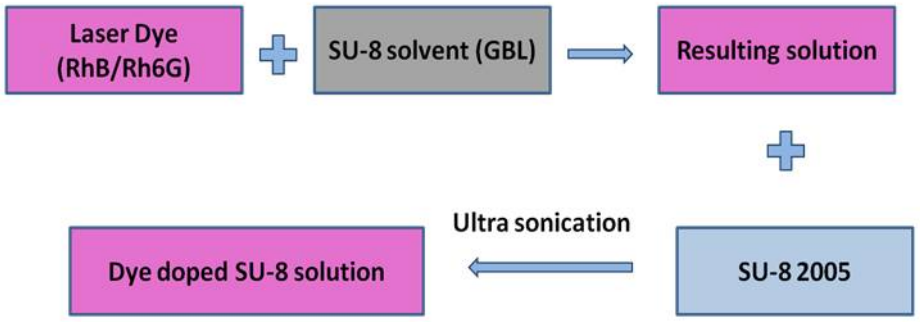

FIGURE 4.12: Schematic representation of dye dissolution process

of dye-doped polymer films are prepared with the same spin condition in order to ensure the thickness of the polymer films is consistent.

The absorption spectra of the dye-doped polymer films with different dye con-

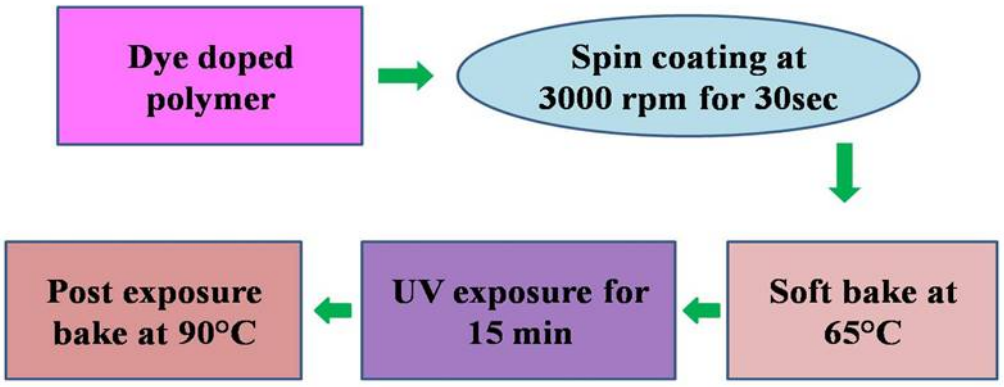

FIGURE 4.13: Dye doped polymer film preparation steps

centrations of RhB (Rh6G) are obtained using the UV-Vis-NIR spectrophotometer (Shimazdu UV3600 Spectrophotometer). The photoluminescence (PL) spectra is collected using the home-built photoluminescence set-up under 405 *nm* laser excitation. The absorption and the emission spectra of the RhB doped SU-8 films of different concentrations are shown in Figure 4.14. The absorption spectra of the RhB doped SU-8 films are in the visible range with a bandwidth of 35 *nm* and

the peak wavelength at 565 *nm*. The absorption increases as the dye concentration increases. The same films under the photoluminescence set-up show fluorescence in the visible range with bandwidth of 35 *nm* with peak emission at 600 *nm*. It can be seen from the spectra that 1% RhB doped SU-8 film shows the highest photoluminescence signal among other dye concentrations. This concentration of RhB in SU-8 could result in lasing with low pump fluence. In the spectral range of 575-590 *nm*, there is obvious overlap between the absorption band and the PL band, which could be observed in Figure 4.14. It is expected that the lasing action will not occur in this spectral range due to the reabsorption of the emitted photons within the gain medium. In contrast, above 590 *nm* wavelength, lasing is expected as the absorption is negligible compared to the fluorescence emission intensity.

The absorption and the emission spectra of the Rh6G doped SU-8 films of different

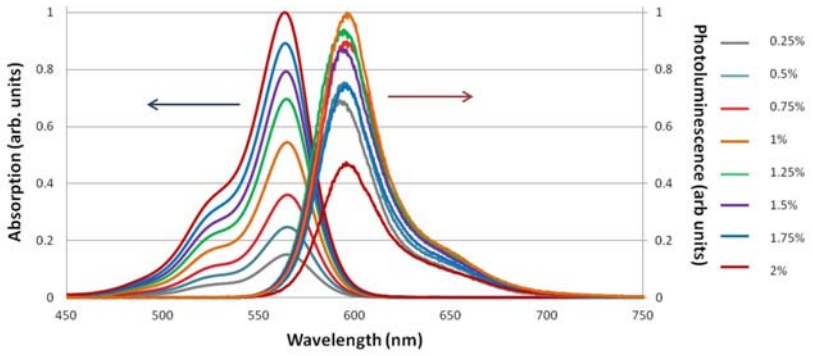

FIGURE 4.14: Absorption and emission spectra obtained from different concentrations of the Rhodamine B content in SU-8

dye concentrations can be seen in Figure 4.15. The absorption of the Rh6G doped SU-8 polymer film is centred at wavelength of 520 *nm* and the corresponding emission from the same film is observed with a spectral width of 40 *nm* centred at 590 nm and one can observe from the Figure 4.15 that there is also an overlap between the absorption and the emission bands in the range from 550 - 570 *nm* in which no lasing can be expected because of the reabsorption of the emitted photons within the gain medium.

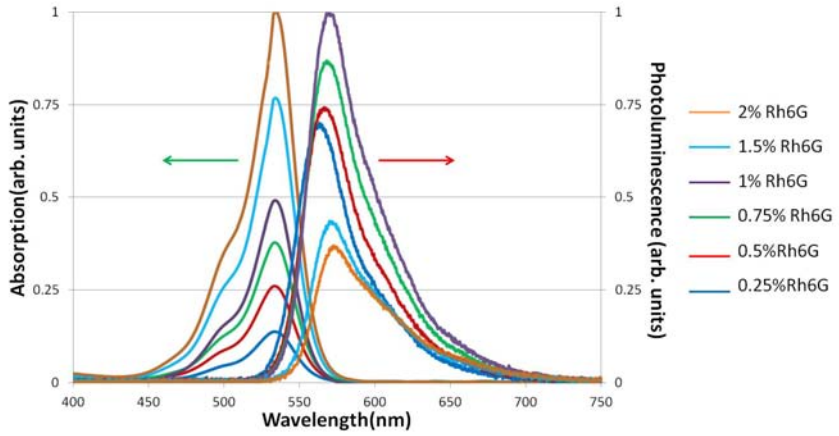

FIGURE 4.15: Absorption and emission spectra obtained from different concentrations of the Rhodamine 6G content in SU-8

4.2.2.2 Fabrication procedure

All the cavity designs presented in this section are generated using MATLAB (codes documented in Appendix C) except the disk resonator which is generated using IonUtils.

Although different geometries of the laser cavities are designed, the fabrication procedure implemented is the same for all cavity designs. First, the dye-doped polymer is spin coated on the desired substrate (in the present case 4 μm thick SiO_2 on silicon as the substrate) to form a 5 μm thick RhB/Rh6G doped SU-8 polymer film. In order to evaporate the solvent in the polymer, the dye-doped polymer sample is soft baked at 95 °C for 3 min. Then the sample is cleaved to the desired dimensions to load the sample in the target chamber of 10 ° beamline. 2 MeV protons are used to fabricate the different cavities in dye-doped polymer film since the electronic collisions are enough to cross link the polymer film. The proton beam is focused down to the spot size of 100 nm or less in both horizontal and vertical directions using the magnetic quadrupole lenses. The focused beam is then magnetically scanned along the desired design using beam scanning to cross-link the dye-doped polymer. All the cavities are fabricated with a proton fluence of 6.25×10^{13} $protons/cm^2$. The sample is then chemically developed to form the

irradiated pattern on the sample. As mentioned earlier, the proton beam writing does not require post-exposure bake step in the fabrication procedure in order to generate the photo acids. The schematic of the fabrication procedure is illustrated in Figure 4.16

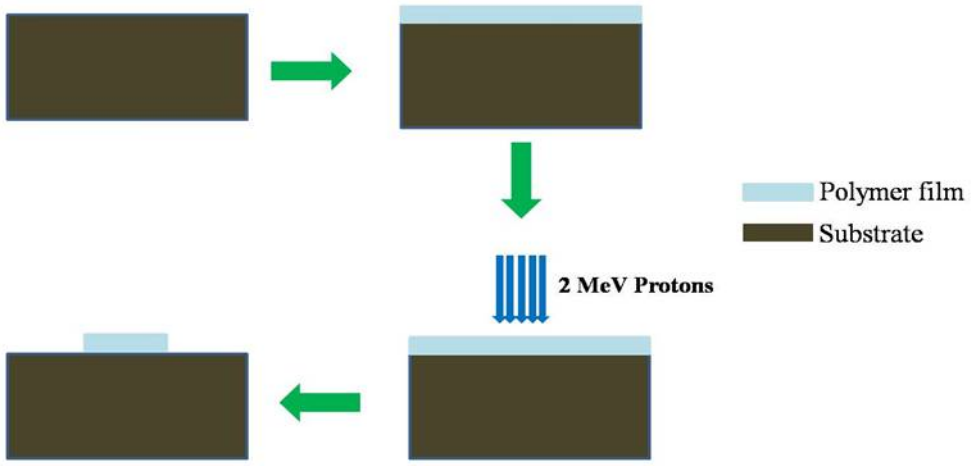

FIGURE 4.16: Schematic showing the fabrication of dye doped polymer lasers using PBW

4.2.3 Optical characterization

The fabricated dye-doped polymer whispering gallery mode micro lasers are characterized by photo pumping of the cavities with the frequency doubled Nd:YAG laser (Spectra Physics DCR3) with 7 nanosecond pulse width and of 10 Hz repetition rate. The dye molecules absorbs the 532 nm photons from the nanosecond laser and emit photons in the emission band of the particular dye of interest. Only certain modes from the emission band exists within the cavity depending on the resonance condition of the whispering gallery mode cavity. Those modes that overcome the losses incurred in the cavity results in lasing spectral lines.

4.2.3.1 Free space photo pumping set-up

The free space photo pumping set-up shown in Figure 4.17, the pump laser beam is directed normal to the sample using a 45° mirror. The sample is placed on a two axis translational stage (Newport ULRAlign) and a fixed diameter aperture (600 μm) is positioned to avoid the unwanted pump laser energy on to the sample. A 10x objective lens is placed on a three-axis translation stage in order to collect the emitted light from the microlaser in the tangential plane of the laser cavity. The collimated output light from the objective lens is then directed to the fiber coupled spectrometer (Ocean Optics HR4000) to collect the spectrum for the microlaser emission. In this optical set-up the fiber coupled spectrometer can be interchanged with the CCD camera to view the emission pattern from the microlaser.

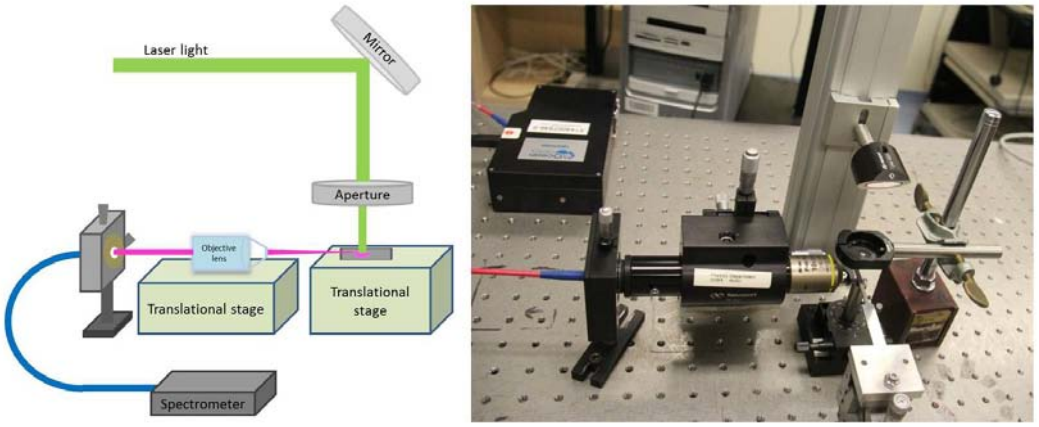

FIGURE 4.17: Free space photo pumping set-up (a) schematic of the set-up (b) characterization region of the set-up

The pump fluence is calculated from the laser energy (E) and beam waist (ω_0) of the pump laser with the following formula.

$$F = \frac{2E}{\pi\omega_0^2} \tag{4.2}$$

4.2.3.2 Effect of dye-doped polymer upon proton beam irradiation

To check the response of the dye-doped polymer when under proton irradiation, square micro structures of 50 μm side length are fabricated with different proton fluence. After the proton irradiation the sample is undergone chemical development process which results in square microstructures on silicon substrate. The sample is then used to perform the photoluminescence experiments to check whether the proton irradiation induce any fluorescence quenching. The emission from the square patterns of different proton fluence showed reduction in the fluorescence. It is clear from the experiments that up to the proton fluence of 200 nC/mm^2, there is no significant fluorescence quenching observed. The microstructures are characterized using the scanning electron microscopy to optimize the proton fluence in order to achieve the straight sidewalls and is found that 80 nC/mm^2 proton fluence is the optimum fluence required for the fabrication of micro structures in dye-doped SU-8 polymer.

4.2.4 Planar microdisk lasers

The planar microdisk resonators are fabricated in 1% RhB and 1% Rh6G doped SU-8 with optimum proton fluence. These dye-doped microdisk resonators acts as microlasers upon optical excitation.

4.2.4.1 Rhodamine B doped SU-8 micro disk laser

The 1 % Rhodamine B doped SU-8 film of 5 μm thickness is prepared on SiO_2/Si substrate. Focused proton beam is employed to pattern the 50 μm diameter circular structures in spin coated dye-doped polymer film and the subsequent chemical

development of the patterned resist results in microdisk laser. The optimum proton fluence 80 nC/mm^2 is used to fabricate the microlaser. The optical and SEM micrographs of the fabricated device can be observed in Figure 4.21.

The sample is then used for optical characterization to obtain the micro laser

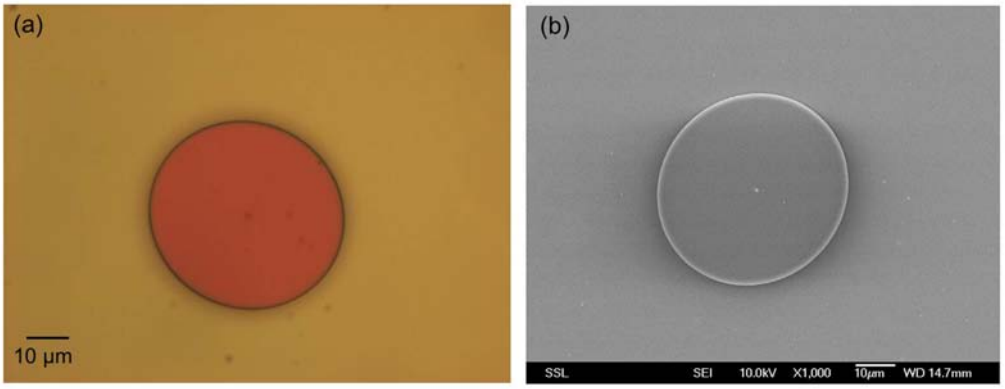

FIGURE 4.18: The optical and SEM micrographs of the fabricated planar microdisk laser in RhB doped SU-8

characteristics. To characterize the polymer micro disk laser the sample is placed on the free-space photo pumping set-up. The cavity is optically excited with the pump laser from the top and the emission from the microlaser is collected in-plane to the microdisk through the objective lens and fiber coupled spectrometer. The emission spectrum centered at 640 nm is observed and emission spectra is collected as a function of the incident energy of the pump laser. The emission intensity is plotted as a function of pump fluence and the graph represents a sudden change in slope which corresponds to the threshold fluence of the microlaser. After the threshold pump fluence of 1 $\mu J/mm^2$, the cavity acts as a laser. The emission spectrum obtained above threshold fluence and the plot of emission intensity as a function of pump fluence is shown in Figure 4.19.

In the above spectrum the individual resonance lines are indistinguishable because of the limitation of spectrometer resolution. As can be observed from the Figure 4.19, the sharp peaks at the top of the spectrum correspond to the whispering

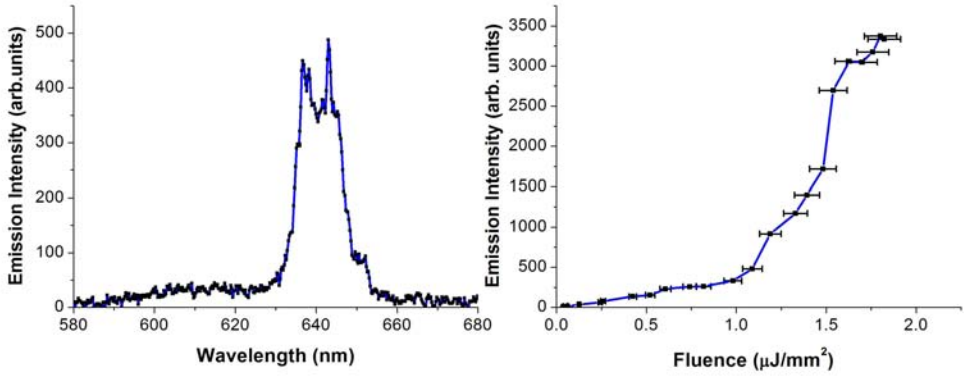

FIGURE 4.19: The figure shows the emission spectrum of the RhB doped SU-8 micro disk laser above the threshold pump fluence along with graph of emission intensity as a function of pump fluence.

gallery modes. In order to observe the individual whispering gallery modes, smaller diameter microdisk was fabricated and characterized. The spectrum in Figure 4.20 clearly shows the well resolved spectral lines which are the WGM modes. The free spectral range calculated from the separation between the spectral lines is 5.35 nm and is well matched with the theoretically calculated FSR for the particular resonance wavelengths. Although the spectral lines are well separated, the linewidth is not accurate and is limited by the spectral resolution of the spectrometer. Therefore, it is not feasible to estimate the Q-factor of the microlaser from the experiment.

4.2.4.2 Rhodamine 6G doped SU-8 micro disk laser

In a similar procedure, the microdisk resonator is fabricated in 1% Rh6G doped SU-8. A 5 μm thick, 50 μm diameter Rh6G doped SU-8 microdisk resonator's optical and the SEM micrographs can be seen in Figure 4.21.

By optically characterizing the fabricated device, laser emission centred at 605 nm was observed. The threshold fluence was estimated to be 1.5 $\mu J/mm^2$ from the graph plotted with emission intensity as a function of input pump fluence. The

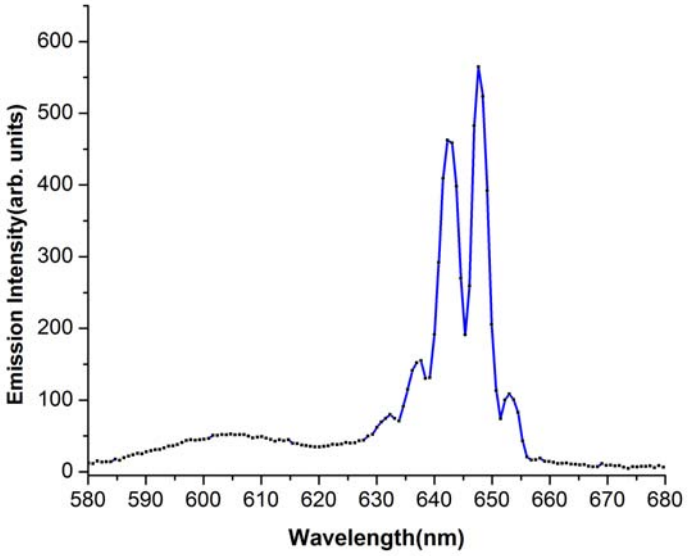

FIGURE 4.20: The emission spectrum of the RhB doped SU-8 micro disk laser of 10 μm diameter above the threshold pump fluence

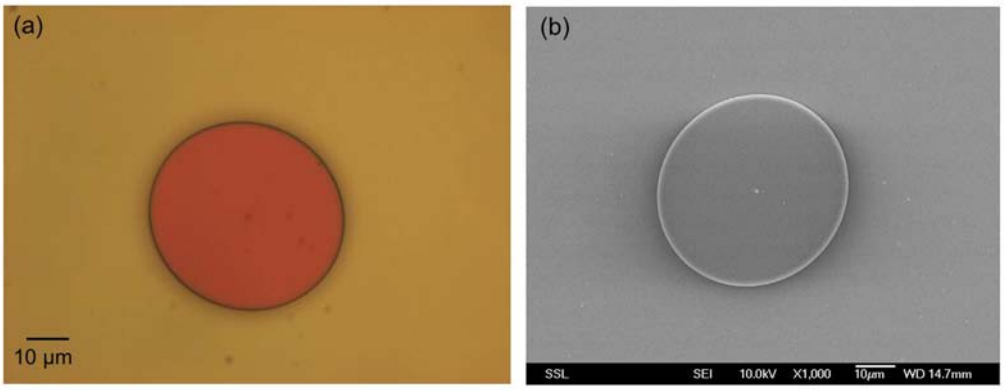

FIGURE 4.21: The optical and SEM micrographs of the fabricated planar microdisk laser in RhB doped SU-8

threshold curve and the emission spectra can be observed in Figure 4.22.

A comparison is made between the two different dye-doped SU-8 microlasers fabricated. The microlasers fabricated in RhB doped SU-8 showed less pump thresholds compared to Rh6G doped SU-8. Therefore, the further work in this thesis is focused only on RhB doped SU-8 microlasers.

The optical characterization of the planar microdisk laser showed non-directional

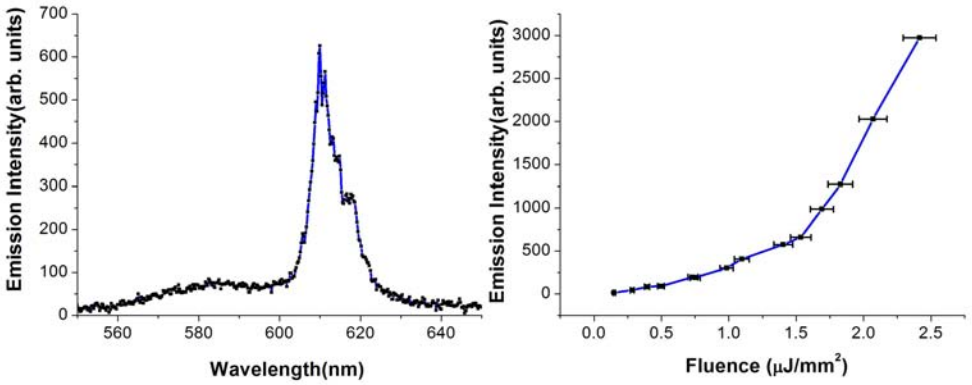

FIGURE 4.22: The figure shows the emission spectrum and the threshold curve of the Rh6G doped SU-8 micro disk laser

emission from the disk laser. A similar spectral response is observed from all directions in the tangential plane of the microdisk. This non-directional laser emission is observed because of the inherent radial symmetry of these circular microresonators, which is undesirable for practical applications.

4.2.5 Directional WGM microlasers

As mentioned earlier, the emission from the microdisk laser is direction independent which made it less efficient. A lot of efforts are devoted to create the WGM laser directional and researchers have come up with variety of cavity designs to obtain the directional behavior in such microlasers. It is found that the directionality is achieved by deforming the symmetrical microdisk laser [103, 106, 123, 124]. In this section different directional cavity designs are discussed and are experimentally demonstrated.

A microdisk resonator could be deformed by spiralling the cavity. With this kind of cavity the propagating mode will be directed to the notch region which could enable the directional emission from the notch region. Three different spiral disk

cavities have been fabricated which are spiral disk laser with notch, spiral disk laser with extended waveguide and elliptical spiral cavity with extended waveguide.

4.2.5.1 Spiral disk resonator with a notch

The spiral microdisk resonator is designed using the following spiral equation

$$r = r_0(1 + \frac{\epsilon}{2\pi}\phi) \tag{4.3}$$

where r_0 is the inner radius of the spiral and ϵ is the aspect ratio and ϕ is the radial angle, so the ϵ defines the notch width. In the present case, the spiral is designed with r_0 of 13.6 μm and ϵ of 0.1 which results in the notch width of 1.4 μm. The optical micrograph of the fabricated spiral laser shown in Figure 4.23.

The photo pumping of the resulted structure is carried out using the free-space

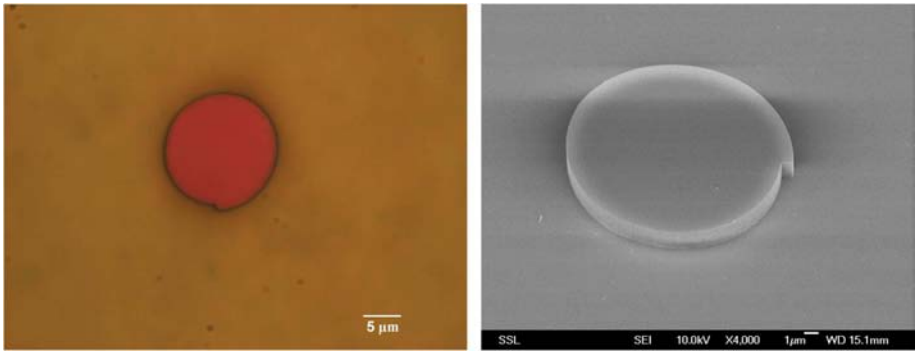

FIGURE 4.23: The optical microscope image of the fabricated spiral laser cavity

photo pumping set-up. The emission from the spiral laser is collected using the 10x objective lens. The Figure 4.24 shows the spectral response of the laser device and the plot of emission intensity as a function pump fluence which gives a lasing threshold of 2.6 $\mu J/mm^2$. The spectrum shows the individual resonance laser lines.

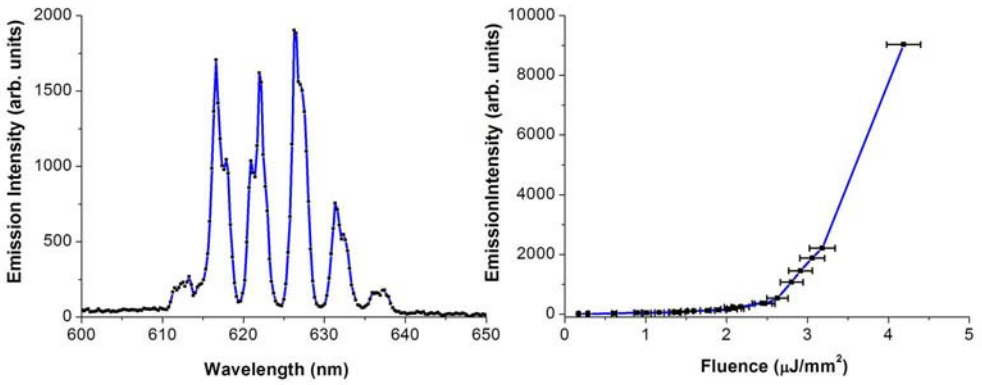

FIGURE 4.24: The figure shows the emission spectrum of the RhB doped SU-8 spiral disk laser above the threshold pump fluence and also the threshold curve

4.2.5.2 Spiral disk resonator with extended waveguide

The spiral disk resonator with extended waveguide cavity design is similar to the spiral laser cavity design mentioned in the previous section. In this design, a waveguide is extended from the notch region of the spiral cavity to confine the laser output to the waveguide region. The output from the laser could be used to integrate with other optical components on chip.

The cavity design is generated using the same spiral equation with a waveguide extended from the notch region which is of same width as the notch and a length equal to r_0. In the present case, the inner radius of the cavity is 100 μm and the ϵ is 0.12. The optical and SEM micrographs are presented in Figure 4.25. The optical characterization is carried out using the free-space photo pumping set-up. The emission spectra from the cavity is collected using the fiber coupled spectrometer and the emission intensity is plotted as a function of input pump fluence and is shown in Figure 4.26 along with the emission spectra of the microlaser at pump fluence above the laser threshold.

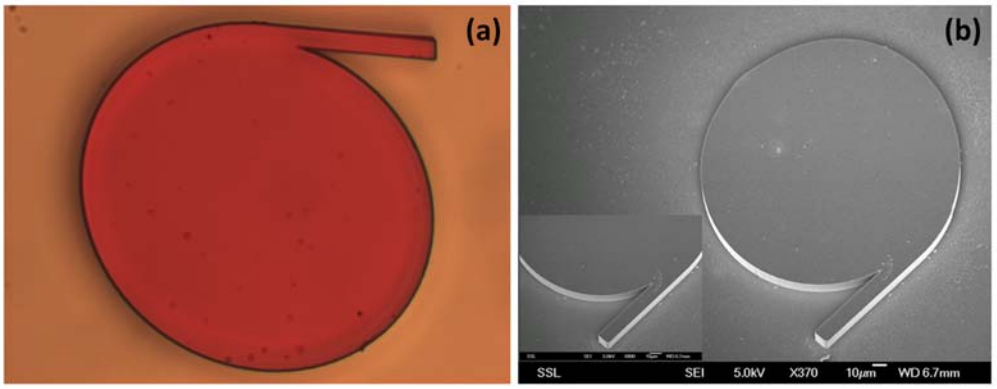

FIGURE 4.25: The (a) optical and the (b) SEM micrograph of the fabricated RhB doped SU-8 spiral disk with extended waveguide

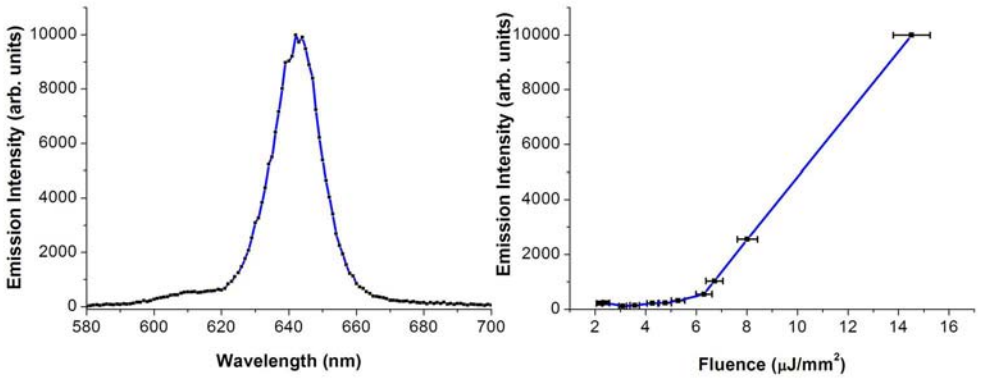

FIGURE 4.26: The figure shows the emission spectrum and the threshold curve of the RhB doped SU-8 spiral disk laser with extended waveguide.

4.2.5.3 Elliptical spiral cavity with extended waveguide

The spiral cavity is further deformed to an ellipse which results in elliptical spiral cavity with extended waveguide. In this design, the waveguide width is chosen as 5 μm. The cavity is designed and fabricated with major axis to minor axis ratio of 2 with major axis dimension of 80 μm. The optical and the SEM micrographs are shown in Figure 4.27. In order to characterize the laser cavity, free-space photo pumping set-up is used and the laser emission spectrum along with the threshold curve is presented in Figure 4.28.

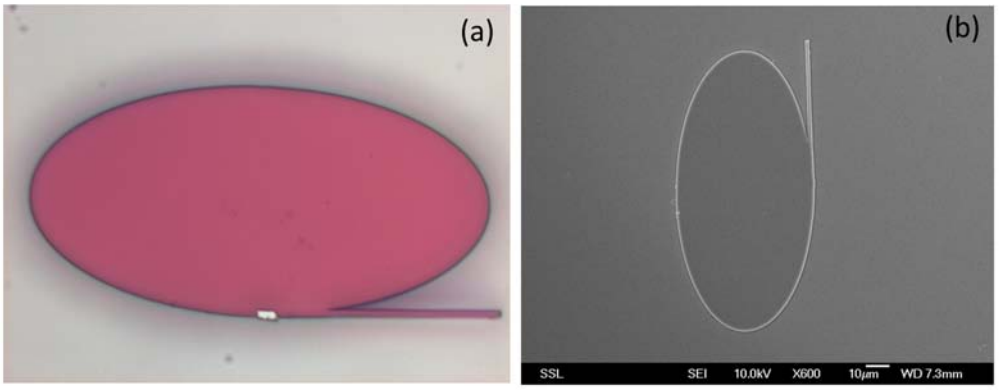

FIGURE 4.27: The (a) optical and the (b) SEM micrograph of the fabricated elliptical spiral cavity with extended waveguide in RhB doped SU-8

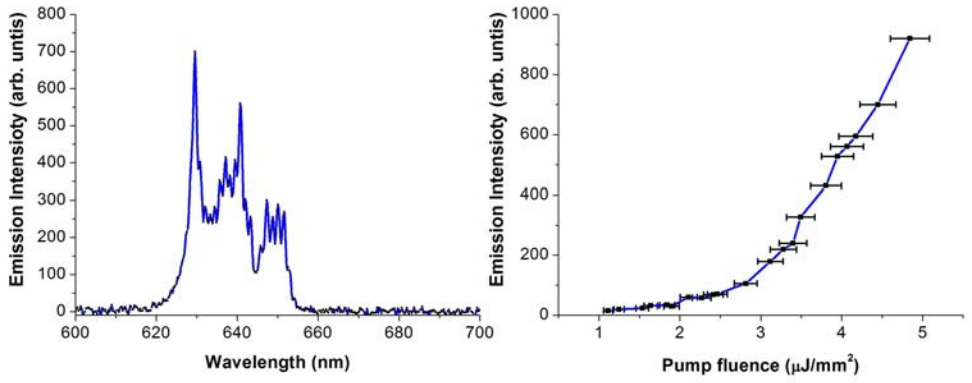

FIGURE 4.28: The emission spectrum and the threshold curve of the RhB doped SU-8 elliptical cavity with extended waveguide

4.2.5.4 Elliptical cavity with deformation at the middle

Apart from the deformation introducing with spiral shape, a notch in the elliptical cavity also introduced to deform the cavity. In this particular case, a wavelength dimension notch is introduced at one end of the ellipse which act as scatterer and this notch scatters a portion of the propagating light inside the cavity to the other

side of the ellipse [106]. Therefore the cavity acts a directional laser.

Elliptical cavity with deformation at the middle is designed by creating the ellipse with its major to minor axis ratio of 1.25 [106]. A deformation is included in the design with the size of the deformation comparable to the wavelength. With such deformation at the middle of the semi minor axis of the ellipse, the emitted light from the cavity is directed opposite to that of the deformation. The effect is pronounced when the size of the deformation is comparable to its wavelength. The geometry of the deformation is independent of the emission direction. The cavity is designed with major axis of the ellipse to be 125 μm and the deformation geometry is a half circle with a radius of 350 nm. The optical and the SEM micrographs of the fabricated laser cavity can be seen in Figure 4.29. To characterize the elliptical

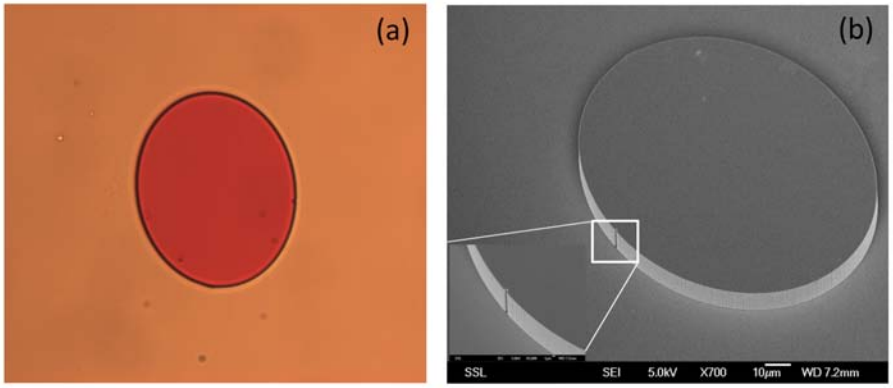

FIGURE 4.29: The (a) optical and the (b) SEM micrograph of the fabricated elliptical cavity with deformation ar the middle in RhB doped SU-8

micro laser the free space photo pumping set-up is adapted. The cavity is photo pumped from the top and the emission is collected in-plane to the cavity from the opposite side that the deformation present. The emission spectra and the plot of emission intensity vs pump fluence can be observed from the Figure 4.30. The threshold fluence for this laser design is 2.75 $\mu J/mm^2$.

In order to investigate the directionality of such directional cavities, a simple cross sectional imaging of the output from the microlaser is implemented. The output of

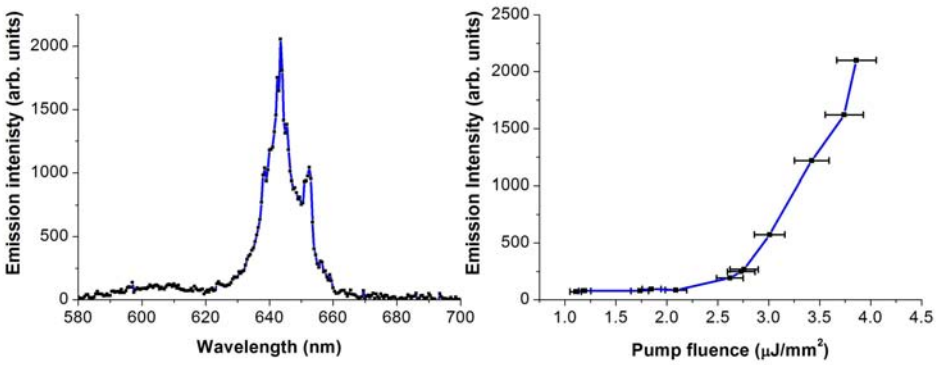

FIGURE 4.30: The emission spectrum and the threshold curve of the RhB doped SU-8 elliptical cavity with notch at the middle

the microlaser is imaged using a CCD camera in the cavity plane with and without the presence of the pump laser and the intensity profile is plotted when the pump laser is turned on. It is clear from the Figure 4.31 that most of the microlaser output is concentrated on the waveguide region which evidences the directional behavior of the spiral disk laser. The similar effect is observed for all the cavity designs discussed.

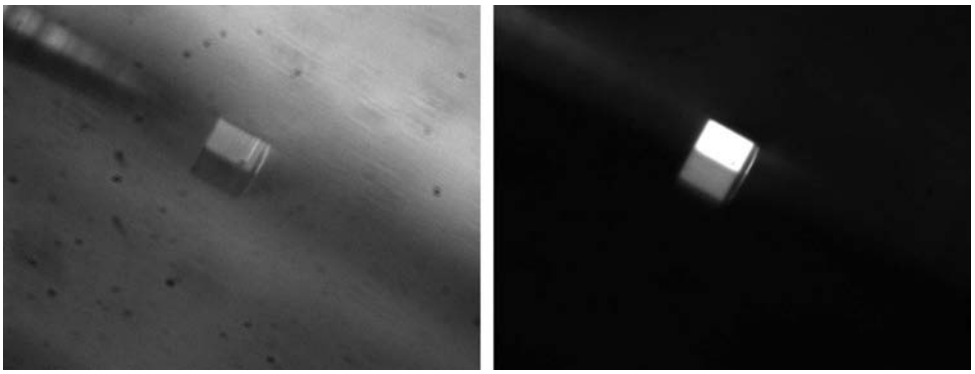

FIGURE 4.31: The directionality of the deformed cavity (spiral with waveguide) can be observed from the cross sectional images taken with (a) pump laser off (b) pump laser on.

4.2.5.5 Coupled cavity microlasers

The elliptical spiral cavity with extended waveguide is fabricated along with an ellipse which is fabricated in the vicinity, 0.5 μm from the laser cavity. The ellipse designed with an aspect ratio of 2, and the major axis dimension of 100 μm with a waveguide width of 5 μm. The SEM micrograph of the fabricated device is shown in Figure 4.32.

The device is optically characterized using the free space photo-pumping set-up

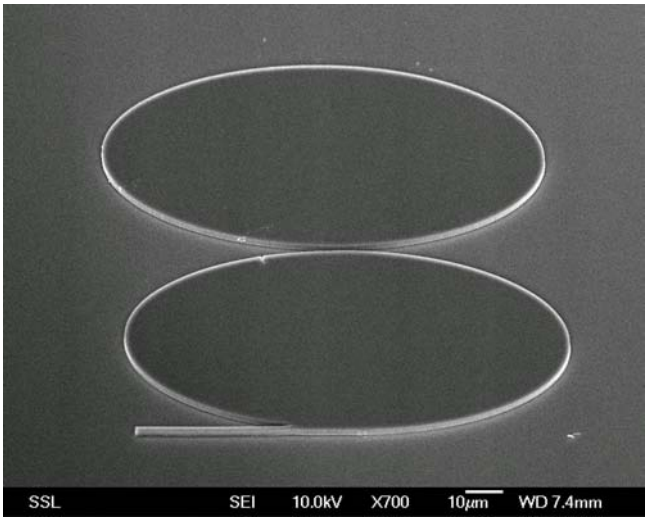

FIGURE 4.32: The SEM micrograph of the RhB doped SU-8 elliptical spiral cavity with extended waveguide coupled to another elliptical cavity in the surrounding

and the spectral response and the threshold curve is obtained and is shown in Figure 4.33. The emission from the coupled cavity laser results in a narrow linewidth laser having 1.5 nm spectral width. The coupled cavity emission spectrum is plotted along with the spectrum obtained for the single cavity of the same dimension to compare the results. As can be seen from the Figure 4.34 only one spectral line is excited in case of the coupled cavity design compared to that of single cavity. The spectra for the two cavities (ellipse and elliptical spiral) is different. The lasing may be observed only for the mode that present in both the cavities.

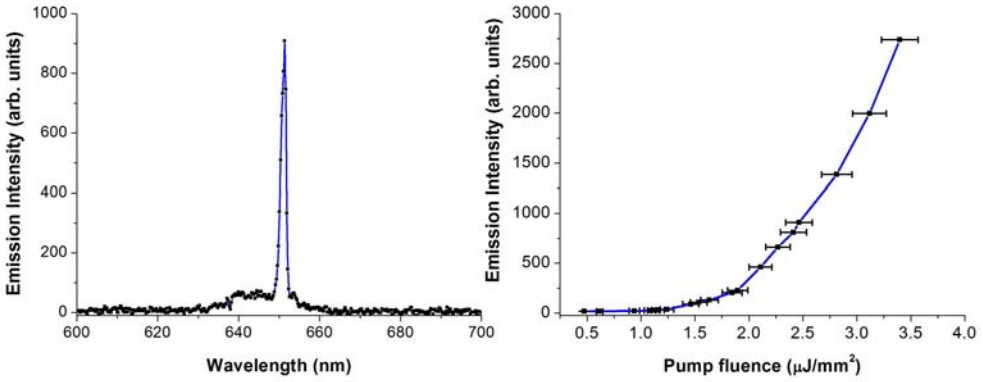

FIGURE 4.33: The emission spectrum and the threshold curve of the coupled cavities fabricated in RhB doped SU-8

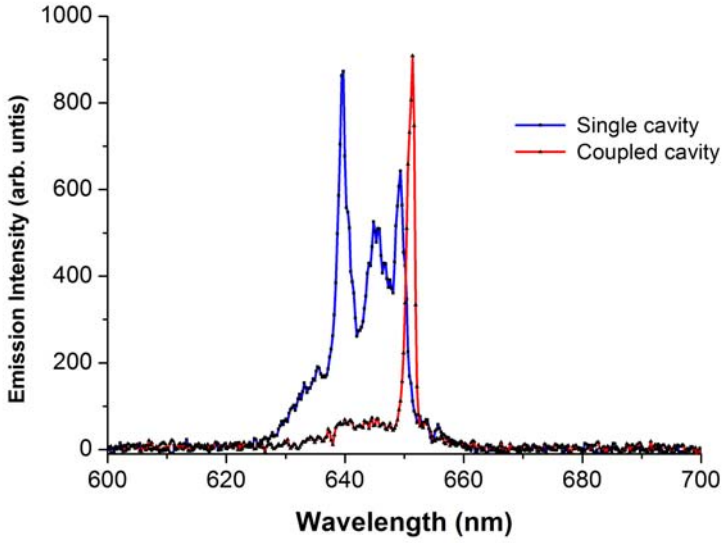

FIGURE 4.34: The figure shows comparison of the spectral response of the coupled cavity and the single cavity

4.2.6 Threshold dependence on cavity parameters

The directionality is achieved in case of the whispering gallery mode microlasers as discussed in the previous section. The threshold fluence obtained for different cavity designs vary from 2 to 7 $\mu J/mm^2$. In this section the threshold dependence is studied by varying the laser cavity parameters.

4.2.6.1 Microlaser thickness dependence

In order to investigate the laser characteristics as a function of thickness of the polymer, the RhB doped SU-8 polymer is prepared to obtain different thickness resists. Three different resist thickness 5 μm, 10 μm and 20 μm RhB doped SU-8 films are spincoated on SiO_2/Si substrate and PBW is used to fabricate the elliptical spiral cavity with extended waveguide of the same dimension. The optical characterization is performed with free space photo pumping set-up and the emission spectra and the threshold curves shown in Figure 4.35 for three different resist thickness.

From the Figure 4.35, it is clear that the laser threshold is independent of the thickness of the resist and the spectral response is changed due to fabrication inhomogeneities.

4.2.6.2 Microlaser dimension dependence

The elliptical spiral cavity with extended waveguide microlasers with major axis dimensions of 40 μm, 80 μm and 120 μm were fabricated in RhB doped SU-8 film using PBW. The microlasers were characterized using the free space photo pumping set-up and the laser spectra and the corresponding threshold curves are shown in Figure 4.36. The results are tabulated in Table 4.4. It can be concluded from the results that the threshold fluence reduces as the dimension of the microlasers increases. Apart from the threshold behavior, the spectral response of the microlaser differs for different dimensions of the microdisk. In case of the the small dimension cavity, the whispering gallery modes can be observed easily because of the large free spectral range. In case of the large diameter cavities, the free spectral range is small.

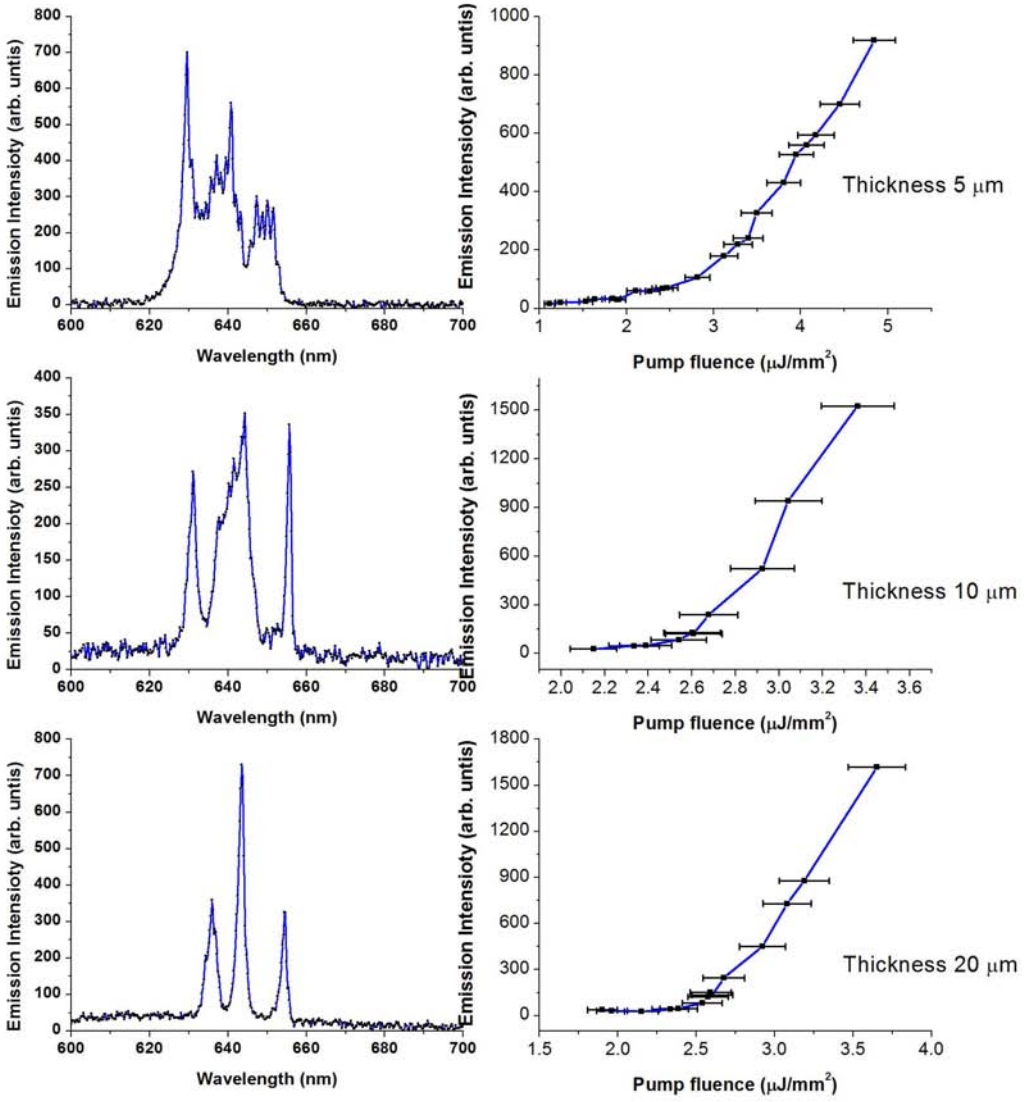

FIGURE 4.35: The emission spectrum and the threshold curve of the RhB doped SU-8 elliptical cavity with extended waveguide for different thickness of the resist indicated on the graph

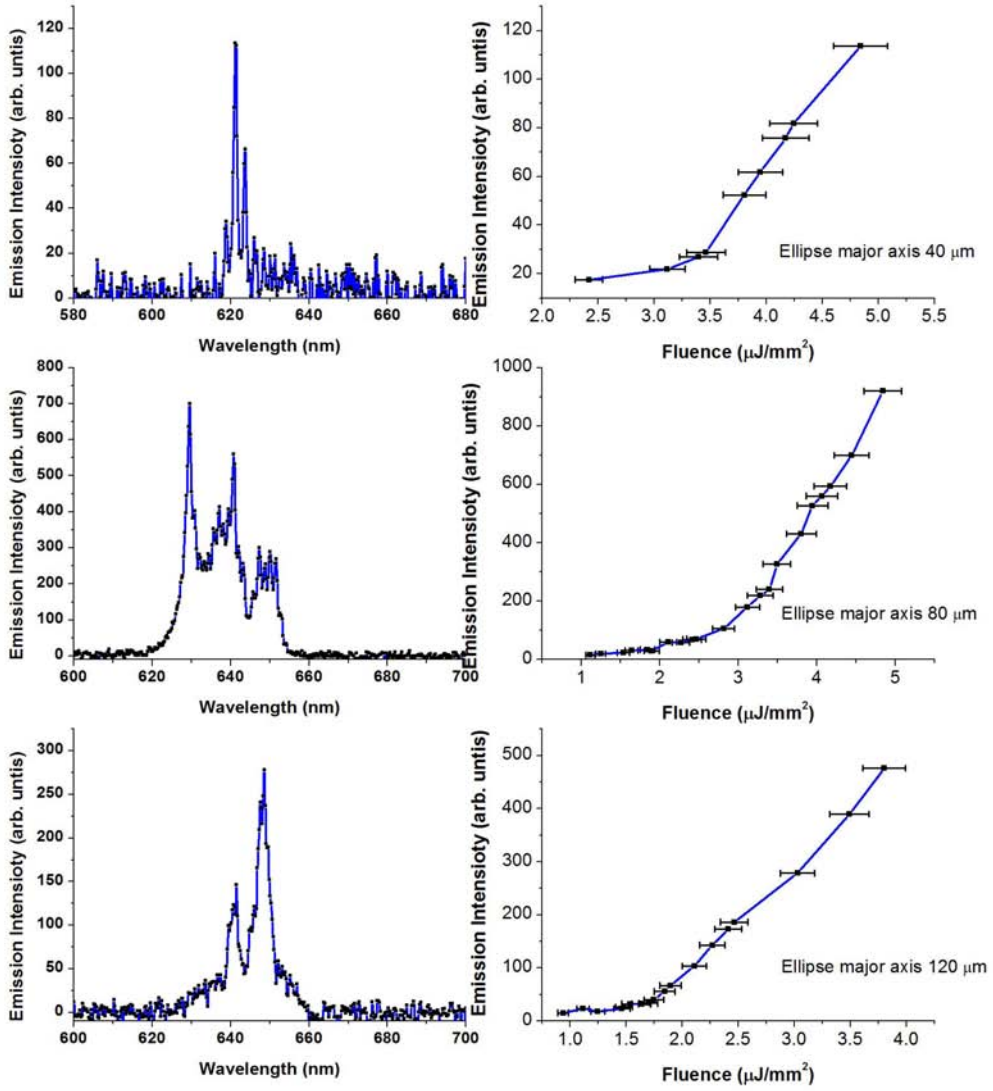

FIGURE 4.36: The threshold curve and the emission spectrum of the RhB doped SU-8 elliptical cavity with extended waveguide for different dimensions of the cavity indicated

4.2.7 Results and Discussion

The gain medium is prepared by simple dissolution of laser dye into the polymer and optimum dye concentration is obtained by the absorption and photoluminescence studies on different laser dyes. The planar microdisk lasers are fabricated in 1 % RhB doped SU-8 and 1 % Rh6G doped SU-8 and photo pumping of these cavities revealed the low threshold behaviour of the 1 % RhB doped SU-8 microdisk laser. Although the low threshold microdisk laser is obtained, the microdisk lasers are non-directional. Various whispering gallery mode cavities are fabricated with different cavity designs which includes a deformation to make such cavities directional. All the laser cavities are optically characterized with photo-pumping of the fabricated devices using a frequency doubled Nd:YAG laser. The cavity designs and the corresponding characterization results are summarized in Table 4.5. From the results, it is clear that the pump threshold fluence for the microdisk lasers is low compared to the different directional cavity designs. This is expected because

Ellipse Dimension (major axis in μm)	Wavelength range (nm)	Threshold fluence ($\mu J/mm^2$)
40	615-625	3.5
80	615-655	2.75
120	635-655	1.75

TABLE 4.4: Dimension dependent laser characteristics

Cavity	Dimension (μm)	Spectral range (nm)	Threshold fluence ($\mu J/mm^2$)
Microdisk	50	630-650	1.0
Microdisk (Rh6G doped SU-8)	50	605-625	1.5
Spiral laser	15	610-640	2.6
Spiral with waveguide	200	620-660	7
Ellipse deformation at middle	100	630-660	2.0
Ellipse spiral with waveguide	80	620-660	2.75
Coupled elliptical spiral cavity	120	648-652	1.75

TABLE 4.5: Summary of results obtained from all the cavities are tabulated, unless specified the gain medium used is RhB doped SU-8

of the reduction in Q-factor as a result of the deformation in the directional cavity designs. The threshold fluence for the directional cavity designs does not vary significantly. The threshold fluence dependence on the cavity parameters are also studied and the results indicate that it is independent of the thickness of the laser cavity and depends on the dimension of the cavity. The threshold fluence decreases with increasing dimension of the cavity. The directionality is achieved in whispering gallery mode lasers which is an important aspect in the present study.

4.3 Summary

Proton beam writing is used for the first time to fabricate the smooth sidewall optical microresonators in polymer SU-8 and the optical characterization of 50 μm diameter microdisk resulted in high Q-factor of 1.1×10^4. Applications based on microdisk resonators such as wavelength filter and microlasers are experimentally demonstrated. By taking the advantage of flexibility of using polymer materials, SU-8 is doped with Rhodamine laser dye to realize microlasers. Further, the study is extended to make the WGM lasers directional with different cavity designs. Circular symmetry in the disk resonator is broken by introducing a deformation in the cavity which helped to achieve directional behavior. Various microlaser cavities are fabricated and characterized optically under photo pumping. The results showed the directionality in whispering gallery mode lasers with low pump thresholds.

Chapter 5

Three dimensional micro disk resonators

Planar whispering gallery mode microresonators have been demonstrated for a variety of applications with different designs which can be integrated directly on to a chip. Though the planar resonators are reported to have high quality factors, issues like surface roughness, lower refractive index contrast between the resonator material and the substrate limit the quality factors. The quality factor of these resonators can be improved further with the fabrication of WGM resonators suspended in air. This improves the optical confinement within the microresonator. In addition, this opens up new possibilities to smoothen the resonator circumference by surface tension forces. Novel resonator designs like the microtoroid could also be potentially fabricated. In this chapter, fabrication of such three dimensional suspended microdisk resonators in different materials is discussed. The same three dimensional microresonators were fabricated in dye doped polymer to reduce the threshold pump fluence of the microlasers.

5.1 Microresonators in silicon

Three dimensional microdisk resonators have already been fabricated in silicon using different fabrication technologies [125–127]. In this section, the fabrication of three dimensional microdisk resonators based on ion beam writing is illustrated. A schematic of the fabrication procedure is shown in Figure 5.1. Proton beam writing of optical components in silicon, particularly optical waveguides are well studied and are shown to have propagation losses $< 1dB/cm$ [40].

Ion beam creates the damage in the silicon crystal and the electrochemical etching

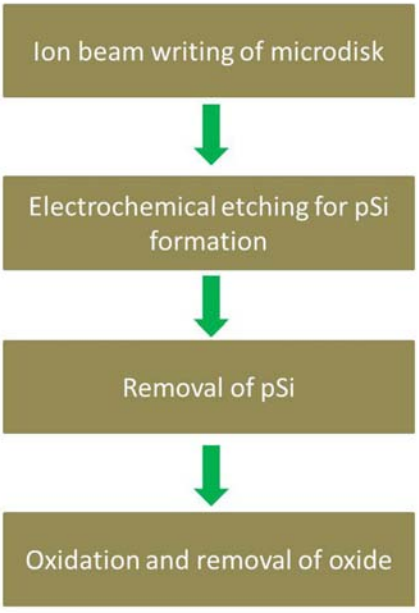

FIGURE 5.1: Schematic representation revealing the fabrication procedure to fabricate the three-dimensional microdisk resonators in silicon

of the silicon in the presence of hydrofluoric (HF) acid results in the formation of porous silicon [128, 129]. The ion damaged region is unchanged and the material surrounding it becomes porous. Since the electrochemical etching is isotropic and the porous silicon formation can be controlled by etching current density and time, a support from the substrate can be formed for the irradiated disk. The porous silicon can then be removed with diluted potassium hydroxide (KOH) which results

in a suspended microdisk resonator in silicon with a support from substrate. The fabrication steps are discussed in detail in the following sections.

5.1.1 Ion beam writing

Proton beam writing is used to fabricate the microdisk resonators in silicon. Depending on the desired thickness of the microdisk, the proton energy and fluence are determined. In the present case, to obtain a microdisk thickness of 2 μm, 375 keV proton energy is chosen. For fabrication, the pre-cleaned silicon sample is first mounted in the 10° beam line target chamber and the focused proton beam of diameter 200 nm is spirally scanned over an area of 50 μm and 100 μm to obtain microdisks with diameters 50 μm, 100 μm respectively.

5.1.2 Electrochemical etching of Silicon

The silicon sample with microdisks fabricated using PBW is then subjected to electrochemical etching in the presence of HF. In this section, the electrochemical etching technique and the inherent mechanism is discussed. Then, the conditions followed to obtain the 2 μm thick microdisk with support from the substrate is described.

Electrochemical Anodization

The electrochemical anodization is performed in an electrolyte containing ethanol and HF with platinum as the negative electrode and an ohmic contact on a p-type silicon sample as the positive electrode. When a bias is applied to these electrodes, the electric field in the etching solution causes the holes to travel to the surface of the silicon sample which causes the pore formation. Many explanations are available for the formation of porous silicon [130, 131]. Platinum is chosen as cathode

since it does not react with HF. Since silicon is hydrophobic, to increase the wettability of silicon, ethanol is added to HF. Ethanol acts as a surfactant preventing the formation of hydrogen bubbles during the anodization.

To perform the electrochemical etching, first the silicon sample is processed to include the ohmic contacts. The 24% HF electrolyte is placed in a plastic beaker and the two electrodes are dipped into the electrolyte. The electrodes are connected to the positive and negative terminals of the DC power supply respectively. The etching rate in the experiment depends on many factors including silicon resistivity, current density, HF concentration and etching time. To optimize the thickness of porous silicon, the same p-type silicon sample is etched using with same resistivity and current for 5 min. The sample is cleaved and characterized using SEM. SEM shows that a layer of 10.9 micron is formed. This implies that for an electrochemical etching current density of 60 mA/cm^2, a p-type medium resistivity silicon wafer (1-10 Ωcm^{-1}) in 24% HF solution will etch at a rate of 2.16 $\mu m/min$.

The proton irradiated silicon sample is processed with ohmic contacts and the electrochemical etching is performed in a 24 % HF solution for 7 min to form a layer of porous silicon about 15 μm in thickness from the surface. Since the electrochemical etching process is isotropic, a support with a width of 20 μm in the case of the 50 μm diameter disk and 70 μm in the case of the 100 μm diameter microdisk.

Removal of Porous silicon

A 15 μm porous silicon layer is formed on the silicon substrate after the electrochemical etching. The porous silicon is removed using the diluted KOH solution and the sample is rinsed for a few minutes to completely remove the pores formed in the silicon sample. After the removal of porous silicon, the free standing silicon microdisk structures supported from the substrate are obtained.

Oxidation as final step

The electrochemical etching roughens the surface of the microstructure during the etching process. It is essential to smooth such structures for optical applications. To smoothen the surface of the microdisk resonators, the sample is oxidised to form

an oxide layer on the surface of microstructures. The removal of the oxide layer in the diluted 2% HF solution results in smooth free-standing microdisk resonators supported from the substrate.

5.1.3 SEM characterization

The fabricated microdisk resonator was characterized using SEM. The SEM micrograph is obtained from top view as well as the tilted view to obtain parameters like diameter of the disk, thickness of the disk and the substrate to disk separation. The microdisk resonators were fabricated with different proton fluence and are characterized using SEM microscopy. The lowest disk thickness obtained was 1.5 μm for a proton fluence of 5×10^{14} $ions/cm^2$. The fabricated microdisk resonator can be seen in Figure 5.2. The microdisk resonator thickness can be further reduced by optimizing the proton energy and the fluence.

5.2 Microresonators in Lithium niobate

Lithium niobate (LN) is a well-known optical material which has electro-optical properties, a wide transmission band (350 nm -5.2 μm), good thermal stability, and is resistant to optical damage [132]. These properties make LN applicable for a wide range of optical applications which have already been demonstrated [133–138]. Although LN has good optical properties, its use is limited because of difficulties encountered in fabricating structures in this hard, difficult-to-etch glassy substance.

5.2.1 Review on Microresonators in Lithium niobate

In spite of the difficulties, fabricating structures in LN, microresonators have been realized in LN due to its interesting material properties [139]. Microring resonators

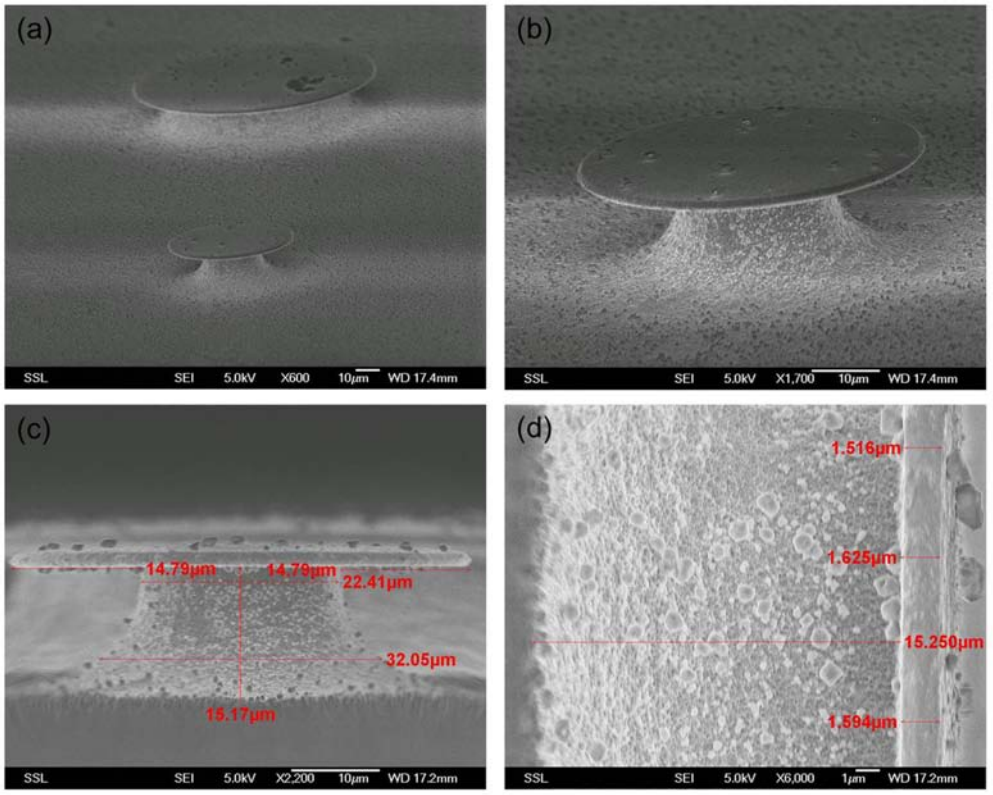

FIGURE 5.2: The SEM micrograph in different angles showing the dimensional parameters like microdisk diamter, thickness and the separation from the substrate

were fabricated in thin slabs of LN formed using crystal ion slicing technique by Guarino et al [140]. In that particular work, the ion implantation was carried out to form the damaged layer underneath the surface of LN. The damaged layer was then removed using chemical etching to form the thin membrane of LN [141]. Photolithography and reactive ion etching (RIE) were used to define the microring resonator in the thin membrane. The high index contrast was achieved by wafer bonding the micro structures fabricated in LN to a low index material. A mask aligner was used to position the waveguide with a submicron separation from the microring resonator. Despite the difficulty in fabrication, the quality factor obtained using this technique was 4×10^3. The resonance frequency shift obtained using the device was 0.14 $GHzV^{-1}$. The limited quality factor of the device might have resulted from imperfections on the surface produced by crystal ion slicing and the

RIE etching of the thin membrane of LN. Koechlin et al. used a similar fabrication procedure to make a micro ring resonator in LN. In this work the ring was transferred to a sapphire substrate with a GaN waveguide through a mechanical aliment procedure [142]. The quality factor achieved for this resonator was also limited and is 4.3×10^3. In a more recent study by Nunzi Conti et al. disk resonators were fabricated in LN using core drilling and polishing of the edge of the 4.7 mm diameter disk resonator systematically to obtain the spherical sidewall profile. The disk resonator was optically characterized using a planar waveguide fabricated in LN and aligned in close proximity during optical characterization. High quality factor of 1.3×10^8 is exhibited by this disk resonator [143]. Although this resonator showed ultrahigh quality factor, the dimension of the disk resonator is too large for the integrated optics applications.

Here we propose an alternative and simpler method that utilizes ion implantation followed by focused ion beam (FIB) milling and inductively coupled plasma (ICP) etching to form the suspended microdisk resonators in LN. The ion beam creates damage at the end of the ion range. This damaged region become chemically active and can be etched away using a chemical etchant and forms a thin membrane of LN. FIB milling and ICP etching is then used to define the microdisk structure in LN.

5.2.2 Production of thin slabs in lithium niobate

High energy ion beams typically from 100 keV to several MeV can penetrate several microns into a material and create maximum damage at the end of the ion range, leaving the surface layer relatively undamaged. The penetration depth at which the maximum damage layer exists can be controlled using an appropriate ion energy. The amount of damage or vacancy density at the end of range can be controlled by the incident ion fluence. For LN a fluence ranging from 1×10^{15} to 5×10^{16} $ions/cm^2$ is typically used to create the buried damaged layer [144, 145]. To optically isolate

the LN slab from the substrate, multiple ion energies can be used to increase the buried implantation layer width.

In the present experiment, He^+ ions are used to create the damage with the ion fluence of $1{\times}10^{16}$ $ions/cm^2$ over an area of 1×1 cm^2 using large area irradiation facility at the Centre for Ion Beam Applications, National University of Singapore. The LN sample is prepared by evaporating a thin metal layer on the surface to minimize the charging effect induced during the implantation process. The LN sample with 10 nm Au on the surface is placed in an extension tube which is 1 m away from the target chamber. The area of irradiation is adjusted by observing the beam from a fluorescent screen arranged at the end of the extension tube. The actual beam current is calculated using the secondary electron suppression method from which irradiation time is calculated for the desired ion fluence. In this experiment, two different thickness of the thin slabs are produced and in each case, three different ion energies are used to obtain an implantation depth of approximately 1 μm. A 1.7 μm thick slab with 1 μm damaged layer are produced with 1, 1.1 and 1.23 MeV energies, and for the 700 nm thick slab 400, 500 and 650 keV energies are used. The ion energies are calculated from the SRIM simulations. The ion damage profile for two different scenario are plotted together and shown in Figure 5.3. The energies are chosen to have the proper overlap of the damage created in the LN crystal. Absence of such overlap leaves undamaged LN crystal in between these damaged layers.

The damaged layer created by ion implantation is chemically active and can be removed using a dilute acid solution (1:2 ratio of 49% HF and 65% HNO_3). This leaves the undamaged slab of material on top with thickness of about 1.7 μm and 700 nm. In order for the chemical etchant to access the damaged layer two different methods can be followed.

(1) Focused Ion Beam (FIB) milling

FIB milling is one of the most attractive techniques for the fabrication of micro or

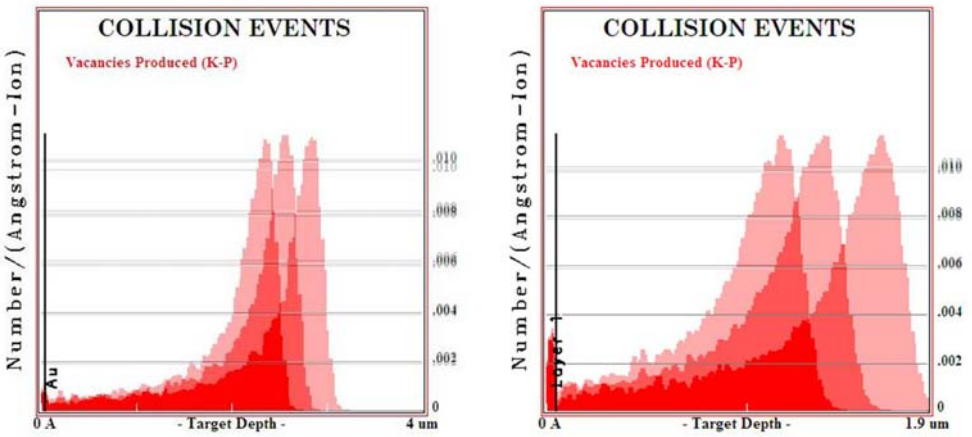

FIGURE 5.3: The image showing the damage profile of the three different energies which showing a clear overlap of the ion damage (a) in the case of 2 μm thick LN and (b) in the case of 700 nm thick LN

nano patterns in most dielectrics without any mask. A beam spot size as small as 5 nm can be achieved regularly [146]. In the present case, FIB milling is used to form a trench in the He^+ implanted LN in order for the dilute acid solutions to reach the buried damaged layer. FIB is used to mill the desired trench pattern with a beam current of 100 pA and the acceleration voltage of 30 kV. The large current used in this experiment can help to reduce the milling time, which reduces the re-deposition of material onto the sidewalls. After the square trench is formed using FIB, the sample is subjected to a chemical etching step in dilute acid (1:2 ratio of 49% HF and 65% HNO_3) for few minutes to remove the damaged layer and a thin slab is observed, isolated from the substrate. The etching rate of the damaged layer is approximately 100 nm/min, whereas the etching rate of the surface layer which has a relatively low damage is negligible. The SEM micrographs of the fabricated thin slabs of 2 μm and 700 nm are shown in Figure 5.6.

(2) Inductively Coupled Plasma (ICP) etching

The second method to access the implantation created damage layer is to use ICP etching. Though FIB is efficient in fabricating micro or nano structures with beam spot sizes less than 5 nm, this technique can not be applied to large areas [147].

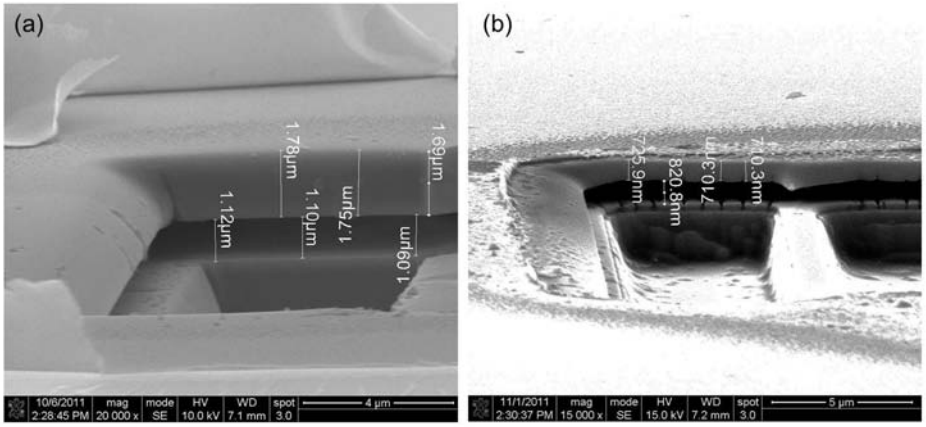

FIGURE 5.4: The image showing (a) the thin slab of 1.7 μm with an air gap of 1.1 μm and (b) a thin slab of approximately 710 nm is obtained with an air gap region of 820 nm

ICP etching can be used for large areas and with the aid of a mask pattern, it can be used for mass production. To create a trench with ICP etching, first, the trench pattern is defined using standard photolithography. To form the trench pattern, the positive photoresist (AZ5214E) is first spincoated onto an implanted lithium niobate sample. Then the patterns are created on the sample using a photomask and UV exposure. Chromium (Cr) is then used as the etch mask due to its hardness (Mohs hardness of Cr is 8) when compared to various metals. Cr helps prevent strong ion bombardment during etching and gives high selectivity. In addition, Cr can lead to better surface quality (post-etch) and also can be easily removed using a commercial Cr etchant. In this work a 300 nm Cr film was deposited onto a $LiNbO_3$ sample using an Edwards Auto 306 electron beam evaporator, and patterned through a lift-off process.

Plasma etching was performed in a Plasma Therm SLR 770 ICP system. An 8-inch Si carrier wafer was used to move the samples from the loadlock into the reactor chamber. Before the ICP etching, O_2 plasma was performed for 15 min to clean the chamber. The gas composition can significantly affects the ultimate etching rate, smoothness, and anisotropy. Argon was added to the fluorine-based gas which can increase the physical etching component and enhance the anisotropy. It is found

that the etching profile can be optimized at a chamber pressure of 7.0 $mTorr$, 90 W RIE power and 800 W ICP power. A perfect rectangular structure with a sidewall slope angle of 90° was achieved [148] in LN as shown in Figure 5.5. After the ICP etching, the sample can be immersed in chemical etchant (1:2 ratio of 49% HF and 65% HNO_3) for few minutes which will result in suspended structures.

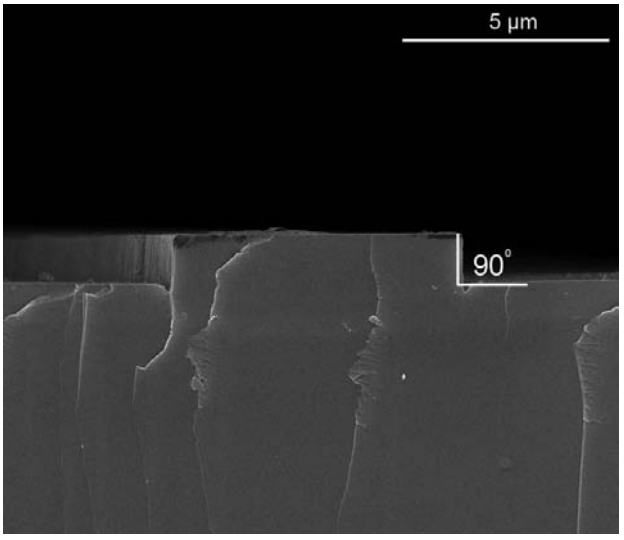

FIGURE 5.5: The lithium niobate microstructure fabricated using ICP etching showing the vertical sidewall feature.

5.2.3 Microdisk resonator in lithium niobate

To fabricate the suspended microdisk resonator in LN, the same LN sample is used with a 1.7 μm thick slab and a ring pattern is milled using FIB to gain the access to the implanted layer for chemical etching. FIB is used to mill the ring shaped trench in the implanted sample with a ring width of 4.5 μm and an outer diameter of 18 μm. This allows the etchant to access to the implanted region. The sample is then placed in the chemical etchant for few minutes to undercut the microdisk in order to isolate it from the substrate. In this process, a microdisk of 13.3 μm diameter with thickness of 1.7 μm is achieved and the SEM micrograph is shown

in Figure 5.6. From the image, it is clear that the disk resonator is separated from the substrate by about 1.1 μm which is sufficient for optical isolation.

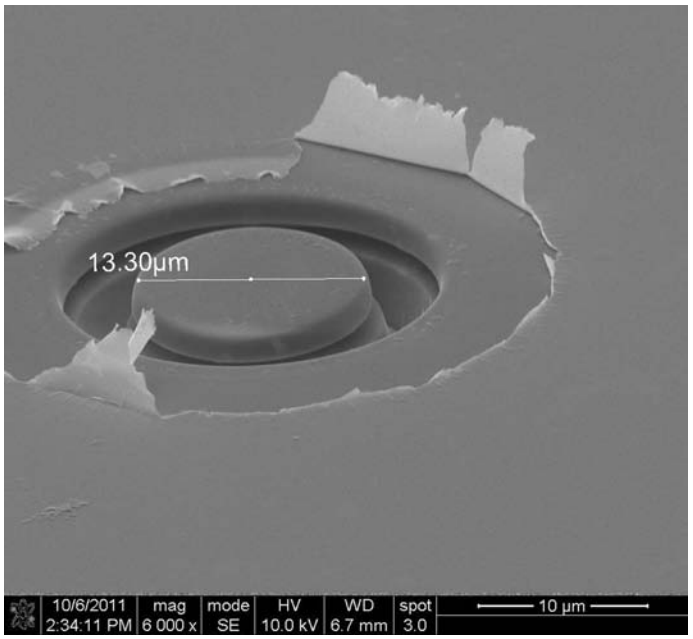

FIGURE 5.6: The suspended microdisk resonator of 13.3 μm diameter fabricated in lithium niobate.

The microdisk resonator thickness can be reduced by controlling the ion bean energies used in the implantation step. As mentioned earlier, the damage profiles of different ion energies have to overlap. By carefully defining the first two energies to have a separation between the two damage profiles, a thin membrane of lithium niobate can be produced with almost the same energies used in the current experiments. With this method, the slab thickness can be obtained as low as 100 nm [149]. After the implantation, the top layer in the lithium niobate can be removed through chemical etching by carefully creating a trench to reach the end of range of the first energy used in the experiment. This leaves the ultrathin layer of lithium niobate on the surface. To demonstrate the effect, an experiment was performed with He ion implantation of three energies 1, 1.15 and 1.25 MeV. The subsequent

trench formation and the chemical etching resulted in a 200 *nm* thick slab in between the damaged regions (air gaps in the image) which can be seen from the SEM micrograph in Figure 5.7.

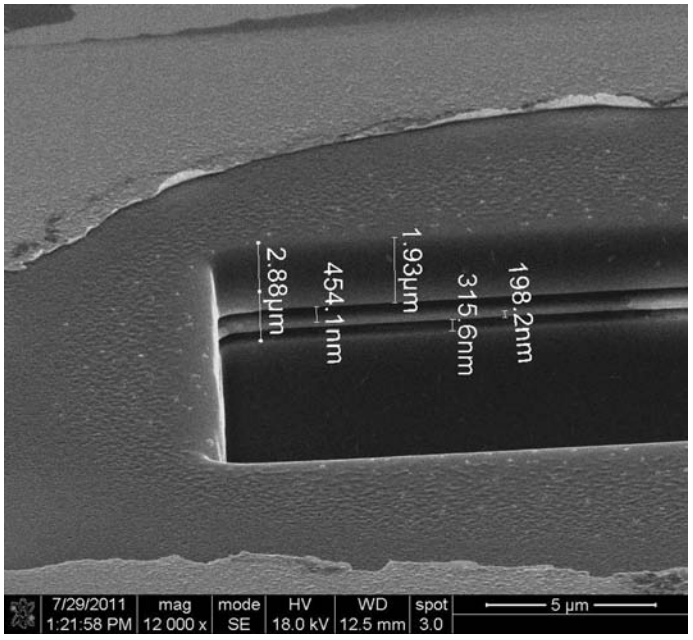

FIGURE 5.7: The thinner slab of 200 nm can be observed in between the top 2 μm slab and the substrate.

5.3 Microresonators in SU-8 photoresist

Microresonators have been extensively studied in the negative tone photoresist like SU-8 because of its optical properties and its compatibility with standard lithography. Planar microresonators have been produced using a variety of fabrication technologies including proton beam writing, as illustrated in Chapter 4. Planar microring resonators surrounded by a low index material have the highest quality factor of 10^5. Suspended microresonators however, cannot be easily fabricated using tools that are commonly available. In this section, the fabrication of the three dimensional SU-8 microresonators is discussed.

5.3.1 Fabrication

Proton beam writing is capable of three dimensional micro structuring, where the depth in at which a material is modified is controlled by the proton energy. Therefore, in order to form a suspended three dimensional cavity two different proton energies are required for the fabrication. Low energy protons are utilized to create the desired cavity and high energy protons are used to form the support structure from the substrate.

In this work, proton beam writing is used to fabricate two designs of microcavities: a micro disk resonator and a spiral micro cavity with extended waveguide. The end of range of protons for different energies in SU-8 is calculated using the SRIM Monte Carlo simulation software. From the SRIM simulation, as shown in Figure 5.8(a), in order to fabricate a 5 μm thick microcavity, the proton energy should be 375 keV. The fabrication of the pedestal can be achieved using high energy protons (2MeV).

The sample is prepared by spin coating a 25 μm thick SU-8 layer on a clean silicon

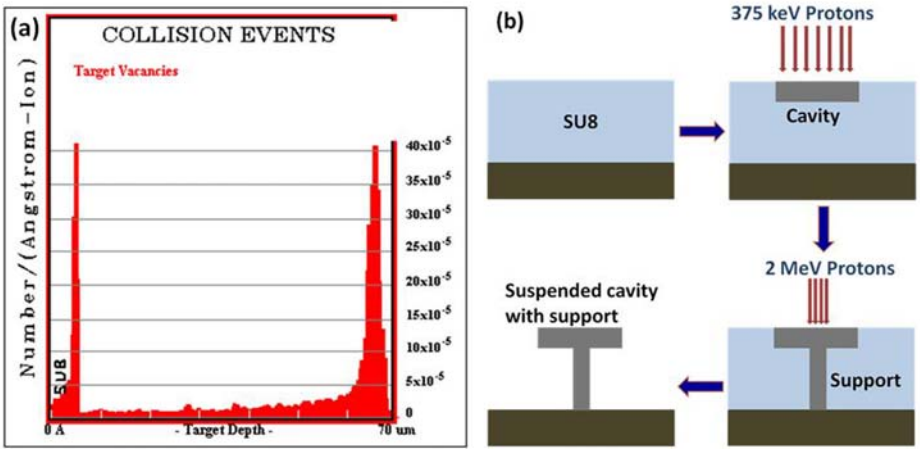

FIGURE 5.8: (a)The SRIM calculations showing the proton end of range in SU-8 and (b) the schematic showing experimental procedure for the fabrication of suspended microdisk

substrate. As shown in the schematic diagram (Figure 5.8(b)), first 375 keV protons are used to fabricate the microcavity. The 375 keV protons are focused down to a

100 nm spot size and the proton beam is magnetically scanned in desired design to obtain the microcavity. In the second fabrication step, 2 MeV protons are used to pattern a pedestal that is required in order to support the cavity fabricated with low energy protons. For both structures, the SU-8 was irradiated with a proton fluence of 40 nC/mm^2. In order to correct for the stage movement over the time, first the focused 375 keV proton beam is used to image a specific location of grid with scan area of 5 μm. Later when operating with high energy protons the same grid image is reproduced by adjusting the stage position. In this process the stage movement can be corrected. After the two energy irradiation, the sample is chemically developed using the standard SU-8 developer which removes the unirradiated SU-8, resulting in a suspended micro cavity. Using the same experimental procedure two different cavities: a disk resonator and a spiral cavity with extended waveguide are fabricated. Figure 5.9 shows an SEM image of the tilted view of the two cavities that are isolated from the substrate

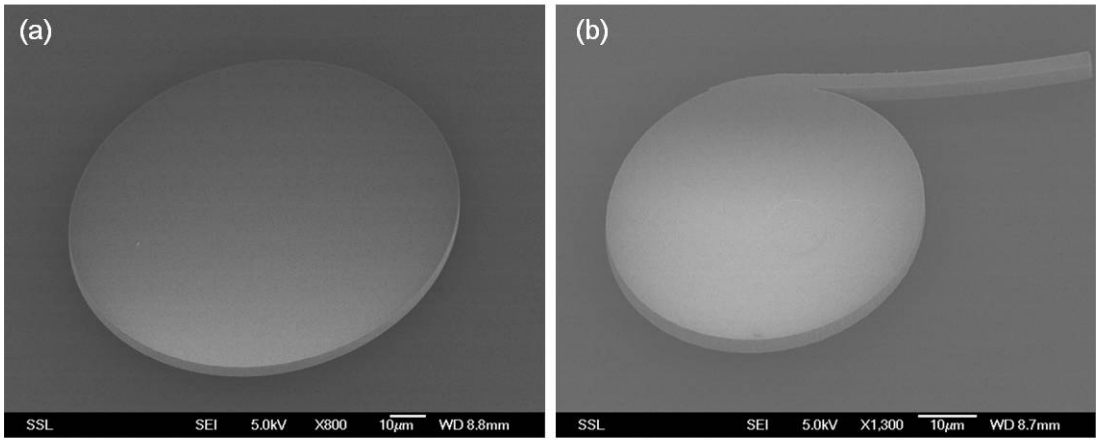

FIGURE 5.9: SEM micrograph of the fabricated (a) microdisk resonator (b) spiral disk resonator with extended waveguide using PBW

5.4 Three dimensional microlasers in dye doped polymer

Focused proton beam writing is used to fabricate a three dimensional microdisk resonator in a dye doped polymer to demonstrate its potential application as a microlaser.

5.4.1 Fabrication

A 25 μm thick Rhodamine B doped SU-8 layer on a silicon wafer is prepared using the same preparation method discussed in Chapter 4 (section 4.2.2.1). The focused 2 MeV protons were used to fabricate the support for the suspended laser cavities. A beam of 2 MeV protons were focused down to a 100 nm spot both in the horizontal and vertical directions. The proton energy is reduced to 200 keV in order to achieve a laser cavity thickness of 2.5 μm. The 200 keV protons are also focused down to 150 nm both in the horizontal and vertical directions. Then, the focused 200 keV proton beam is magnetically scanned to irradiate the desired cavity design at the same position as the support. After the proton irradiation, chemical development is carried out to remove the unirradiated resist which results in a three dimensional suspended cavity supported on the substrate. Different cavity designs, discussed in Chapter 4, are fabricated suspended with a support from the substrate.

The SEM micrographs of the fabricated suspended disk microresonators, spiral disk and spiral disk with extended waveguide are shown in Figure 5.10. All the microlasers are fabricated using a with scan size of 20 μm and with a support of 5 μm in diameter.

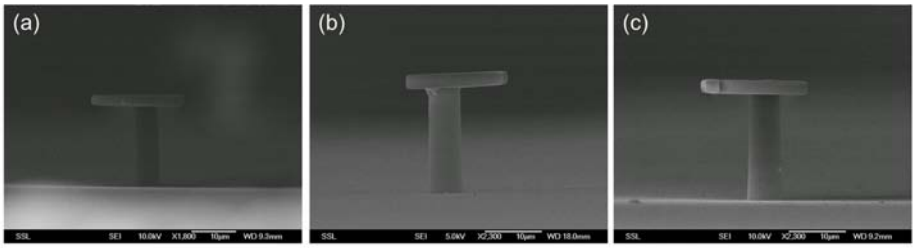

FIGURE 5.10: SEM micrographs of the fabricated suspended microlasers (a) microdisk (b) spiral disk (c) spiral disk with extended waveguide.

5.4.2 Results and Discussion

All the microlasers are optically characterized using a pulsed laser of wavelength 532 nm. Using a visible camera, the optical images are obtained for each microlaser with and without the presence of the pump laser. The obtained cross sectional images of the suspended lasers are shown in Figure 5.11 which clearly shows the directional behaviour of these microlasers. The emission intensity in the case of the spiral disk, spiral disk with waveguide and the elliptical cavity are confined to a small region when compared to the microdisk laser where the emission is uniform. This shows the directionality of such laser cavity designs. The microlaser emission spectrum is measured using a fiber-coupled spectrometer for each cavity design. The threshold calculations have been performed using the pump fluence dependence of the microlaser emission obtained by varying pump fluences. The emission spectra and the corresponding threshold plot for each microlaser is presented in the Figure 5.12 and the results are tabulated in Table 5.1.

The suspended microlaser performance is compared with the planar microlasers of the same dimensions. A decrease in the laser threshold fluence is observed for all the cavities. This improvement in laser threshold is attributed to the fact that the microresonator quality factor increases due to the increased refractive index contrast. The surrounding air medium for the suspended cavities acts as alow index cladding layer. The quality factor of the suspended microresonator has not been measured by direct transmission experiments, but the reduction in suspended

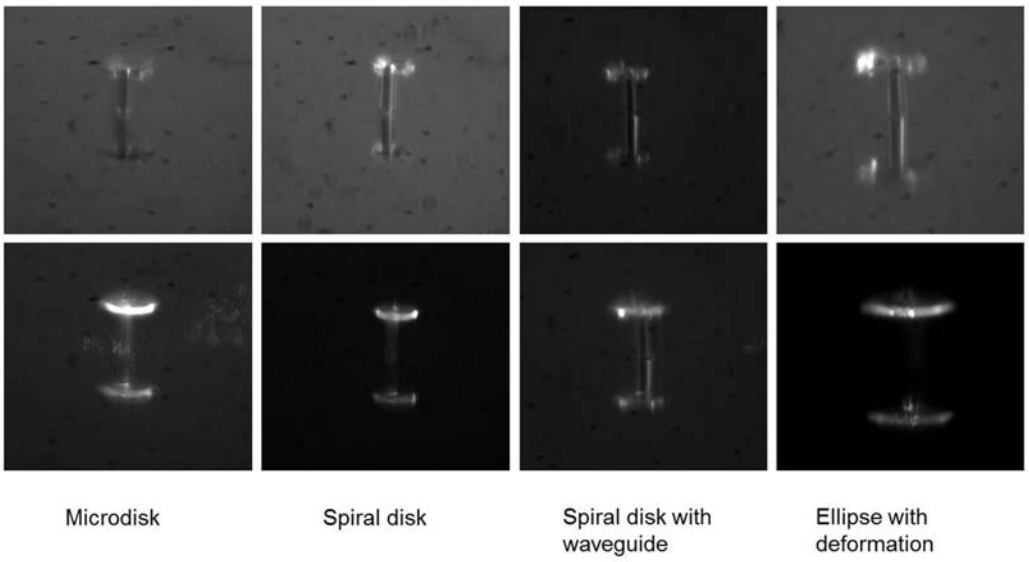

FIGURE 5.11: The emission intensity profile obtained in-plane to the sample (a) microdisk (b) spiral disk (c) spiral disk with extended waveguide (d) elliptical resonator with deformation in the minor axis.

Cavity	Dimension (μm)	Threshold fluence ($\mu J/mm^2$)	
		2D cavity	3D cavity
Microdisk	20	1.0	0.5
Spiral laser	20	3.5	1.2
Spiral with waveguide	20	5.2	2.4
Ellipse deformation at middle	30	2.5	1.4

TABLE 5.1: Summary of three dimensional laser cavity characteristics fabricated in Rhodamine B doped SU-8

microlaser threshold infers that the suspended microlasers have a higher Q-factors compared to planar microlasers.

The suspended microlasers have a laser threshold approximately one half of the threshold obtained for planar microlasers. Although there is improved laser performance due to better optical confinement, the microlaser sidewall is not straight because of the low energy proton beam writing which may result in reducing the quality of the microresonator. To observe the surface quality of the backside of the cavity, the disk is rotated using an optical fibre. The SEM image in Figure 5.13 shows that the sidewall of the suspended cavity is not vertical. For the fabrication

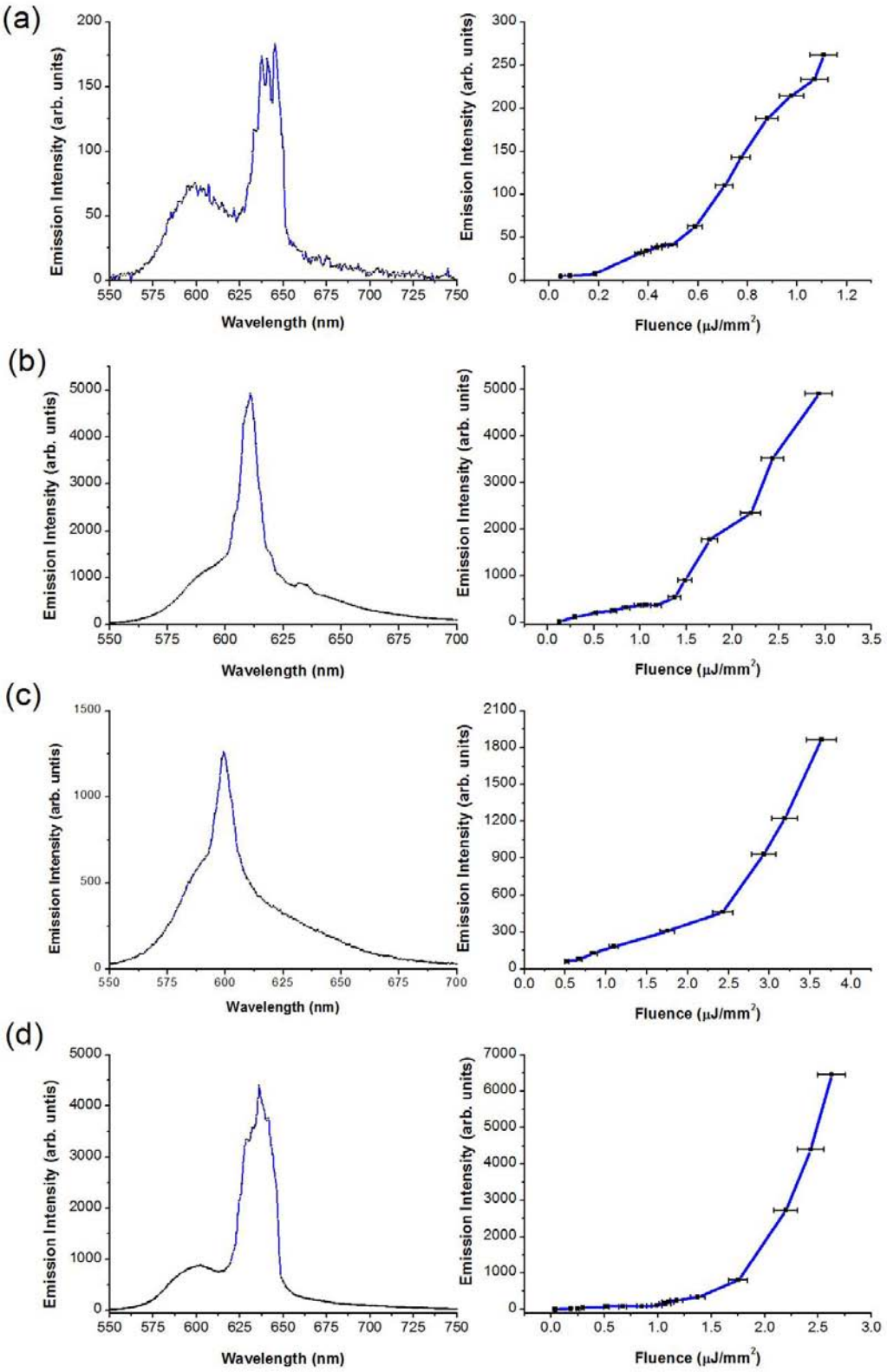

FIGURE 5.12: The laser spectra and the threshold plot for each suspended micro-laser (a) microdisk (b)spiral disk with notch (c) spiral with extended waveguide (d) ellipse with deformation at the middle.

of suspended microresonator, both electronic and nuclear damage is used which effects the sidewall profile. The front and backside of the cavity is imaged through SEM microscopy and it is observed from the SEM images that the backsurface of the microlaser is as smooth as the front surface, which is obtained directly from the spin coating.

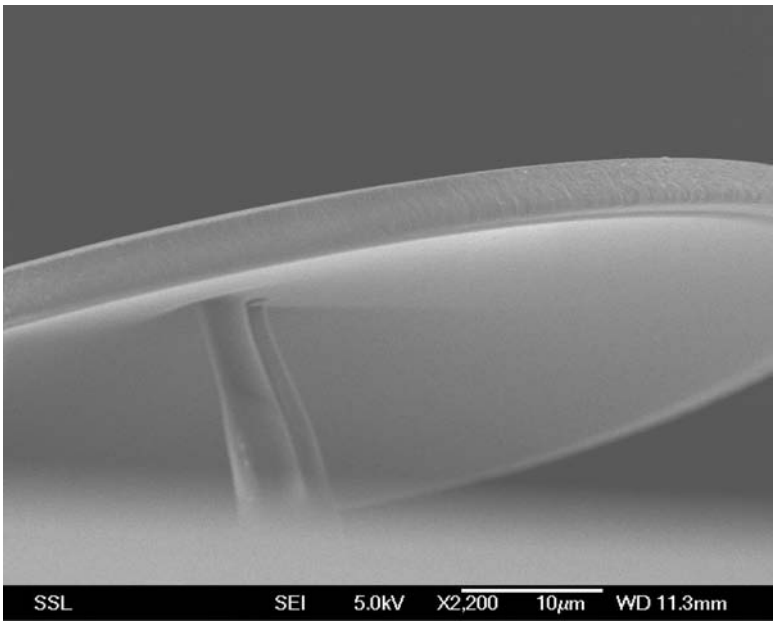

FIGURE 5.13: The SEM image showing the sidewall profile of the microlaser

5.5 Summary

Three dimensional microdisk resonators were fabricated in different materials using ion beams with different post processing steps depending on the material used. Resonators were fabricated in materials like silicon, lithium niobate and SU-8 photoresist. Though not all the characterization has been performed to measure the resonator parameters, based on the results it could be expected that these cavities exhibits higher Q-factors compared to planar cavities which is also evident from the results obtained from suspended microlasers. The suspended microlasers showed improved laser performance over the planar microlasers.

Chapter 6

Optical modification of materials through Ion implantation

Energetic ion beams have many applications including lithography and material modification. Ion implantation is a well known material modification technique, widely used in the semiconductor industry to introduce dopants into the semiconductors. Ion beams, upon traversing through the material, participate in interactions with the local atomic environment and transfer their energy to the atomic system, which ultimately results in local modification of the material. The lattice damage that occurs during the implantation sometimes results in a change in the physical, chemical, electronic and optical properties of the material which have applications in different research fields. In this chapter, ion implantation together with lithography has been used to create implantation damage confined to microstructures within single crystal materials. The optical modification was observed and is used for the optical waveguide applications. The same technique was implemented for nonlinear optical crystals which also resulted in confined optical waveguides and waveguide lasers.

6.1 Modification of Diamond with proton implantation

Diamond is an outstanding material which has remarkable physical, chemical and optical properties. Diamond is the hardest natural material with the highest Youngs modulus (1050 GPa) and has the highest thermal conductivity. Diamond is chemically inert and bio-compatible. Optically, diamond has one of the widest optical transparency windows of any material ranging from the deep UV (λ=200 nm) all the way up to terahertz frequencies (λ =100 μm) [150–153]. Furthermore, due to its large band gap (5.495 eV), more than 500 optical light emitting centres have been documented in diamond. Although diamond has attractive properties, its application in research is limited because of high cost and the lack of high quality substrates. In recent years, high quality single crystal diamond substrates with precisely controlled impurity concentrations have been manufactured with the help of the chemical vapor deposition (CVD) method [154, 155]. Synthetic diamond substrates grown using CVD can now be produced with consistent optical and electrical properties. The availability of high quality low cost substrates has reignited interest in diamond for various applications.

One issue that still remains is that micro machining of diamond is challenging due to its mechanical hardness and chemical inertness. Micro machining is important for practical applications in all fields especially for optical integrated circuits. Only ion beam related techniques have the capability of micro patterning diamond. Microstructures can be fabricated in diamond using two methods. Firstly, the micro structures are patterned on a photoresist, then the structures are transferred to diamond using inductively coupled plasma etching and the subsequent resist removal leaves the micro-structures in diamond [156]. This micro/nano structuring is only applicable for fabrication of ridge structures such as ridge waveguides. The same method was also used to form the nanopillars which were used to isolate single

color centres (NV center) in each nano-structure [157]. However, this method is not applicable for all optical applications because of the substrate loss [158, 159]. The second method is to combine ion implantation and focused ion beam (FIB) milling to generate the micro/nano structures isolated from the substrate. Ion implantation above a certain fluence changes the diamond substrate from diamond to graphite which is chemically active. The removal of graphite leaves behind thin membranes of diamond isolated from the substrate. The energies of the ion beams can be controlled to obtain the desired thickness of the diamond membranes. Later FIB can be used to pattern the desired micro/nano structures in the thin membranes of diamond [149].

In addition to these physical patterning techniques, ion beams have recently been used to locally modify the optical properties of diamond at the micron level [160]. PBW has the potential to generate optical micro-structures in diamond at a specific depth from the surface, which can also be used for dense integration of optical components in the substrate. Although previous work on optical waveguides in diamond have verified that waveguiding does occur in the implanted areas, no information on the quality of the waveguides and their optical characteristics has been reported. Although a refractive index increase is observed in case of the proton implantation in diamond, the mechanism for this increase is unclear. This motivated us to study the effects of proton implanted diamond. Here, we attempt to understand the mechanism behind the increase of refractive index and also perform a detailed optical characterization of the proton implanted waveguides in diamond. This work is still ongoing however some preliminary results are presented here.

6.1.1 Implantation procedure

An optical grade, high purity single crystal type IIa CVD diamond substrate with dimensions $5\ mm \times 5\ mm \times 1\ mm$ was obtained from Gemesis Corporation [161]. Proton beam writing is used to form the waveguides in diamond, the fabrication

procedure is similar to the one discussed in Chapter 4. For the fabrication of 1 mm long waveguides, the diamond sample is mounted in such a way that the 1 $mm \times 5$ mm surface faces the ion beam. The focused proton beam is scanned magnetically over a width of 2 μm. The waveguide width at the end of ion range is 4 μm if the lateral straggling of protons in diamond is taken into account. For ion implantation, the electronic collisions in the material is negligible compared to nuclear collision that occur at the end of range. For 2 MeV protons a maximum damage at a depth of 27 μm from surface is created.

Diamond can be converted into graphite by ion implantation when the vacancy density is above $1\times10^{22}/cm^3$ for shallow implantation, and $6-9\times10^{22}$ vacancies$/cm^3$ for deep implantations [162, 163]. This corresponds to an areal fluence of the order of 1×10^{17} $ions/cm^2$. In order to fabricate waveguides by this process, the proton implantation has to be performed with a fluence below this critical value. In order to accurately calculate the proton fluence, the Rutherford backscattering spectrum is obtained using the RBS detector in the target chamber. From the obtained spectrum, the carbon surface peak is fit using the SIMNRA software package to obtain the incident number of protons. The measured RBS spectrum along with the SIMNRA surface peak fit can be seen in Figure 6.1. A total of 6 waveguides with a 2 μm width were fabricated using PBW uaing a proton fluence varying from 2×10^8 to 4×10^{10} $ions/cm$. Since line scanning is used for the waveguide fabrication, the proton fluence is quantified as line fluence. A line fluence is a more accurate measure compared to an areal fluence since the final dimension of the microstructure at the end of range always larger than the designed dimension [164]. The protons create the maximum damage to the crystal at the end of the ion range because of the nuclear collisions. The differential interference contrast microscope image of the cross section of the sample shows the damage profile. The top view and the cross-sectional microscope images were obtained and is shown in Figure 6.2. As can be observed from the figure, the electronic collisions have negligible effect on the refractive index because there is no significant change observed in the

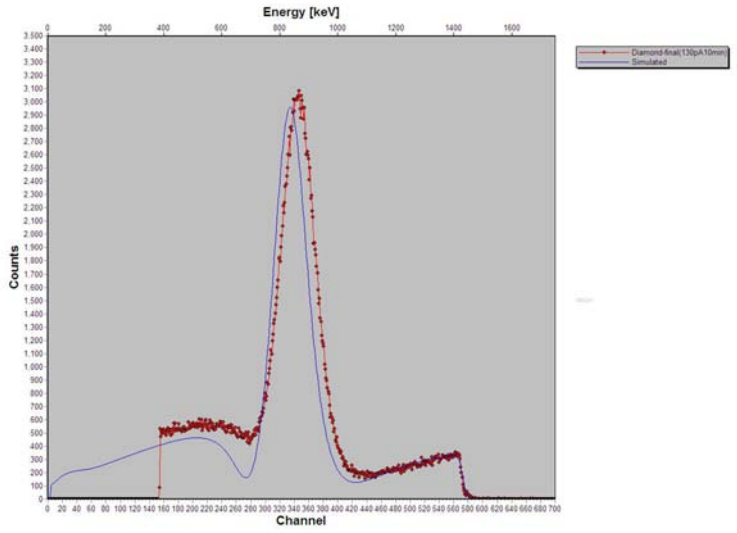

FIGURE 6.1: The figure shows the collected RBS spectrum along with the SIM-NRA fit

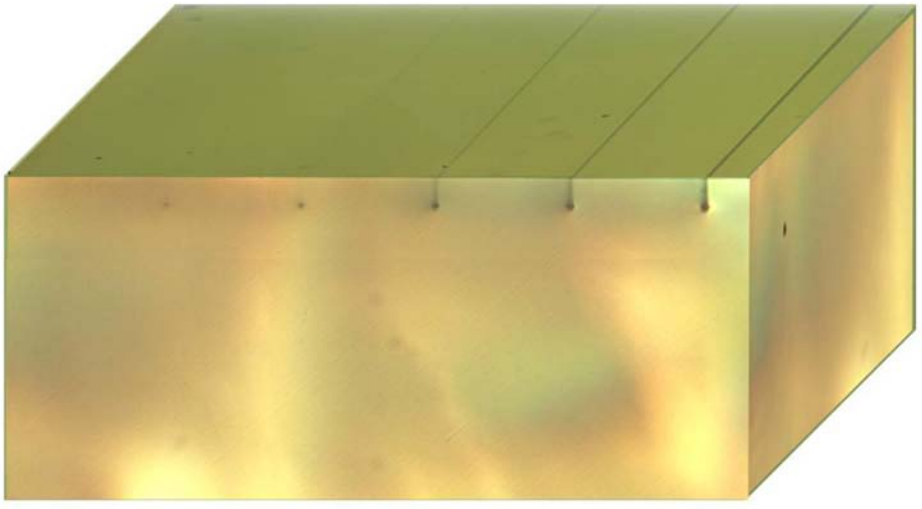

FIGURE 6.2: The top view and the cross-sectional DIC microscope images of the proton implanted waveguides of different ion fluence

region between the surface and the end of range. At the end of range, the damage is pronounced and can be easily observed from the cross-sectional optical micrograph obtained from the fabricated waveguides.

6.1.2 Optical waveguiding in proton implanted Diamond waveguides

The proton implanted 2 μm wide structures with different proton fluences are optically characterized using a continuous wave 532 nm diode pumped solid state laser using the end-fire coupling set up discussed in Chapter 4.

6.1.2.1 Evidence of waveguiding

The waveguides fabricated in diamond showed optical-guiding in implanted regions, where the proton beam has created the maximum damage. The waveguides of different proton fluence were end-fire coupled using the free-space optical waveguide characterization setup using a 532 nm continuous wave DPSS laser. For the coupling of light into the waveguides, a 10x microscope objective was used and for light collection from the output of the waveguides, a 40x objective lens was used. The output modes of the waveguides were captured with a CCD camera and is shown in Figure 6.3. Figure 6.3 shows the confined modes at the end of range at a depth of 27 μm from the diamond surface which clearly shows that the optical field is confined and that guiding occurs in the implanted waveguides. This indicates that optical modification has taken place due to the nuclear damage caused by the proton implantation. As can be observed from Figure 6.3, for higher fluence waveguides, the mode intensity is greatly reduced which is possibly due to the absorption of photons from the large defect concentration in this region.

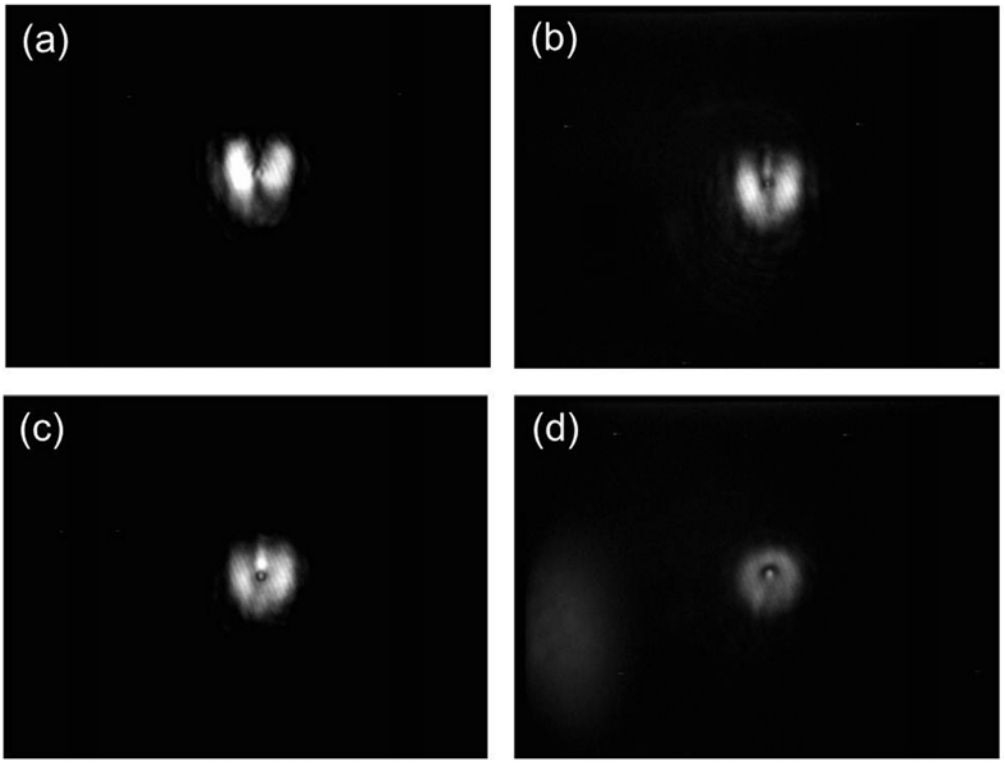

FIGURE 6.3: The output TM mode profiles of the proton implanted diamond waveguides with different proton fluence, (a) 4×10^{10} *protons/cm* (b) 2×10^{10} *protons/cm*, (c) 1×10^{10} *protons/cm*, (d) 2×10^{9} *protons/cm*.

6.1.2.2 Propagation loss measurements

The output mode profiles obtained are the direct evidence of wave-guiding in the proton implanted waveguides. The propagation loss measurement has been carried out to estimate the losses incurred due to proton implanation. The waveguide is only 1 *mm* in length which is very short and since it is hard to polish diamond, the cut-back method for propagation loss measurement cannot be implemented. So instead, we employ the scattering technique to calculate propagation loss in these waveguides.

The scattering technique is a simpler method to measure the propagation loss in the integrated waveguides. In this technique, the propagation loss can be measured by monitoring the out of plane scattered light intensity from the light propagating in the waveguides. The intensity of light propagating in the waveguide is proportional

to the intensity of the light scattered out of the waveguide. The intensity variation as a function of the length of the waveguide can be written as

$$I(x) = I_0 10^{-(\frac{\alpha x}{10})} \tag{6.1}$$

where $I(x)$ and I_0 are the transmitted light intensity after a propagation distance of x and the initial intensity at the start of the waveguide respectively. The x(cm) is the propagation distance in the waveguide and α is the loss coefficient. The attenuation factor α can be calculated by fitting the plot of intensity vs length measured from the waveguide using equation 6.1. Equation 6.1 can be rewritten in terms of $\alpha(dB/cm)$ as

$$\alpha = -\frac{10}{x} log\big(\frac{I(x)}{I_0}\big) \tag{6.2}$$

The waveguides are end-fire coupled using the optical setup discussed in Chapter 4. Since the length of the waveguide is short and the material is transparent, it is hard to identify the coupling of light into the waveguide. To ensure that the focus of the input objective lens is at the input end facet of sample, the other end of the sample is focused using the output objective lens by observing the cross-sectional image of the sample with the aid of a vidicon camera. Then, the diamond sample is moved down and the input objective lens is translated to obtain a focused laser spot in the vidicon camera without moving the output objective. Now, the diamond sample is moved back into position and the input objective is moved in the opposite direction with a distance equal to the length of the waveguide, in which case the focus plane has to be at the input end facet of the sample. The incident light is coupled into the waveguide and the scattered light images from the light propagating in the waveguides is captured using the high resolution visible camera from QImaging (QIMAGING Retiga Exi). In order to calculate the propagation loss, the waveguide region in the image is cropped and the logarithm of intensity is plotted as a function of the propagation length. A total of 10 images are captured for each waveguide and

Fluence ($protons/cm$)	Propagation loss (dB/cm)	
	TE	TM
4×10^{10}	124.93	105.32
2×10^{10}	83.33	71.27
1×10^{10}	34.85	37.21
2×10^{9}	46.08	44.21

TABLE 6.1: Summary of the propagation loss results on different proton fluence buried waveguides

are averaged in order to improve the accuracy of measurement. The background is subtracted from each image and the waveguide section of the image is cropped and processed to obtain the propagation loss. A MATLAB code (Appendix C) is written and implemented to make the data processing simpler.

For each waveguide fluence, a set of scattered images are collected and processed to obtain the propagation loss of the waveguide. The top view scattered image and the corresponding linear fit used to calculate the propagation loss is shown in Figure 6.4.

The measurement of the optical modes and the propagation loss has been carried out for both TE and TM polarizations and the results are tabulated in Table 6.1. The propagation loss is slightly lower for TM polarized light compared to TE polarized light. The propagation loss shows a decreasing trend as the proton fluence decreases from 4×10^{10} $protons/cm$ to 1×10^{10} $protons/cm$. And below a fluence of 1×10^{10} $protons/cm$ the propagation loss shows an increasing trend for both polarizations. This shows that in the case of the as-implanted waveguides, the 2×10^{10} $protons/cm$ fluence waveguide has a lower propagation loss when compared to waveguides fabricated using higher fluences. The higher propagation losses that were measured for waveguides above this fluence may be because of the increase in absorption. For the lower fuences, the reduced refractive index contrast decreases the confinement of the optical field, resulting in a higher propagation loss. Although the propagation losses tabulated are quite high, these propagation losses can be reduced by thermally annealing the damage caused during implantation.

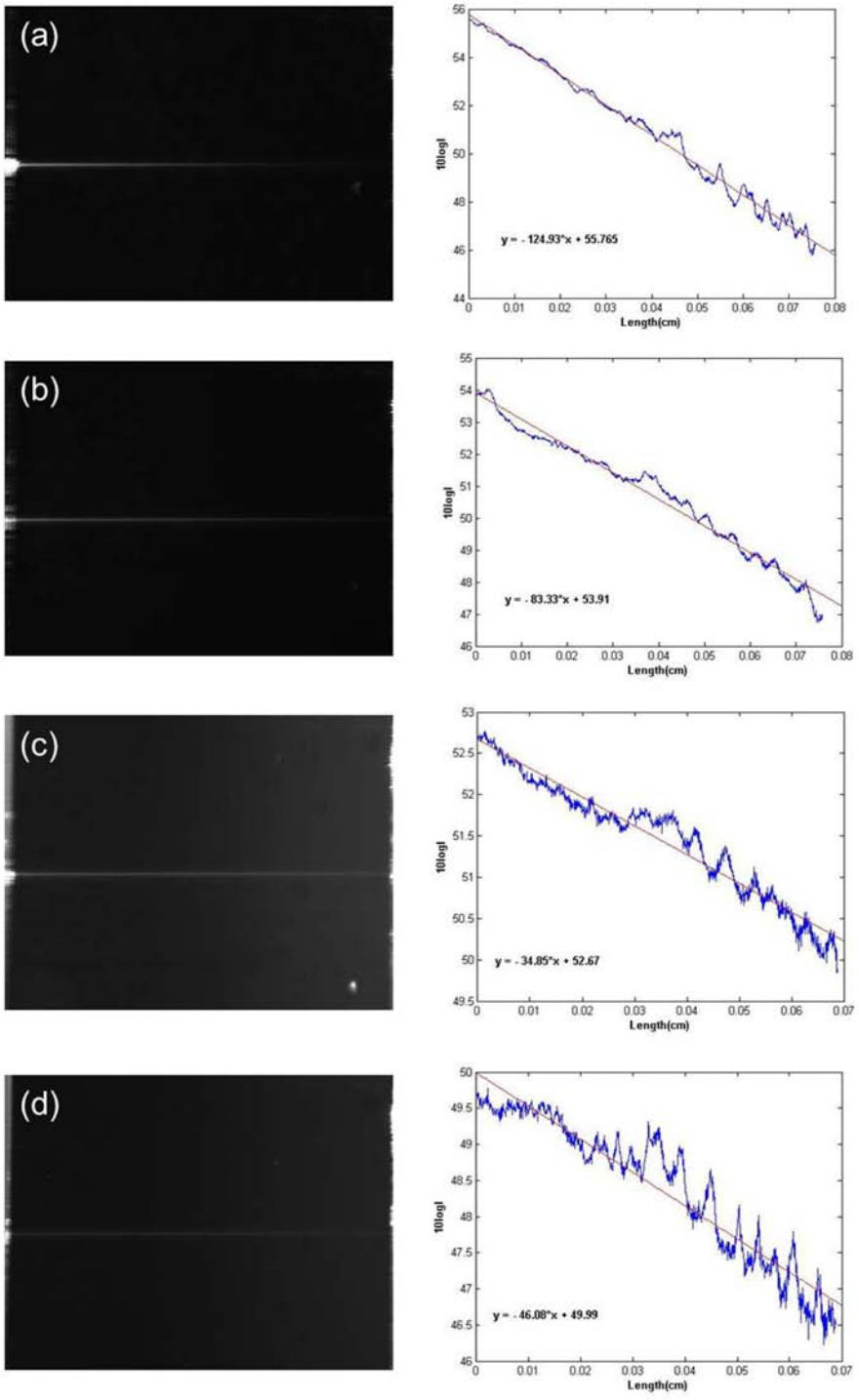

FIGURE 6.4: The scattered light images collected from the top view camera and the corresponding intensity plot as a function of the length of the waveugide for different proton fluence waveguide (a) 4×10^{10} *protons/cm* (b) 2×10^{10} *protons/cm*, (c) 1×10^{10} *protons/cm*, (d) 2×10^{9} *protons/cm*.

6.1.3 Spectroscopic investigation of implantation effects

The proton implanted diamond is spectroscopically investigated to get the information on the optical effects produced by the implantation process. The room temperature photoluminescence, Raman spectroscopy and the atomic force microscopy were performed in an attempt to better understand the ion beam damage process.

6.1.3.1 Photoluminescence of implanted diamond

Different defects formed during the implantation sometimes result in different fluorescence emission centres that can be used to identify the defects formed during the proton implantation process. The cross section of the implanted waveguide in the diamond sample is used to measure the micro photoluminescence spectra using a home built micro PL set-up based on microscope and a 405 nm diode laser. A fluorescence microscope is used to observe the fluorescence from the proton implanted waveguides. The fluorescence image is captured when the sample is excited using blue excitation filter and is shown in Figure 6.5. As can be seen from the Figure 6.5, all the waveguides are emitting fluorescence including the lowest fluence waveguides where light propagation was not observed. The photoluminescence spectrum is collected from the various waveguides at room temperature through a fibre-coupled spectrometer (shown in Figure 6.6). It is clear from the figure that the proton implantation process creates two different color centres in diamond, one with a zero phonon line (ZPL) at 470 nm corresponding to the TR12 color centre and the other ZPL at 740 nm corresponding to the GR1 color centre. The TR12 color centre is due to an interstitial carbon atom in a hexagonal site [165]. The GR1 color centre is the commonly observed in diamond after ion implantation [166]. This color centre is formed because of point defects created as a result of ion implantation, and the fluorescence intensity increases with ion fluence because of the increased creation of point defects in the crystal. The ZPL for both the color centres can be observed at

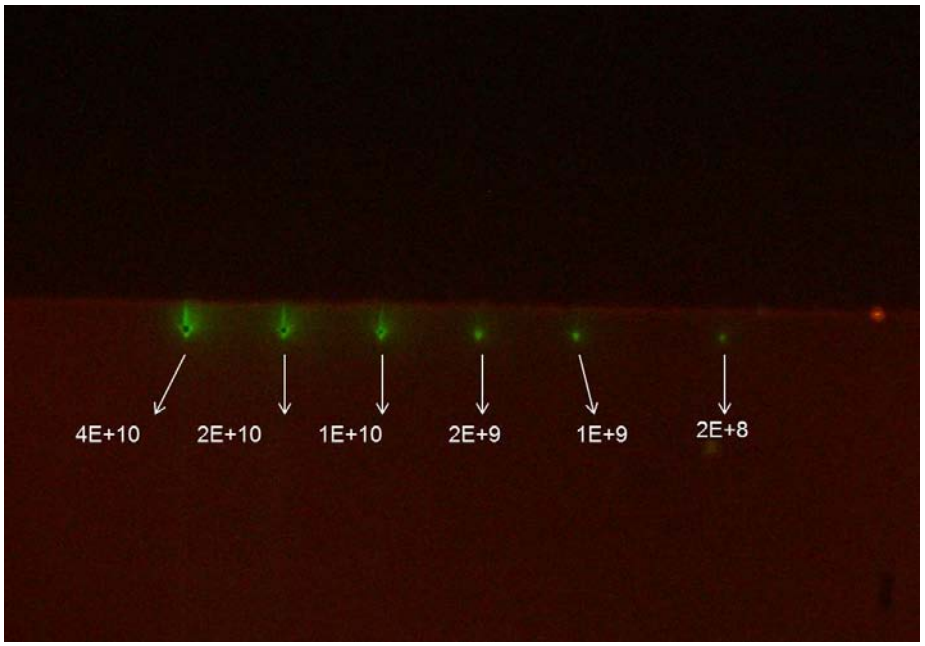

FIGURE 6.5: The figure shows fluorescence image of the cross-sectional view of the implanted waveguide

room temperature which suggests that the color centre emission is strong and can be used as a room temperature single photon light source.

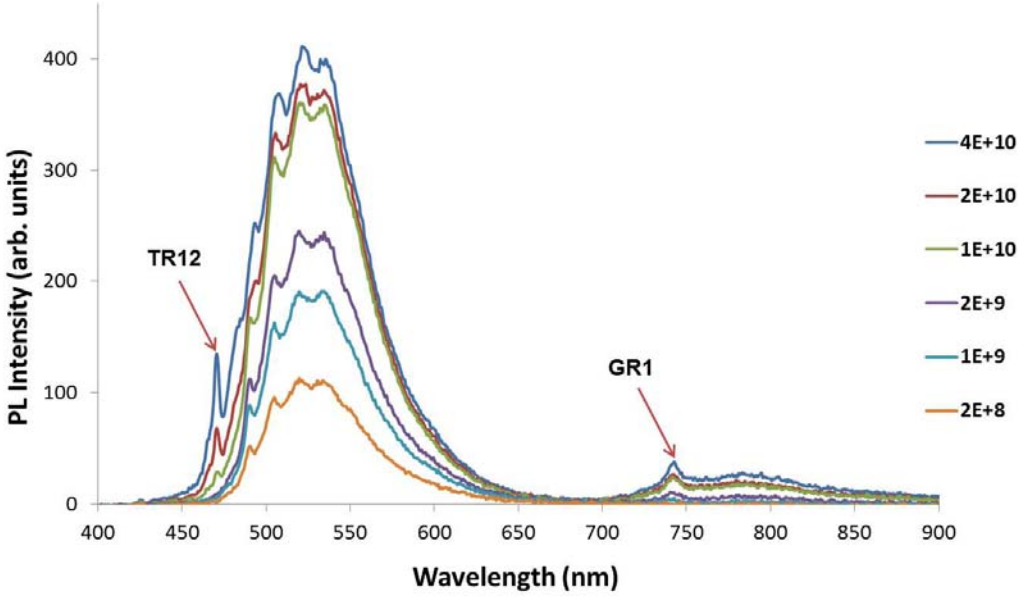

FIGURE 6.6: The figure shows room temperature photoluminescence spectrum obtained from the proton implanted diamond showing two different color centres

6.1.3.2 Atomic force microscopy results

Atomic force microscopy was performed on the implanted diamond to observe any swelling on the surface because of the pressure buildup inside the diamond crystal caused by the proton implantation. First, the pristine diamond surface is imaged using AFM to obtain the surface roughness, the image is shown in Figure 6.7. The rms roughness of the diamond surface is 1.5 nm. Then, AFM is performed on

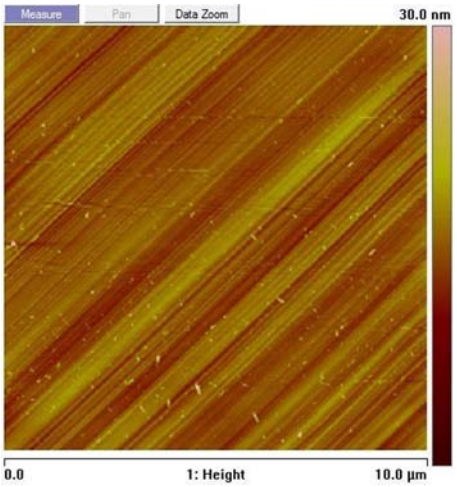

FIGURE 6.7: The figure shows atomic force microscopy image representing the pristine diamond surface roughness less than 1.5nm

the proton implanted waveguides, no surface swelling is observed for fluences below $1{\times}10^{10}$ $protons/cm$. The AFM image showing the surface swelling of 5.2 $\pm$ 0.5 nm for $2{\times}10^{10}$ $protons/cm$ fluence waveguide, is shown in Figure 6.8. The AFM measurements on the waveguide region of the 5 mm $\times$ 5 mm surface of the sample also shows no swelling.

6.1.3.3 Raman spectral mapping of proton implanted diamond waveguides

Raman spectroscopy is a powerful tool that can be used to monitor structural changes in the material. The Raman spectroscopy on the implanted diamond was

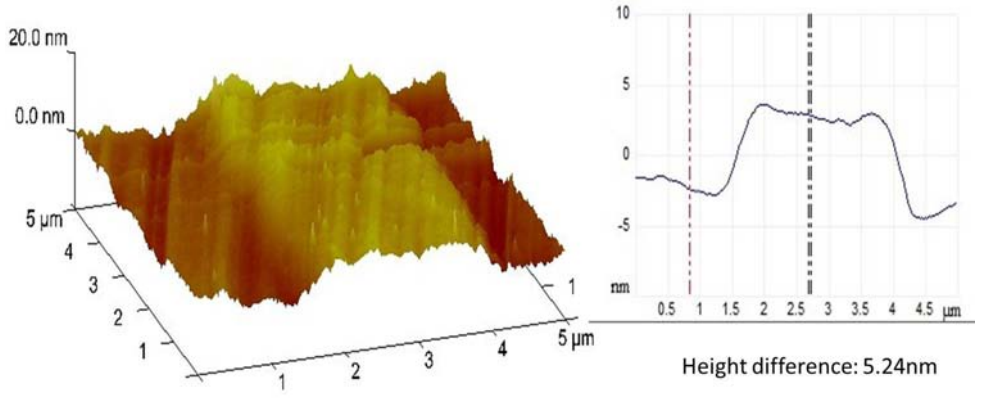

FIGURE 6.8: Atomic force microscopy image showing height difference between the waveguide region and the pristine diamond region which corresponds the surface swelling caused by the proton implantation.

performed at different points on the implanted regions to obtain the information on lattice vibrations. The Raman spectrum from the pristine diamond, shown in Figure 6.9, shows a Raman peak for CVD diamond with wave number 1332.5 cm^{-1} and the second order peaks observed at higher wave numbers. The Raman spectrum is obtained at different points within the ion beam damage region in the diamond using a micro Raman spectrometer. The micro Raman spectrometer is able to obtain the Raman spectrum within the spatial resolution of less than 1 μm on the sample and from each Raman spectrum, the Raman intensity can be mapped in different intervals of wavenumbers selected. The Raman spectrum at different points at the end of range and the corresponding Raman peak mapping can be found in Figure 6.10.

From the obtained Raman spectrum, it is evident that the proton fluence used in the experiment have not exceeded the graphitization limit since there is no graphite peak near 1560 cm^{-1} observed in the spectra collected at different points. The Raman spectra at different points within the maximum damage region showed Raman peaks at different wave numbers. The Raman spectrum obtained from point 4 in Figure 6.10 shows several interesting peaks at wave numbers 300, 680, 1630 and 3030 cm^{-1}. It is observed that these peaks appear just below where the maximum damage

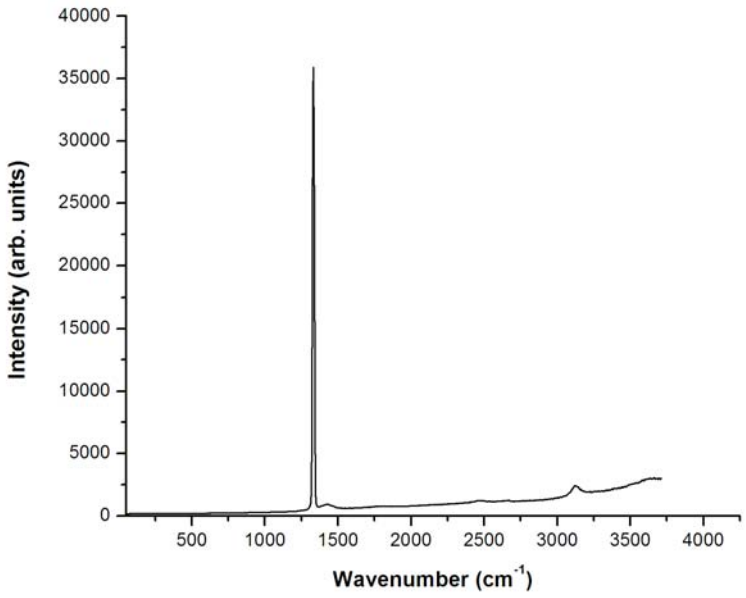

FIGURE 6.9: The Raman spectrum of the pristine CVD grown sample obtained away from the waveguide region

occurred during the implantation. This may be attributed to the fact that the internal pressure causes the lattice vibrations to change in a region just below where the maximum damage occurs. Because of the internal pressure, the lattice is deformed and in the region above where the maximum damage occurs, the diamond lattice expands and the surface swelling takes place. In the region below where the maximum damage occurs, diamond lattice experiences pressure.

6.1.3.4 Refractive index modification

The refractive index modification can be estimated from the vacancy density. The SRIM monte carlo simulations are used to obtain information on the vacancies creation during ion implantation. The implantation creates a vacancy density (ν(z)) at a depth z which can be calculated from the vacancy per unit length ($p^{(E)}(z)$) and the ion fluence(ϕ).

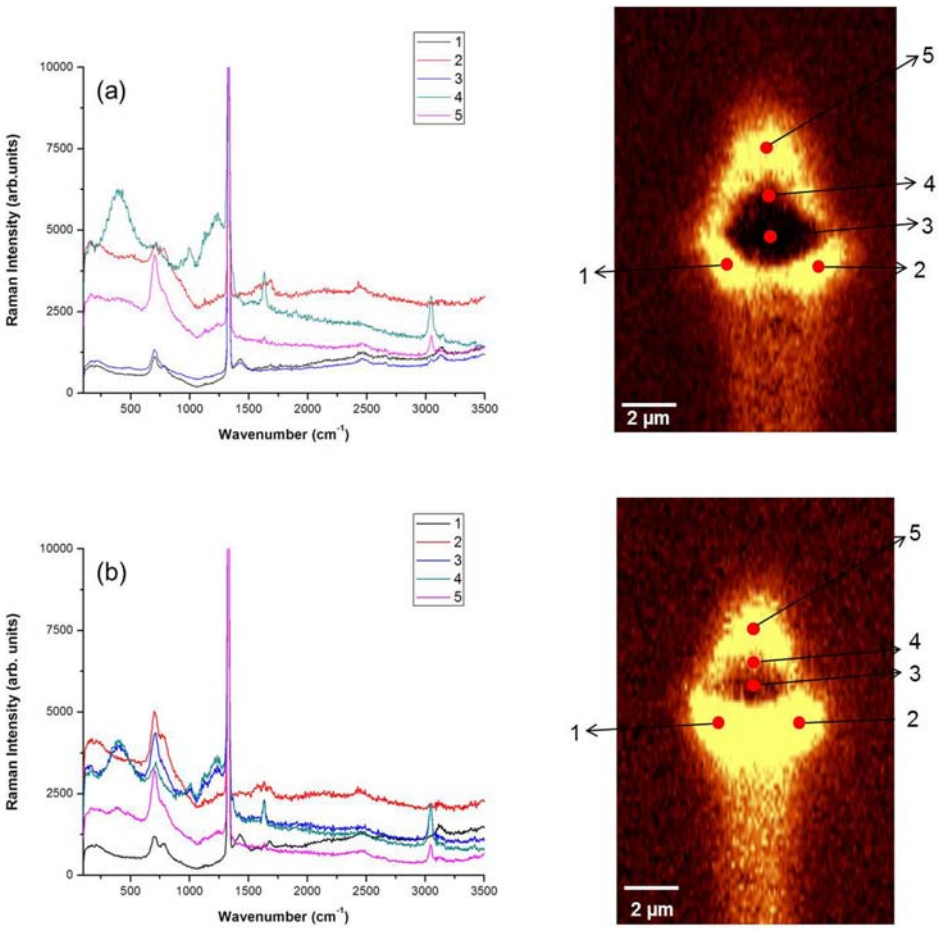

FIGURE 6.10: Raman spectra obtained at different points (located in Raman map) within the damage region and the corresponding Raman intensity map image for (a) $4{\times}10^{10}$ *protons/cm* fluence waveguide and (b) $2{\times}10^{10}$ *protons/cm* fluence waveguide

The vacancy density is given by

$$\nu = \phi.p^{(E)}(z) \tag{6.3}$$

is we assume that nonlinear processes such as self-annealing, ballistic annealing and defect interaction are not taken into consideration. The complex refractive index retrieval method is discussed in Ref [167]. The complex refractive index is extracted from the optical path difference and the absorption length difference created by the implantation. The optical path difference and absorption length difference are function of proton energy and fluence. The complex refractive index can be written

Proton Energy	Re(c) (cm^3)	Im(c) (cm^3)
2 MeV	$(4.34\pm0.05)10^{-23}$	$(2.86\pm0.05)10^{-23}$
3 MeV	$(4.26\pm0.12)10^{-23}$	$(2.85\pm0.10)10^{-23}$

TABLE 6.2: Values of the complex quantity c for two different proton energies

as

$$\hat{n}(z) = \hat{n_0} + \hat{c}.\nu(z) \tag{6.4}$$

The complex quantity $\hat{c}$ is estimated from the complex optical path difference. The real and imaginary amplitudes of c are tabulated for two different energies taken from the Ref [167]. The vacancy density (ν(z)) is calculated from the SRIM monte carlo simulations performed on diamond using an atomic density of 3.52 g/cm^3 and a displacement energy of 50 eV for an averaged ensemble of 50,000 *ions*. From the complex quantity c and the vacancy density (ν(z)), the refractive index is estimated for each proton fluence and is shown in Figure 6.11. A maximum increase in refractive index of 0.0267 is obtained for 4×10^{10} $protons/cm$ fluence using this method.

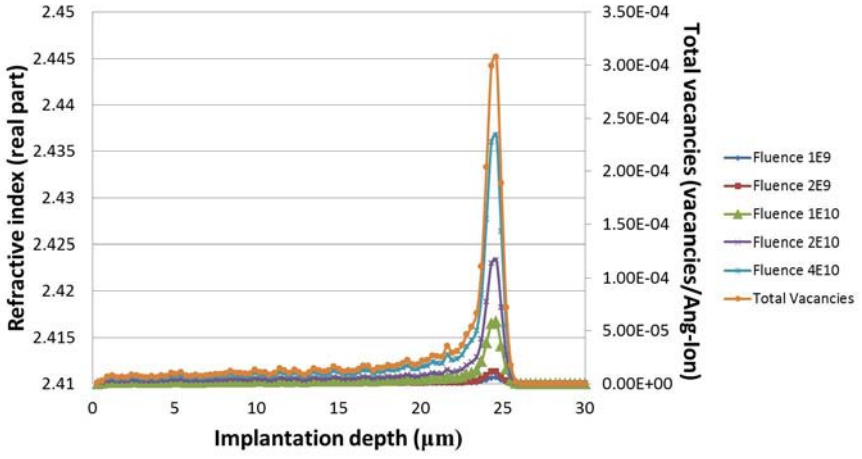

FIGURE 6.11: The figure shows the vacancy density and the corresponding refractive index profile as a function of depth in the implanted diamond for each proton fluence

6.1.4 Thermal annealing study of proton implanted diamond waveguides

Thermal annealing can be used to alleviate damage created by the ion implantation [168]. The effect on propagation loss of diamond waveguides for different annealing temperatures has been studied. To perform this experiment a different sample is used. A type IIa single crystal cvd grown diamond sample of dimensions 3.0 × 3.0 × 0.5 mm^3 is used for the proton implantation. The sample was then implanted at the external scanning microbeam facility of the LABEC laboratory in Firenze [169]. The waveguides are fabricated with a waveguide width of 12 μm and a length 500 μm with fluence 1.2×10^{10} $protons/cm$ and 2.4×10^{10} $protons/cm$. The first evidence of light guiding in proton implanted diamond was observed in the same sample with a different proton fluence reported in [160]. The as-implanted diamond sample is optically characterized using the optical characterization set-up discussed in Chapter 4. The scattering method is used for the propagation loss measurement. After the measurement the sample is thermally annealed at different temperatures in ambient atmosphere. After each thermal annealing step the propagation loss measurements has been carried out. The annealing temperature dependent propagation loss measurements for both TE and TM polarisations are tabulated in Table 6.3 and the plot showing the propagation loss as a function of annealing temperature is shown in Figure 6.12. After annealing at 400 °C the 1.2×10^{10} fluence waveguide propagation loss is reduced to 20.4 dB/cm from 153.1 dB/cm for TE polarization. The annealing study is in progress and annealing at increased temperatures may further reduce the propagation losses.

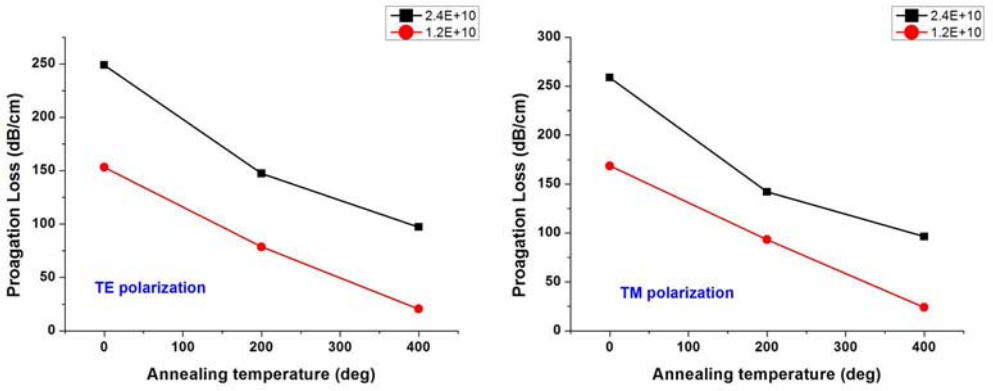

FIGURE 6.12: The figure shows the propagation loss of the diamond waveguides as the annealing temperature increases under different incident polarization of light (a) TE polarization (b) TM polarization

Waveguide fluence ($particles/cm$)	Annealing temperature	Propagation loss (dB/cm)	
		TE	TM
2.4×10^{10}	as-implanted	248.9	258.7
	200 °C	147.3	141.9
	400 °C	97.2	96.3
1.2×10^{10}	as-implanted	153.1	168.6
	200 °C	78.7	93.2
	400 °C	20.4	24

TABLE 6.3: Summary of results of diamond waveguide propagation loss depending on annealing temperatures

6.2 Optical modification in nonlinear optical crystals through ion beam writing

Nonlinear optical crystals have been extensively studied due to their unique optical properties. They have been utilized in various applications including frequency converters for lasers, electro-optic modulators etc. By creating microstructures and optical waveguides in non linear optical crystals, many of the unique phenomena that are observed in bulk crystals can be utilized for applications in integrated optics. Furthermore, due to the increased level of optical confinement in microstructures, many of these nonlinear effected can be enhanced [170]. For example, nonlinear

waveguides are expected to allow the occurrence of diverse nonlinear phenomena at very low light powers [171]. Particularly, for crystals that serve as frequency converters, waveguide-based light generation could have a higher efficiency and give more choice of different modes when compared to their bulk counterparts [172]. Recent work utilizing ion implantation to modify non linear crystals has shown that an increase in refractive index can be achieved at the end of range. This makes it possible to directly fabricate waveguides in these materials. Two dimensional waveguide configurations such as channel waveguides, ridge waveguides can further confine the optical fields to obtain increased optical densities.

Recently high energy proton beam writing with energies typically 1-3 MeV, has emerged as a promising lithographic technique with beam spot sizes as small as 19 nm $\times$ 29.9 nm. Focused proton beam writing has already been successful in fabricating buried channel waveguides in glasses, semiconductors, and laser crystals. More recently, channel waveguides in Nd:YAG fabricated using PBW have shown low loss waveguiding. In addition, these waveguides were used as continuous wave lasers with highly symmetric modes [168, 173]. Helium (He) ions can also be focused to fabricate buried waveguides in laser crystals. In this section, buried optical waveguide fabrication using both proton beam writing (PBW) and focused He beam writing (HeBW) are discussed along with the characterization results.

6.2.1 Implantation procedure

Nonlinear optical crystals Neodymium doped gadolinium gallium garnet (Nd^{3+}:$Gd_3Ga_5O_{12}$ or Nd:GGG) and Potassium titanyl phosphate ($KTiOPO_4$ or KTP) are chosen as the substrate material for waveguide fabrication using PBW and HeBW respectively.

Neodymium doped gadolinium gallium garnet (Nd^{3+}:$Gd_3Ga_5O_{12}$ or Nd:GGG) is one of the excellent gain media for solid state lasers, and has attracted much attention owing to its advantageous features such as good thermal conductivities, higher

separation coefficient of Nd^{3+} and fewer growth defects. Because of its stable chemical properties, normal chemical methods such as metal ion thermal in-diffusion and ion exchange cannot be applied to fabricate waveguides in Nd:GGG. So far, channel waveguides have been fabricated in an Nd:GGG crystal only by physical techniques, such as masked ion implantation and femto-second (fs) laser inscription.These techniques were also utilized to fabricate waveguide lasers [174, 175].

Potassium titanyl phosphate ($KTiOPO_4$ or KTP) is a well known nonlinear optical crystal, that has been used for applications such as optical parametric oscillation (OPO), and second harmonic generation (SHG). These applications have come about due to its many superior properties, e.g., broad transmitting range, large nonlinear optical coefficients, and high optical damage threshold [176–178]. Channel waveguides in KTP crystals have been produced by several techniques including ion exchange [179], ion implantation [180, 181], and femtosecond laser inscription [182].

The waveguide fabrication procedure used in this thesis is same for both crystals, Nd:GGG and KTP apart from different energies and the ion fluence used. For the fabrication of optical waveguides in laser crystals, first, the ion beam is focused using the magnetic quadrupole lens to the beam spot size of 500 nm and the beam is magnetically scanned, over a lateral width which is the width of the waveguide, perpendicular to the direction in which the the motorized stage translated. The fabrication procedure is depicted in Figure 6.13

An optically polished Nd:GGG crystal with dimensions of 10 mm × 5 mm × 1.5 mm is used for the experiments. Waveguides are fabricated using 1 MeV protons on the 10 mm × 5 mm surface with the 10 mm direction as the beam scanning direction and the 5 mm direction as the writing direction. The proton implanted waveguide of 4 μm width is fabricated in Nd:GGG with proton fluence of $2{\times}10^{16}$ $ions/cm^2$.

An optically polished KTP crystal with dimensions of 11 mm × 7 mm × 1.2 mm is

used in this study. The 11 $mm \times 7$ mm surface is used for the fabrication of waveguides. The 2 MeV He^+ ion beam is used to fabricate waveguides of 4 μm width in the 11 mm direction with beam scanning direction set to the 7 mm direction. Two waveguides are fabricated with fluence of $5{\times}10^{15}$ and $1{\times}10^{16}$ $ions/cm^2$.

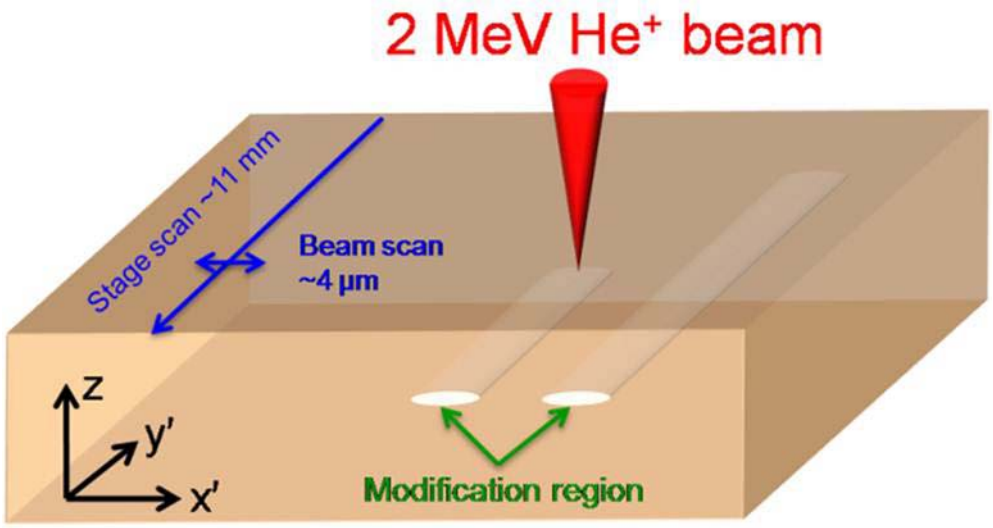

FIGURE 6.13: Schematic represents the waveguide fabrication procedure

6.2.2 Effects of implantation

The SRIM monte carlo simulations are performed to obtain the ion-induced damage profile in the nonlinear crystals. As mentioned earlier the damage is created at the end of the ion range, where the ions lose most of their energy and contribute to nuclear collisions. The SRIM simulation shows that the Bragg peak occurs at a depth of 8.6 μm in the material in the case of the proton implantation in Nd:GGG and 5.5 μm deep in the case of the He^+ implantation in KTP. As can be seen from Figure 6.14, the damage is negligible before the end of range and increases suddenly at the end of range which causes a variation in the nonlinear properties in the confined region where the nuclear collisions are dominant. The figure shows both the defect per atom (DPA) and the ion concentration in the material. The

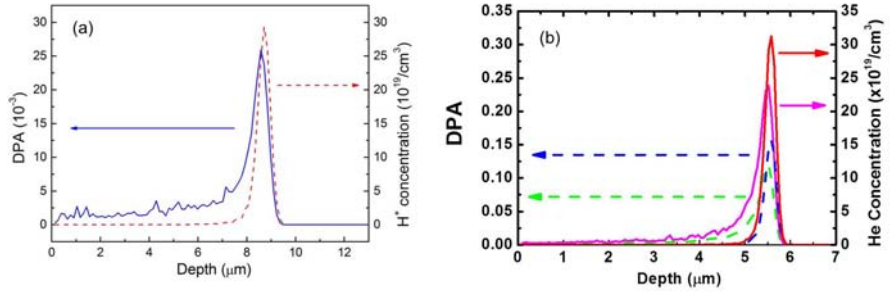

FIGURE 6.14: SRIM simulation results showing the defect per atom (dashed line) and the Ion concentration in (a) Nd:GGG and (b) KTP nonlinear crystal

cross sectional images of the fabricated waveguides are shown in Figure 6.15. The 6.15(a) shows an optical image of the cross section of the fabricated waveguide in Nd:GGG that was fabricated using a fluence of 2×10^{16} $ions/cm^2$. The cross section image shows that the waveguide is formed at a depth of 8.6 μm which agrees well with the simulation result. The Figure 6.15(b) shows the cross sectional optical transmission image of the waveguide fabricated using a fluence of 1×10^{16} He^+/cm^2. The waveguide is formed at a depth of 5.5 μm from the surface of the KTP crystal which also agrees with the simulation result.

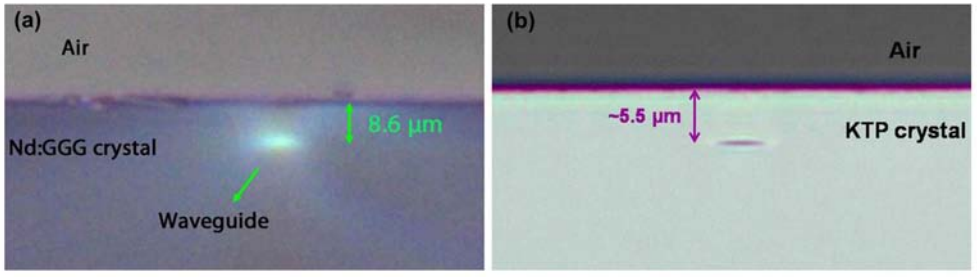

FIGURE 6.15: The cross sectional optical micrographs (a) for the waveguide fabricated in Nd:GGG and (b)the optical transmission image of the KTP waveguide.

6.2.3 Results and Discussion

The fabricated waveguides in the laser crystals are optically characterized with the end-fire coupling set-up that uses 632.8 nm wavelength HeNe laser. It is found that

all the waveguides show guiding at the local modification which further confirms that the effect is caused by the nuclear damage in the crystals. From the measured modal profile the refractive change can be retrieved.

6.2.3.1 Refractive index retrieval

The refractive index changes caused by the ion implantation in the crystals are estimated by measuring the numerical aperture (N.A) of the channel waveguides [183], and through equation 6.5

$$\Delta n = \frac{sin^2(\Theta_m)}{2n} \tag{6.5}$$

where n is the refractive index of the bulk crystal, and Θ_m is the maximum incident angular deflection at which no guiding of light occurs inside the waveguide.

The refractive index of the bulk substrates are measured using the m-line technique through a prism coupler (Metricon 2010). The measured refractive index of the Nd:GGG substrate is 1.965. Using the same technique the measured refractive indices of the KTP substrate are 1.7630 for $n_{x'}$ and 1.8643 for n_z.

In case of the Nd:GGG waveguide, the maximum increase in refractive index is estimated as 1.2×10^{-3}. Based on this measurement, the refractive index profile is reconstructed through the mode profile. The refractive index distribution is used to simulate the light propagation in the waveguide with the finite-difference beam propagation method by using the commercial software RSoft BeamPROP. The obtained guided mode TM_{00} through simulation along with the measured modal profile and the reconstructed refractive index distribution can be seen in Figure 6.16. As can be observed from Figure 6.16(a) and Figure 6.16(b) the calculated mode profile and the simulated mode profile are in agreement which suggests that the refractive index reconstruction is successful. The propagation loss is also calculated using the same setup using the Fabry-Perot method. The measured propagation

loss was 4.3 dB/cm for TM_{00} mode at the same wavelength.

A similar approach is implemented for the buried waveguide fabricated in KTP

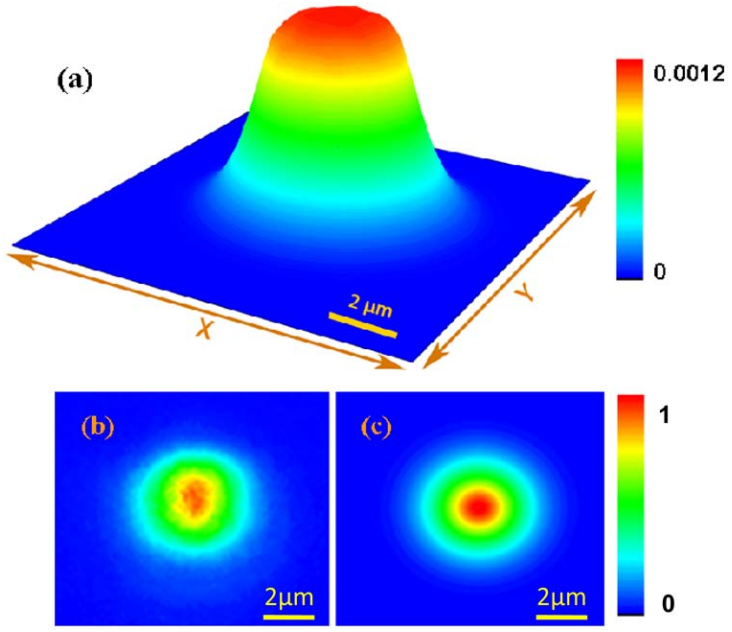

FIGURE 6.16: (a) Reconstructed refractive index change distribution of the Nd:GGG channel waveguide at 633 *nm*, with the index of the substrate to be 1.965; (b) measured and (c) calculated modal profile of the TM_{00} fundamental mode of the waveguide.

with a fluence of 5×10^{15} He^{+}/cm^{2}. The maximum estimated refractive index change for quasi TE_{00} mode was calculated to be 4.2×10^{-3}. Using this maximum index change, the refractive index distribution is reconstructed with which a simulation is carried out to obtain the calculated quasi TE_{00} mode profile. The refractive index distribution, calculated and simulated quasi TE_{00} mode profile is shown in Figure 6.17. It can be observed that the calculated and the simulated mode profiles are in agreement.

The propagation losses of the two channel waveguides are calculated using the same set-up using a wavelength of 632.8 nm. The results are tabulated in Table 6.4. The table shows that the propagation loss for both the modes TE and TM along with the estimated maximum refractive index. For the low fluence (5×10^{15} $particles/cm^{2}$) waveguide, the TE guided modes showed lower propagation loss when compared to the TM guided modes. In contrast, the high fluence (1×10^{16} $particles/cm^{2}$)

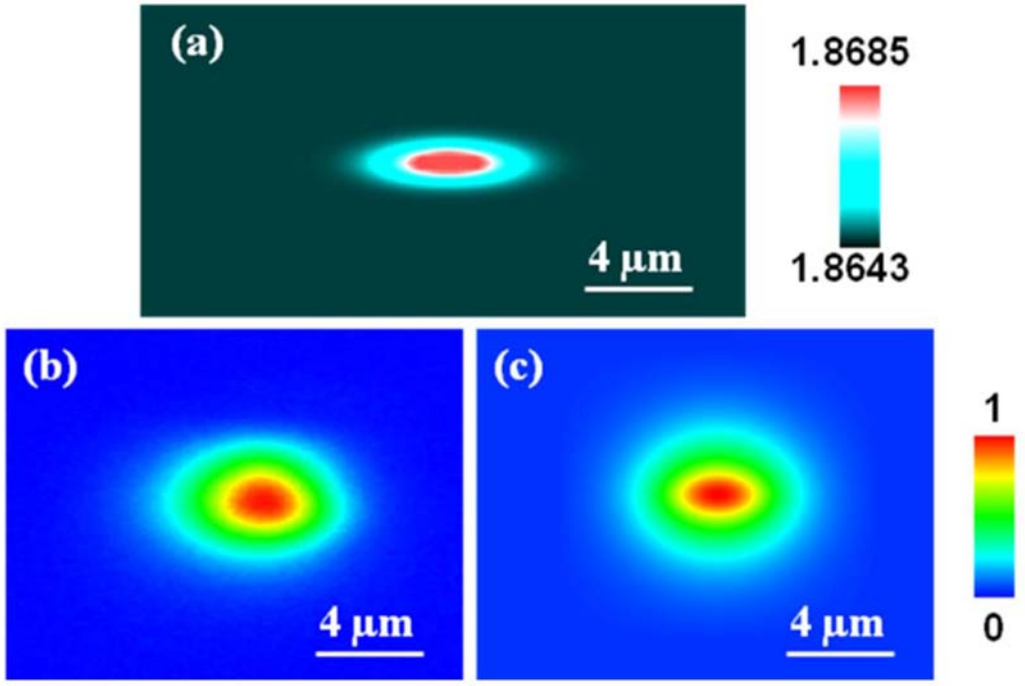

FIGURE 6.17: (a) Reconstructed refractive index distribution, (b) measured and (c) calculated modal profiles of the quasi-TE_{00} mode of the buried channel waveguide with fluence of 5×10^{15} $particles/cm^2$at the wavelength of 632.8 nm.

Fluence (particles/cm^2)	Propagation loss (dB/cm)		Refractive index change	
	TE	TM	Δ $n_{x'}$	Δ n_z
5×10^{15}	0.7	1.8	0.00420	0.00430
10×10^{15}	6	2.8	0.00270	0.00277

TABLE 6.4: Summary of results on KTP buried waveguides

waveguide showed a lower propagation loss for the TM guided mode. Basically, the propagation loss in the waveguides depends on refractive index contrast between the waveguide and the surrounding bulk crystal, and the defect level of the lattices (related to the scattering loss). The waveguide fabricated by HeBW using a fluence of 5×10^{16} He^+/cm^2 gives the optimum refractive index change and lattice disorder that resulted in lowest propagation loss of 0.7 dB/cm.

The propagation loss in both the crystals can be further reduced by an extra annealing step, which has already been demonstrated in case of Nd:YAG channel waveguides fabricated using PBW.

6.2.3.2 Waveguide laser based on Nd:GGG waveguide

Proton implanted Nd:GGG buried waveguides were able to operate as waveguide laser. To characterize the waveguide laser the Nd:GGG sample is adhered to a mirror at each end of the sample to form the resonant cavity. The Fabry-Perot cavity is formed with two mirrors designed to give a 98% transmission at 808 *nm* and >99% reflectivity at 1064 *nm* (input mirror) and a mirror with reflectivity >99% at 808nm and >95% reflectivity at 1064 *nm* (output mirror). The end-fire coupling set-up designed to characterize the laser had a convex lens of focal length 25 *cm* as the coupling lens, and a 20x microscopic objective lens along with the infrared CCD camera chosen for collecting the laser emission. The laser emission was characterized using a spectrometer and the laser emission spectrum along with the plot of output CW waveguide laser power as a function of absorbed power in the channel waveguide can be observed in Figure 6.18.

From the laser emission spectrum it is clear that the laser emission center is located

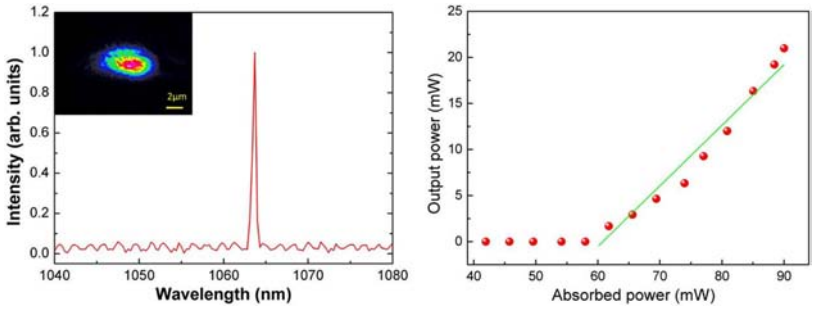

FIGURE 6.18: (a)Emission spectrum of the PBW Nd:GGG waveguide laser. Inset, image of the output laser mode (TM_{00})(b)Measured output waveguide laser power as a function of the absorbed pump power (balls). The green solid line shows the linear fit of the experimental data.

at 1063.7 *nm* which corresponds to the ${}^4F_{3/2} \rightarrow {}^4I_{11/2}$ transition of the Nd^{3+} ions. The FWHM of the emission line is calculated to be 0.6 *nm*. From the Figure 6.18(b) the pump threshold can be easily observed which is 61 *mW* and the slope efficiency can be calculated from the graph. A slope efficiency of 66% was achieved which is the highest value achieved in ion beam fabricated channel waveguides in laser

crystals. The optical-to-optical power conversion efficiency of 23% is achieved with maximum laser power measured to be 21 mW for the pump power of 91 mW. The PBW channel waveguide in Nd:GGG operated as a waveguide laser which had the highest slope efficiency and highest power conversion efficiency of any previously reported waveguide lasers fabricated using femtosecond laser.

Chapter 7

Summary and Outlook

7.1 Summary

Proton beam writing has been utilized for the fabrication of the smooth sidewall whispering gallery mode (WGM) microresonators in SU-8 polymer. The WGM microdisk resonator was integrated with waveguide to make the optical characterization simpler. The microdisk resonator was optically characterized at the telecommunication wavelengths and the whispering gallery mode resonator parameters were deduced from the experimental transmission spectrum. The highest quality factor achieved was 10^4 in polymer microdisk resonators. This waveguide integrated microdisk resonator has potential for wavelength filtering applications which was demonstrated successfully. To make active devices, the high Q-factor microdisk resonators were fabricated in a laser dye-doped polymer. These microresonators exhibited lasing action under optical pumping. The microdisk resonators were fabricated in 1% Rhodamine B doped SU-8 polymer and also in 1% Rhodamine 6G per chlorate doped SU-8 to obtain WGM resonator based microlasers. Optical pumping of the fabricated microlasers with frequency doubled Nd:YAG laser at 532 nm generating 7 ns pump pulses at 10 Hz repetition rate resulted in lasing near 600 nm for the two different dye-doped polymer microlasers. The microlaser threshold

pump fluence was calculated and it was found that the threshold for these cavities are smaller compared to the other cavity types because of the high Q-factors. The laser dye incorporated SU-8 material can therefore, be used as a potential active medium for making compact microlasers.

Although the microdisk resonators fabricated in dye doped SU-8 showed lasing, the microlasers were omni-directional because of the inherent circular symmetry. The omni-directional laser has no importance in practical applications. To make the microlaser directional, the circular design was deformed in different ways and fabricated in 1% Rhodamine B doped SU-8 polymer. The directionality of these microlasers was investigated qualitatively by obtaining cross-sectional images during optical pumping. The deformed laser cavities showed higher laser thresholds compared to circular disk lasers because of reduced Q-factor due to deformity. The microlaser performance was investigated by varying the parameters like laser design, dimensions of the microlaser and laser thickness. To improve the directional laser performance and reduce the laser threshold, suspended 3D microlasers were fabricated by taking advantage of the flexibility offered by PBW. These suspended microlasers exhibit improved laser thresholds by a factor of 2.

Ion beam writing was implemented to fabricate waveguides in type IIa single crystal diamond by local modification of the material. The proton implantation in diamond modified the material optically and showed an increase in refractive index. This was evident from the observation of propagating optical modes in the diamond waveguides. The propagation loss measurements done on these waveguides with two different polarizations revealed high losses in the waveguides. The propagation loss observed in TM polarization is smaller compared to TE polarization. The spectroscopic analysis of the proton implantation induced effects in diamond waveguides is under progress. The AFM measurements on the implanted waveguides showed swelling of the sample at the implantation region. The room temperature photoluminescence from the diamond waveguides was observed and two color centres were

identified. The Raman measurement shows interesting peaks within the implantation region although, the nature of these peaks is unknown. All these measurements were performed on as implanted diamond sample. The ion beam writing was also employed to modify the nonlinear crystals like KTP and Nd:GGG and waveguiding was demonstrated. The low loss waveguides were reported and lasing action was observed in these waveguides.

7.2 Outlook

7.2.1 Continuation of the current work

7.2.1.1 Microlaser with electrical pumping

The current work reports the microlasers in Rhodamine B doped SU-8 polymer in which lasing was achieved through optical pumping. The microlasers based on whispering gallery mode resonators showed superior performance compared to other cavities. To integrate these cavity designs on an optical chip, it would be more feasible to have electrical pumping scheme rather than an optical one. The electrical pumping scheme is easier in a compact optical chip. So, the electrical pumping based microlasers can be realized by replacing the SU-8 polymer with some conductive polymers available.

7.2.1.2 Spectroscopic investigations of ion induced damages in Diamond

The proton induced effects studied so far are limited and the results obtained are only from the as-implanted waveguides. The propagation loss measurements indicate higher losses because of the damage caused to the diamond lattice. Other measurements like photoluminescence, atomic force microscopy, and Raman measurements were also of as-implanted sample. The lattice damage can be reduced

by annealing at optimum conditions, so the measurements have to performed after annealing at different temperatures to reduce the optical losses. It is essential to obtain low-loss waveguides in diamond making it desirable for achieving integrated diamond photonics. The systematic annealing study could help us better understand the proton irradiation induced effects in diamond lattice.

7.2.2 Compact Diamond single photon laser

The proton implantation in diamond showed room temperature photoluminescence with zero phonon lines at 470 nm and 740 nm which correspond to TR12 and GR1 color centres respectively. The TR12 color centre emits single photons [165]. This room temperature luminescence can be utilized to realize a single photon laser when the color centres are confined in a cavity. The microresonator can be fabricated in a similar fashion as the lithium niobate disk discussed in section 5.2. Different chemical compositions can be used to etch the graphitic layer formed underneath the surface when irradiated with He^+ ions above a certain threshold fluence [149]. After fabrication of the suspended microresonators, low energy proton implantation on these microresonators would confine the color centres within the cavity. Optical excitation of the cavity will result in recirculation of the light emission from the color centres emitting single photons. This approach could be followed to obtain single photon lasers. The schematic of the fabrication of diamond single photo laser can be seen from Figure 7.1.

7.2.3 Coupled resonator induced transparency in Fabry-Perot resonator embedded in ring resonator

Coupled resonator induced transparency effect is generally observed in two microresonators coupled to each other because of their close proximity. The same effect can

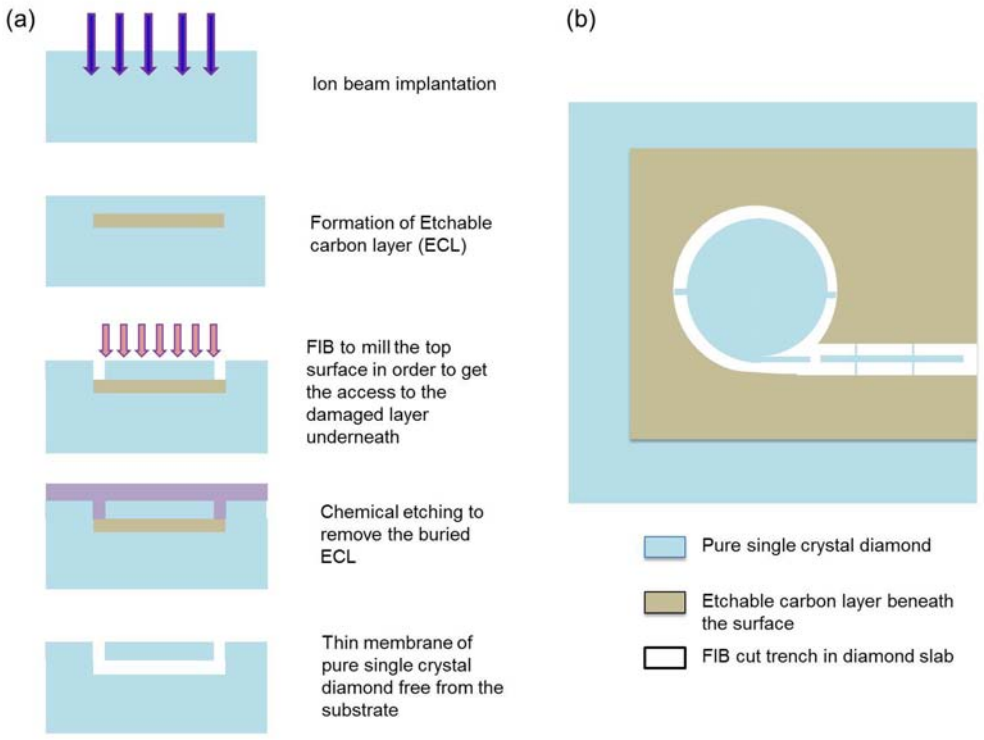

FIGURE 7.1: The schematic representation of the fabrication of the diamond single photon laser (a) shows the schematic to fabricate thin sheets of diamond (b) the top view of the final device with integrated waveguide

be observed in single ring (disk) resonator when two periodic mirrors placed in the ring resonator. Mirrors can be formed in a waveguide by patterning a set of holes with a certain periodicity. Two such set of holes separated by some distance could form a fabry perot resonator in a waveguide [184]. Similar formation can be lithographically made in a ring resonator. The FDTD simulations were performed to observe the coupled resonance phenomenon with silicon being the resonator material. A silicon ring resonator of 10 μm wide diameter and the ring width of 2 μm was designed with resonance wavelength near the telecommunication wavelengths. A set of 4 periodic holes on both sides of the cavity form the mirror. Another 4 non-periodic holes with decreasing diameters form a tapered region and are defined in the cavity to reduce the reflection losses by the periodic mirrors. The dimensions of the fabry perot resonator formation is adopted from Ref [184]. A 2 μm wide waveguide is also included near the ring resonator. An excitation pulse is launched

in the waveguide and the electric field data is collected from the end of the waveguide which gives the transmission spectrum. The schematic of the cavity design and the resulted transmission spectrum obtained from FDTD simulation carried out with RSoft software package can be seen in Figure 7.2.

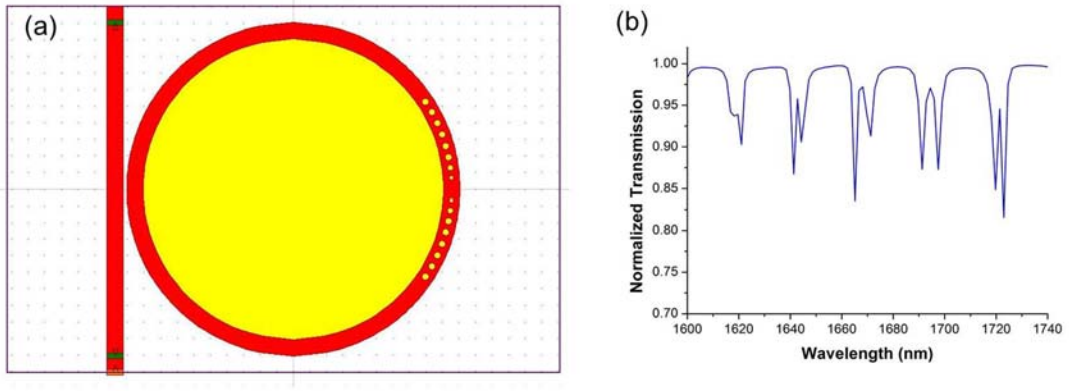

FIGURE 7.2: The coupled resonator induced transparency effect observed in Fabry Perot resonator embedded in ring resonator (a) The Rsoft CAD design showing the ring resonator with embedded air holes within the ring which serve as Fabry Perot resonator (b) Transmission spectrum of the design obtained from the electric field end of the waveguide

Bibliography

[1] Springham S.V., T.Osipowicz, J.L Sanchez, L.H. Gan, and F. Watt. Micromachining using deep ion beam lithography. *Nuclear Inst and Methods in Physics Research B*, 130:155–159, 1997. URL http://www.ciba.nus.edu.sg/publications/files/pbw/pbw1997_1.pdf.

[2] Frank Watt, Mark B.H. Breese, Andrew A. Bettiol, and Jeroen A. van Kan. Proton beam writing. *Materials Today*, 10(6):20–29, June 2007. ISSN 13697021. doi: 10.1016/S1369-7021(07)70129-3. URL http://linkinghub.elsevier.com/retrieve/pii/S1369702107701293.

[3] J a van Kan, P Malar, and Armin Baysic de Vera. The second generation Singapore high resolution proton beam writing facility. *The Review of scientific instruments*, 83(2):02B902, February 2012. ISSN 1089-7623. doi: 10.1063/1.3662205. URL http://www.ncbi.nlm.nih.gov/pubmed/22380334.

[4] Jose Luis Sanchez, G. Guy, J.A. van Kan, T.Osipowicz, and F.Watt. Proton micromachining of substrate scaolds for cellar and tissue engineering. *Nuclear Inst and Methods in Physics Research B*, 158:185–189, 1999. URL http://www.ciba.nus.edu.sg/publications/files/pbw/pbw1999_3.pdf.

[5] A.A. Bettiol, T.C. Sum, J.a. van Kan, and F. Watt. Fabrication of micro-optical components in polymer using proton beam micro-machining and modification. *Nuclear Instruments and Methods in Physics Research Section B: Beam Interactions with Materials and Atoms*, 210:250–255, September 2003. ISSN 0168583X. doi: 10.1016/S0168-583X(03)01021-8. URL http://linkinghub.elsevier.com/retrieve/pii/S0168583X03010218.

[6] J.a. van Kan, P.G. Shao, P. Molter, M. Saumer, a.a. Bettiol, T. Osipowicz, and F. Watt. Fabrication of a free standing resolution standard for focusing MeV ion beams to sub 30nm dimensions. *Nuclear Instruments and*

Methods in Physics Research Section B: Beam Interactions with Materials and Atoms, 231(1-4):170–175, April 2005. ISSN 0168583X. doi: 10.1016/j.nimb.2005.01.052. URL http://linkinghub.elsevier.com/retrieve/pii/S0168583X05000728.

[7] J. a. Kan, F. Zhang, S. Y. Chiam, T. Osipowicz, a. a. Bettiol, and F. Watt. Proton beam writing: a platform technology for nanowire production. *Microsystem Technologies*, 14(9-11):1343–1348, January 2008. ISSN 0946-7076. doi: 10.1007/s00542-007-0514-y. URL http://www.springerlink.com/index/10.1007/s00542-007-0514-y.

[8] J. a. Kan, P. G. Shao, Y. H. Wang, and P. Malar. Proton beam writing a platform technology for high quality three-dimensional metal mold fabrication for nanofluidic applications. *Microsystem Technologies*, 17(9):1519–1527, July 2011. ISSN 0946-7076. doi: 10.1007/s00542-011-1321-z. URL http://www.springerlink.com/index/10.1007/s00542-011-1321-z.

[9] T C Sum, A A Bettiol, H L Seng, I Rajta, J A Van Kan, and F Watt. Proton beam writing of passive waveguides in PMMA. *Nuclear Instruments and Methods in Physics Research Section B: Beam Interactions with Materials and Atoms*, 210:266–271, 2003. ISSN 0168583X. doi: 10.1016/S0168-583X(03)01028-0. URL http://linkinghub.elsevier.com/retrieve/pii/S0168583X03010280.

[10] H Mabuchi and H J Kimble. Atom galleries for whispering atoms: binding atoms in stable orbits around an optical resonator. *Optics Letters*, 19(10):749–751, 1994. URL http://www.ncbi.nlm.nih.gov/pubmed/19844433.

[11] Alexandre Francois and Michael Himmelhaus. Optical biosensor based on whispering gallery mode excitations in clusters of microparticles. *Applied Physics Letters*, 92(14):141107, 2008. ISSN 00036951. doi: 10.1063/1.2907491. URL http://link.aip.org/link/APPLAB/v92/i14/p141107/s1&Agg=doi.

[12] Lin Zhang Lin Zhang, Yunchu Li Yunchu Li, Jeng-Yuan Yang Jeng-Yuan Yang, Muping Song Muping Song, R G Beausoleil, and A E Willner. Silicon-Based Microring Resonator Modulators for Intensity Modulation, 2010. ISSN 1077260X. URL http://ieeexplore.ieee.org/lpdocs/epic03/wrapper.htm?arnumber=5256200.

[13] Judith R. Schwesyg, Tobias Beckmann, Anne S. Zimmermann, Karsten Buse, and Daniel Haertle. Fabrication and characterization of whispering-gallery-mode resonators made of polymers. *Optics Express*, 17(4):2573, February 2009. ISSN 1094-4087. doi: 10.1364/OE.17.002573. URL `http://www.opticsexpress.org/abstract.cfm?URI=oe-17-4-2573`.

[14] I. Rajta, S.Z. Szilasi, J. Budai, Z. Tóth, P. Petrik, and E. Baradács. Refractive index depth profile in PMMA due to proton irradiation. *Nuclear Instruments and Methods in Physics Research Section B: Beam Interactions with Materials and Atoms*, 260(1):400–404, July 2007. ISSN 0168583X. doi: 10.1016/j.nimb.2007.02.052. URL `http://linkinghub.elsevier.com/retrieve/pii/S0168583X07004302`.

[15] P. Olivero, S. Calusi, L. Giuntini, S. Lagomarsino, a. Lo Giudice, M. Massi, S. Sciortino, M. Vannoni, and E. Vittone. Controlled variation of the refractive index in ion-damaged diamond. *Diamond and Related Materials*, 19(5-6):428–431, May 2010. ISSN 09259635. doi: 10.1016/j.diamond.2009.12.011. URL `http://linkinghub.elsevier.com/retrieve/pii/S0925963509003719`.

[16] E Flores-Romero, G V Vázquez, H Márquez, R Rangel-Rojo, J Rickards, and R Trejo-Luna. Laser emission in proton-implanted Nd:YAG channel waveguides. *Optics Express*, 15(26):17874–17880, 2007.

[17] T Osipowicz. Micro-PIXE and channeling PIXE analysis of Ag-doped YBa 2 Cu 3 O 7Àd thin lms. *Nuclear Inst and Methods in Physics Research B*, 150: 543–547, 1999.

[18] F. Watt, T. Osipowicz, T.F. Choo, I. Orlic, and S.M. Tang. Nuclear microprobe analysis and imaging: Current state of the art performances. *Nuclear Instruments and Methods in Physics Research Section B: Beam Interactions with Materials and Atoms*, 136-138(97):313–317, March 1998. ISSN 0168583X. doi: 10.1016/S0168-583X(97)00710-6. URL `http://linkinghub.elsevier.com/retrieve/pii/S0168583X97007106`.

[19] M B H Breese, M A Rana, T Osipowicz, and E J Teo. Enhanced Planar Channeling of MeV Protons through Thin Crystals. *Physical Review Letters*, (September):1–4, 2004. doi: 10.1103/PhysRevLett.93.105505.

[20] T. Osipowicz, H.L. Seng, T.K. Chan, and B. Ho. The CIBA high resolution RBS facility. *Nuclear Instruments and Methods in Physics Research Section B:*

Beam Interactions with Materials and Atoms, 249(1-2):915–917, August 2006. ISSN 0168583X. doi: 10.1016/j.nimb.2006.03.198. URL `http://linkinghub.elsevier.com/retrieve/pii/S0168583X06004368`.

[21] Frank Watt, Xiao Chen, Armin Baysic De Vera, Chammika N.B. Udalagama, M. Ren, Jeroen a Van Kan, and Andrew a Bettiol. The Singapore high resolution single cell imaging facility. *Nuclear Instruments and Methods in Physics Research Section B: Beam Interactions with Materials and Atoms*, 269(20):2168–2174, October 2011. ISSN 0168583X. doi: 10.1016/j.nimb.2011.02.028. URL `http://linkinghub.elsevier.com/retrieve/pii/S0168583X11002114`.

[22] Philip J. C Breese, Mark B. H; Jamieson, David N; King. *Materials Analysis using a Nuclear Microprobe*. John Wiley, 1996. ISBN 9780471106081, 0471106089.

[23] Ton H. Bethe. Zur Theorie des Durchgangs schneller Korpuskularstrahlen durch Materie. *Annalen der Physik*, 397(3):325–400, 1930.

[24] Von H. Bloch. Zur Bremsung rasch bewegter Teilchen beim Durchgang durch Materie. *Annalen der Physik*, 408(3):285–320, 1933.

[25] D J W Mow, R G Haitsma, T Butz, R Flagmeyer, D Lehmann, and J Vogt. The novel ultrastable HVEE 3.5 MV Singletron? accelerator for nanoprobe applications. *Nuclear Inst and Methods in Physics Research B*, 130:31–36, 1997. doi: 10.1016/S0168-583X(97)00186-9. URL `http://www.sciencedirect.com.libproxy1.nus.edu.sg/science/article/pii/S0168583X97001869`.

[26] J Kuffel, E; Zaengl, W. S; Kuffel. *High voltage engineering: fundamentals*. Newnes, 2nd edition, 2000. ISBN 9780750636346, 0750636343, 008050809X, 9780080508092.

[27] Watt; G. W. Grime ; J. A. Cookson F. *Principles and applications of high-energy ion microbeams*. Hilger, 1987. ISBN 0852745176, 9780852745175.

[28] F. Watt, J.a. van Kan, I. Rajta, a.a. Bettiol, T.F. Choo, M.B.H. Breese, and T. Osipowicz. The National University of Singapore high energy ion nano-probe facility: Performance tests. *Nuclear Instruments and Methods in Physics Research Section B: Beam Interactions with Materials and Atoms*, 210:14–20, September 2003. ISSN 0168583X. doi: 10.

1016/S0168-583X(03)01003-6. URL http://linkinghub.elsevier.com/retrieve/pii/S0168583X03010036.

[29] Andrew A Bettiol, J A Van Kan, T C Sum, and F Watt. A LabVIEWe-based scanning and control system for proton beam micromachining. *Nuclear Inst and Methods in Physics Research B*, 181:49–53, 2001. URL http://www.sciencedirect.com/science/article/pii/S0168583X01005547.

[30] J A Van Kan, A A Bettiol, K Ansari, P Shao, and F Watt. Improvement in proton beam writing at the nano scale. *Micro Electro Mechanical Systems, 2004. 17th IEEE International Conference on. (MEMS)*, pages 673–676, 2004. URL http://ieeexplore.ieee.org/xpl/login.jsp?tp=&arnumber=1290674&url=http://ieeexplore.ieee.org/xpls/abs_all.jsp?arnumber=1290674.

[31] T. C. Sum, a. a. Bettiol, J. a. van Kan, F. Watt, E. Y. B. Pun, and K. K. Tung. Proton beam writing of low-loss polymer optical waveguides. *Applied Physics Letters*, 83(9):1707, 2003. ISSN 00036951. doi: 10.1063/1.1606502. URL http://link.aip.org/link/APPLAB/v83/i9/p1707/s1&Agg=doi.

[32] A.A. Bettiol, C.N.B. Udalagama, J.a. Van Kan, and F. Watt. Ionscan: scanning and control software for proton beam writing. *Nuclear Instruments and Methods in Physics Research Section B: Beam Interactions with Materials and Atoms*, 231(1-4):400–406, April 2005. ISSN 0168583X. doi: 10.1016/j.nimb.2005.01.090. URL http://linkinghub.elsevier.com/retrieve/pii/S0168583X05001102.

[33] Chammika N.B. Udalagama, Andrew a. Bettiol, J.a. van Kan, and Frank Watt. Proton beam micromachining dose normalization for SU-8 using ionoluminescence detection. *Nuclear Instruments and Methods in Physics Research Section B: Beam Interactions with Materials and Atoms*, 210:256–259, September 2003. ISSN 0168583X. doi: 10.1016/S0168-583X(03)01023-1. URL http://linkinghub.elsevier.com/retrieve/pii/S0168583X03010231.

[34] Andrew a. Bettiol, Kambiz Ansari, Tze Chien Sum, Jeroen a. van Kan, and Frank Watt. Fabrication of micro-optical components in polymer using proton beam writing. *Proceedings of SPIE*, 5347:255–263, January 2004. doi: 10.1117/12.524300. URL http://spiedigitallibrary.org/proceeding.aspx?doi=10.1117/12.524300.

[35] Jeroen A. van Kan, Andrew A Bettiol, Kambiz Ansari, Ee Jin Teo, Tze Chien Sum, and Frank Watt. Proton beam writing : a progress review. *International Journal of Nanotechnology*, 1(4):464–479, 2004. doi: DOI:10.1504/IJNT.2004.005980. URL http://www.inderscience.com/info/inarticle.php?artid=5980.

[36] T. C. Sum, a. a. Bettiol, H. L. Seng, J. a. Van Kan, and F. Watt. Direct measurement of proton-beam-written polymer optical waveguide sidewall morphorlogy using an atomic force microscope. *Applied Physics Letters*, 85(8):1398, 2004. ISSN 00036951. doi: 10.1063/1.1784035. URL http://link.aip.org/link/APPLAB/v85/i8/p1398/s1&Agg=doi.

[37] K. Ansari, J. a. van Kan, a. a. Bettiol, and F. Watt. Fabrication of high aspect ratio 100nm metallic stamps for nanoimprint lithography using proton beam writing. *Applied Physics Letters*, 85(3):476, 2004. ISSN 00036951. doi: 10.1063/1.1773933. URL http://link.aip.org/link/APPLAB/v85/i3/p476/s1&Agg=doi.

[38] Bean K. E. Anisotropic Etching of Silicon. *IEEE TRANSACTIONS ON ELECTRON DEVICES*, ED-25(10):1185–1193, 1978. doi: 10.1109/T-ED.1978.19250. URL http://ieeexplore.ieee.org/xpl/login.jsp?tp=&arnumber=1479644&url=http://ieeexplore.ieee.org/xpls/abs_all.jsp?arnumber=1479644.

[39] E J Teo, a a Bettiol, P Yang, M B H Breese, B Q Xiong, G Z Mashanovich, W R Headley, and G T Reed. Fabrication of low-loss silicon-on-oxidized-porous-silicon strip waveguide using focused proton-beam irradiation. *Optics letters*, 34(5):659–61, March 2009. ISSN 0146-9592. URL http://www.ncbi.nlm.nih.gov/pubmed/19252584.

[40] Ee Jin Teo, Andrew a Bettiol, Boqian Xiong, Mark B H Breese, and Prashant T Shuvan. An all-silicon, single-mode Bragg cladding rib waveguide. *Optics express*, 18(9):8816–23, April 2010. ISSN 1094-4087. URL http://www.ncbi.nlm.nih.gov/pubmed/20588726.

[41] P. Y. Yang, G. Z. Mashanovich, I. Gomez-Morilla, W. R. Headley, G. T. Reed, E. J. Teo, D. J. Blackwood, M. B. H. Breese, and a. a. Bettiol. Free-standing waveguides in silicon. *Applied Physics Letters*, 90(24):241109, 2007. ISSN 00036951. doi: 10.1063/1.2749175. URL http://link.aip.org/link/APPLAB/v90/i24/p241109/s1&Agg=doi.

[42] I. Rajta, I. Gómez-Morilla, M.H. Abraham, and Á.Z. Kiss. Proton beam micromachining on PMMA, Foturan and CR-39 materials. *Nuclear Instruments and Methods in Physics Research Section B: Beam Interactions with Materials and Atoms*, 210:260–265, September 2003. ISSN 0168583X. doi: 10.1016/S0168-583X(03)01025-5. URL `http://linkinghub.elsevier.com/retrieve/pii/S0168583X03010255`.

[43] T C Sum, A A Bettiol, C Florea, and F Watt. Proton-beam writing of polymethylmethacrylate buried channel waveguides, 2006. ISSN 07338724.

[44] A. A. Bettiol, S. Venugopal Rao, E. J. Teo, J. a. van Kan, and Frank Watt. Fabrication of buried channel waveguides in photosensitive glass using proton beam writing. *Applied Physics Letters*, 88(17):171106, 2006. ISSN 00036951. doi: 10.1063/1.2198798. URL `http://link.aip.org/link/APPLAB/v88/i17/p171106/s1&Agg=doi`.

[45] A.A. Bettiol, T.C. Sum, F.C. Cheong, C.H. Sow, S. Venugopal Rao, J.a. van Kan, E.J. Teo, K. Ansari, and F. Watt. A progress review of proton beam writing applications in microphotonics. *Nuclear Instruments and Methods in Physics Research Section B: Beam Interactions with Materials and Atoms*, 231(1-4):364–371, April 2005. ISSN 0168583X. doi: 10.1016/j.nimb.2005.01.084. URL `http://linkinghub.elsevier.com/retrieve/pii/S0168583X05001047`.

[46] R Huszank, S Z Szilasi, I Rajta, and A Csik. Fabrication of optical devices in poly(dimethylsiloxane) by proton microbeam. *Optics Communications*, 283 (1):176–180, 2010. ISSN 00304018. doi: 10.1016/j.optcom.2009.09.066. URL `http://linkinghub.elsevier.com/retrieve/pii/S0030401809009432`.

[47] S Z Szilasi, N Hegman, A Csik, and I Rajta. Creation of convex microlenses in PDMS with focused MeV ion beam. *Microelectronic Engineering*, 88(9): 2885–2888, 2011. ISSN 01679317. doi: 10.1016/j.mee.2011.03.007.

[48] Vladimir M. Shalaev. Optical negative-index metamaterials. *Nature Photonics*, 1(1):41–48, January 2007. ISSN 1749-4885. doi: 10.1038/nphoton.2006.49. URL `http://www.nature.com/doifinder/10.1038/nphoton.2006.49`.

[49] Sher-Yi Chiam, Jiaguang Han, Ranjan Singh, Weili Zhang, Thomas Osipowicz, and Andrew a. Bettiol. Spectral Properties of Thick Split Ring Resonators in the THz regime. *Proceedings of SPIE*, 6893(65):68930A–68930A–8, February 2008. doi: 10.1117/12.762369. URL http://proceedings.spiedigitallibrary.org/proceeding.aspx?doi=10.1117/12.762369.

[50] Sher-Yi Chiam, Ranjan Singh, Jianqiang Gu, Jiaguang Han, Weili Zhang, and Andrew a. Bettiol. Increased frequency shifts in high aspect ratio terahertz split ring resonators. *Applied Physics Letters*, 94(6):064102, 2009. ISSN 00036951. doi: 10.1063/1.3079419. URL http://link.aip.org/link/APPLAB/v94/i6/p064102/s1&Agg=doi.

[51] Lord Rayleigh. The Problem of the Whispering Gallery. *Philosophical Magazine Series 6*, 20(120):1001–1004, 1910. doi: 10.1080/14786441008636993. URL http://www.tandfonline.com/doi/abs/10.1080/14786441008636993.

[52] A N Oraevsky. Whispering-gallery waves. *Quantum Electronics*, 32(5):377–400, 2002. doi: 10.1070/QE2001v031n05ABEH002205. URL http://iopscience.iop.org/1063-7818/32/5/R01.

[53] Peter Walsh and G. Kemeny. Laser Operation Without Spikes in a Ruby Ring. *Journal of Applied Physics*, 34(4):956, 1963. ISSN 00218979. doi: 10.1063/1.1729570. URL http://link.aip.org/link/JAPIAU/v34/i4/p956/s1&Agg=doi.

[54] Mohammad Soltani, Siva Yegnanarayanan, and Ali Adibi. Ultra-high Q planar silicon microdisk resonators for chip-scale silicon photonics. *Optics express*, 15(8):4694–704, April 2007. ISSN 1094-4087. URL http://www.ncbi.nlm.nih.gov/pubmed/19532715.

[55] Ming Cai Ming Cai, G Hunziker, and K Vahala. Fiber-optic add-drop device based on a silica microsphere-whispering gallery mode system, 1999. ISSN 10411135. URL http://ieeexplore.ieee.org/lpdocs/epic03/wrapper.htm?arnumber=766785.

[56] Jan Niehusmann, Andreas Vörckel, Peter Haring Bolivar, Thorsten Wahlbrink, Wolfgang Henschel, and Heinrich Kurz. Ultrahigh-quality-factor silicon-on-insulator microring resonator. *Optics Letters*, 29(24):2861–2863, 2004. URL http://www.ncbi.nlm.nih.gov/pubmed/15645805.

[57] Xinzheng Zhang, Xuejin Zhang, Jiabin Xu, Xudong Shan, Jun Xu, and Dapeng Yu. Whispering gallery modes in single triangular ZnO nanorods. *Optics Letters*, 34(16):2533–2535, 2009. URL http://www.ncbi.nlm.nih.gov/pubmed/19684840.

[58] Shengmei Zheng Shengmei Zheng, Ning Ma Ning Ma, and A W Poon. Experimental demonstration of waveguide-coupled hexagonal micropillar resonators with round-corners in silicon nitride, 2005. URL http://ieeexplore.ieee.org/lpdocs/epic03/wrapper.htm?arnumber=1572873.

[59] Kerry J Vahala. *Optical microcavities*. World Scientific, 2004. ISBN 9789812387752, 9812387757.

[60] Uriel Levy, Kyle Campbell, Alex Groisman, Shayan Mookherjea, and Yeshaiahu Fainman. On-chip microfluidic tuning of an optical microring resonator. *Applied Physics Letters*, 88(11):111107, 2006. ISSN 00036951. doi: 10.1063/1.2182111. URL http://link.aip.org/link/APPLAB/v88/i11/p111107/s1&Agg=doi.

[61] G T Paloczi, Y Huang, and A Yariv. Free standing all polymer resonator optical filter. *ELECTRONIC LETTERS*, 39(23):3–4, 2003. doi: 10.1049/el. URL http://ieeexplore.ieee.org/xpl/articleDetails.jsp;jsessionid=tpP3P4TVxkvcMDYjLq80WJl2HxypQ1y4PVJTc92mgQkHLjDXnhKG!238098542?arnumber=1248963&contentType=Journals+&+Magazines.

[62] T Sherwood, A C Young, J Takayesu, A K Y Jen, L R Dalton, and Antao Chen Antao Chen. Microring resonators on side-polished optical fiber, 2005. ISSN 10411135. URL http://ieeexplore.ieee.org/lpdocs/epic03/wrapper.htm?arnumber=1512288.

[63] A Leinse, M B J Diemeer, A Rousseau, and A Driessen. A novel high-speed polymeric EO Modulator based on a combination of a microring resonator and an MZI, 2005. ISSN 10411135. URL http://ieeexplore.ieee.org/lpdocs/epic03/wrapper.htm?arnumber=1512277.

[64] Chung-yen Chao and L Jay Guo. Polymer microring resonators fabricated by nanoimprint technique. *Journal of Vacuum Science and Technology B: Microelectronics and Nanometer Structures*, 20(6):2862, 2002. ISSN 0734211X. doi: 10.1116/1.1521729. URL http://link.aip.org/link/JVTBD9/v20/i6/p2862/s1&Agg=doi.

[65] M L Gorodetsky, a a Savchenkov, and V S Ilchenko. Ultimate Q of optical microsphere resonators. *Optics letters*, 21(7):453–5, April 1996. ISSN 0146-9592. URL http://www.ncbi.nlm.nih.gov/pubmed/19865436.

[66] F Morichetti, A Melloni, M Martinelli, R G Heideman, A Leinse, D H Geuzebroek, and A Borreman. Box-Shaped Dielectric Waveguides: A New Concept in Integrated Optics?, 2007. ISSN 07338724. URL http://ieeexplore.ieee.org/lpdocs/epic03/wrapper.htm?arnumber=4298997.

[67] Ming-Chun Tien, Jared F Bauters, Martijn J R Heck, Daryl T Spencer, Daniel J Blumenthal, and John E Bowers. Ultra-high quality factor planar Si3N4 ring resonators on Si substrates. *Optics express*, 19(14):13551–6, July 2011. ISSN 1094-4087. URL http://www.ncbi.nlm.nih.gov/pubmed/21747510.

[68] E Shah Hosseini, S Yegnanarayanan, and A Adibi. High quality factor silicon nitride microdisk resonators for chip-scale visible sensing, 2009. URL http://ieeexplore.ieee.org/lpdocs/epic03/wrapper.htm?arnumber=4771669.

[69] D K Armani, T J Kippenberg, S M Spillane, and K J Vahala. Ultra-high-Q toroid microcavity on a chip. *Nature*, 421(6926):925–928, 2003. URL http://www.ncbi.nlm.nih.gov/pubmed/12606995.

[70] Mani Hossein-Zadeh and Kerry J Vahala. Free ultra-high-Q microtoroid: a tool for designing photonic devices. *Optics express*, 15(1):166–75, January 2007. ISSN 1094-4087. URL http://www.ncbi.nlm.nih.gov/pubmed/19532232.

[71] Po Dong, Roshanak Shafiiha, Shirong Liao, Hong Liang, Ning-Ning Feng, Dazeng Feng, Guoliang Li, Xuezhe Zheng, Ashok V Krishnamoorthy, and Mehdi Asghari. Wavelength-tunable silicon microring modulator. *Optics express*, 18(11):10941–6, May 2010. ISSN 1094-4087. URL http://www.ncbi.nlm.nih.gov/pubmed/20588949.

[72] Tao Ling, Sung-Liang Chen, and L Jay Guo. Fabrication and characterization of high Q polymer micro-ring resonator and its application as a sensitive ultrasonic detector. *Optics express*, 19(2):861–9, January 2011. ISSN 1094-4087. URL http://www.pubmedcentral.nih.gov/articlerender.fcgi?artid=3368304&tool=pmcentrez&rendertype=abstract.

[73] Po Dong, Wei Qian, Hong Liang, Roshanak Shafiiha, Ning-Ning Feng, Dazeng Feng, Xuezhe Zheng, Ashok V Krishnamoorthy, and Mehdi Asghari. Low power and compact reconfigurable multiplexing devices based on silicon microring resonators. *Optics express*, 18(10):9852–8, May 2010. ISSN 1094-4087. URL `http://www.ncbi.nlm.nih.gov/pubmed/20588834`.

[74] John E. Heebner and Robert W. Boyd. SLOW AND STOPPED LIGHT 'Slow' and 'fast' light in resonator-coupled waveguides. *Journal of Modern Optics*, 49(14-15):2629–2636, November 2002. ISSN 0950-0340. doi: 10.1080/0950034021000011527. URL `http://www.tandfonline.com/doi/abs/10.1080/09500340210000011527`.

[75] S. M. Spillane, T. J. Kippenberg, and K. J. Vahala. Ultrahigh- Q toroidal microresonators for cavity quantum electrodynamics. *Physical Review A*, 71 (1):1–10, January 2005. ISSN 1050-2947. doi: 10.1103/PhysRevA.71.013817. URL `http://link.aps.org/doi/10.1103/PhysRevA.71.013817`.

[76] Payam Rabiei, Student Member, William H Steier, Life Fellow, Cheng Zhang, and Larry R Dalton. Polymer Micro-Ring Filters and Modulators. *Journal of Lightwave Technology*, 20(11):1968–1975, 2002.

[77] Fengnian Xia, Lidija Sekaric, and Yurii Vlasov. Ultracompact optical buffers on a silicon chip. *Nature Photonics*, 1(1):65–71, January 2007. ISSN 1749-4885. doi: 10.1038/nphoton.2006.42. URL `http://www.nature.com/doifinder/10.1038/nphoton.2006.42`.

[78] David Smith, Hongrok Chang, Kirk Fuller, a. Rosenberger, and Robert Boyd. Coupled-resonator-induced transparency. *Physical Review A*, 69(6):1–6, June 2004. ISSN 1050-2947. doi: 10.1103/PhysRevA.69.063804. URL `http://link.aps.org/doi/10.1103/PhysRevA.69.063804`.

[79] Frank Vollmer and Stephen Arnold. Whispering-gallery-mode biosensing : label- free detection down to single molecules. *Nature Methods*, 5(7):591–596, 2008. doi: 10.1038/NMETH.1221. URL `http://www.nature.com/nmeth/journal/v5/n7/abs/nmeth.1221.html`.

[80] Yong Ma, Gilbert Chang, Seoijin Park, Liwei Wang, and Seng Tiong Ho. InGaAsP thin-film microdisk resonators fabricated by polymer wafer bonding for wavelength add-drop filters. *IEEE Photonics Technology Letters*, 12(11):1495–1497, November 2000. ISSN 1041-1135. doi: 10.1109/

68.887713. URL http://ieeexplore.ieee.org/lpdocs/epic03/wrapper.htm?arnumber=887713.

[81] a. Rastelli, a. Ulhaq, Ch. Deneke, L. Wang, M. Benyoucef, E. Coric, W. Winter, S. Mendach, F. Horton, F. Cavallo, T. Merdzhanova, S. Kiravittaya, and O. G. Schmidt. Fabrication and characterization of microdisk resonators with In(Ga)As/GaAs quantum dots. *Physica Status Solidi (C)*, 3(11):3641–3645, December 2006. ISSN 16101634. doi: 10.1002/pssc.200671502. URL http://doi.wiley.com/10.1002/pssc.200671502.

[82] B E Little, J S Foresi, G Steinmeyer, E R Thoen, S T Chu, H A Haus, E P Ippen, L C Kimerling, and W Greene. Ultra-Compact Si SiO Microring Resonator. *Technology*, 10(4):549–551, 1998. ISSN 10411135. doi: 10.1109/68.662590. URL http://ieeexplore.ieee.org/xpls/abs_all.jsp?arnumber=662590.

[83] D Rafizadeh, J P Zhang, R C Tiberio, and S T Ho. Propagation Loss Measurements in Semiconductor Microcavity Ring and Disk Resonators. *Journal of Lightwave Technology*, 16(7):1308–1314, 1998. URL http://www.opticsinfobase.org/jlt/abstract.cfm?uri=jlt-16-7-1308.

[84] MicroChemCorporation. URL http://microchem.com/.

[85] Om Prakash Parida and Navakant Bhat. CHARACTERIZATION OF OPTICAL PROPERTIES OF SU-8 AND FABRICATION OF OPTICAL COMPONENETS. *INternational Conference on Optics and Photonocs*, pages 4–7, 2009. URL http://www.csio.res.in:8085/icop/contents/Poster/PosterSession3/OpticalNetworksandComponents/PS3_E.8_OmPrakashParida(2).pdf.

[86] B Bêche, N Pelletier, E Gaviot, and J Zyss. Single-mode TE00TM00 optical waveguides on SU-8 polymer. *Optics Communications*, 230(1-3):91–94, 2004. ISSN 00304018. doi: 10.1016/j.optcom.2003.11.016. URL http://linkinghub.elsevier.com/retrieve/pii/S0030401803022338.

[87] Xudi Wang, Yanlin Liao, Bin Liu, Liangjin Ge, Guanghua Li, Shaojun Fu, Yifang Chen, and Zheng Cui. Free-standing SU-8 subwavelength gratings fabricated by UV curing imprint. *Microelectronic Engineering*, 85(5-6):910–913, 2008. ISSN 01679317. doi: 10.1016/j.mee.2007.12.060. URL http://linkinghub.elsevier.com/retrieve/pii/S0167931707008167.

[88] Bo Yang, Liu Yang, Rui Hu, Zhen Sheng, Daoxin Dai, and Qingkun Liu. Fabrication and Characterization of Small Optical Ridge Waveguides Based on SU-8 Polymer. *Journal of Lightwave Technology*, 27(18):4091–4096, September 2009. ISSN 0733-8724. doi: 10.1109/JLT.2009.2022285. URL http://ieeexplore.ieee.org/lpdocs/epic03/wrapper.htm?arnumber=4912305.

[89] Xuelian Zhu, Yongan Xu, and Shu Yang. Distortion of 3D SU8 photonic structures fabricated by four-beam holographic lithography withumbrella configuration. *Optics Express*, 15(25):16546–16560, 2007. URL http://www.opticsinfobase.org/abstract.cfm?URI=oe-15-25-16546.

[90] Willyan Hasenkamp, David Forchelet, Kristopher Pataky, Jimmy Villard, Harald Van Lintel, Arnaud Bertsch, Qing Wang, and Philippe Renaud. Polyimide/SU-8 catheter-tip MEMS gauge pressure sensor. *Biomedical microdevices*, 14(5):819–28, October 2012. ISSN 1572-8781. doi: 10.1007/s10544-012-9661-8. URL http://www.pubmedcentral.nih.gov/articlerender.fcgi?artid=3444706&tool=pmcentrez&rendertype=abstract.

[91] Brian Bilenberg, Torben Rasmussen, Soren Balslev, and Anders Kristensen. Real-time tunability of chip-based light source enabled by microfluidic mixing. *Journal of Applied Physics*, 99(2):023102, 2006. ISSN 00218979. doi: 10.1063/1.2163011. URL http://link.aip.org/link/JAPIAU/v99/i2/p023102/s1&Agg=doi.

[92] Hironobu Sato, Hirokazu Matsumura, Satoshi Keino, and Shuichi Shoji. An all SU-8 microfluidic chip with built-in 3D fine microstructures. *Journal of Micromechanics and Microengineering*, 16(11):2318–2322, 2006. ISSN 09601317. doi: 10.1088/0960-1317/16/11/010. URL http://stacks.iop.org/0960-1317/16/i=11/a=010?key=crossref.58d73815752e23d8272453fcd2d22819.

[93] James Ziegler - SRIM & TRIM. URL http://www.srim.org/.

[94] C.-Y. Chao and L.J. Guo. Reduction of Surface Scattering Loss in Polymer Microrings Using Thermal-Reflow Technique. *IEEE Photonics Technology Letters*, 16(6):1498–1500, June 2004. ISSN 1041-1135. doi: 10.1109/LPT.2004.827413. URL http://ieeexplore.ieee.org/lpdocs/epic03/wrapper.htm?arnumber=1300644.

[95] P. Koonath, T. Indukuri, and B. Jalali. Monolithic 3-D silicon photonics. *Journal of Lightwave Technology*, 24(4):1796–1804, April 2006. ISSN 0733-8724. doi: 10.1109/JLT.2006.871121. URL http://ieeexplore.ieee.org/lpdocs/epic03/wrapper.htm?arnumber=1618769.

[96] Daniele Rezzonico, Andrea Guarino, Christian Herzog, Mojca Jazbinsek, and Peter Günter. High-Finesse Laterally Coupled Organic Inorganic Hybrid Polymer Microring Resonators for VLSI Photonics. *IEEE Photonics Technology Letters*, 18(7):865–867, 2006. doi: 10.1109/LPT.2006.871816. URL http://ieeexplore.ieee.org/xpl/login.jsp?tp=&arnumber=1608188&url=http://ieeexplore.ieee.org/iel5/68/33733/01608188.pdf?arnumber=1608188.

[97] Allen Taflove. Application of the Finite-Difference Time-Domain Method to Sinusoidal Steady-State Electromagnetic-Penetration Problems. *Ieee Transactions On Electromagnetic Compatibility*, EMC-22(3):191–202, 1980. ISSN 00189375. doi: 10.1109/TEMC.1980.303879. URL http://ieeexplore.ieee.org/xpls/abs_all.jsp?arnumber=4091372.

[98] RSoft: The Source for Photonic & Network Design Software. URL http://www.rsoftdesign.com/.

[99] B.E. Little, S.T. Chu, H.a. Haus, J. Foresi, and J.-P. Laine. Microring resonator channel dropping filters. *Journal of Lightwave Technology*, 15(6):998–1005, June 1997. ISSN 07338724. doi: 10.1109/50.588673. URL http://ieeexplore.ieee.org/lpdocs/epic03/wrapper.htm?arnumber=588673.

[100] V Sandoghdar, F Treussart, J Hare, V Lefèvre-Seguin, J Raimond, and S Haroche. Very low threshold whispering-gallery-mode microsphere laser. *Physical review. A*, 54(3):R1777–R1780, September 1996. ISSN 1050-2947. URL http://www.ncbi.nlm.nih.gov/pubmed/9913762.

[101] Ebinazar B. Namdas, Minghong Tong, Peter Ledochowitsch, Sarah R. Mednick, Jonathan D. Yuen, Daniel Moses, and Alan J. Heeger. Low Thresholds in Polymer Lasers on Conductive Substrates by Distributed Feedback Nanoimprinting: Progress Toward Electrically Pumped Plastic Lasers. *Advanced Materials*, 21(7):799–802, February 2009. ISSN 09359648. doi: 10.1002/adma.200802436. URL http://doi.wiley.com/10.1002/adma.200802436.

[102] Marko Loncar, Tomoyuki Yoshie, Axel Scherer, Pawan Gogna, and Yueming Qiu. Low-threshold photonic crystal laser. *Applied Physics Letters*, 81(15): 2680, 2002. ISSN 00036951. doi: 10.1063/1.1511538. URL `http://link.aip.org/link/APPLAB/v81/i15/p2680/s1&Agg=doi`.

[103] Q. Song, L. Ge, a. Stone, H. Cao, J. Wiersig, J.-B. Shim, J. Unterhinninghofen, W. Fang, and G. Solomon. Directional Laser Emission from a Wavelength-Scale Chaotic Microcavity. *Physical Review Letters*, 105(10): 103902, August 2010. ISSN 0031-9007. doi: 10.1103/PhysRevLett.105.103902. URL `http://link.aps.org/doi/10.1103/PhysRevLett.105.103902`.

[104] M. Lebental, J. S. Lauret, R. Hierle, and J. Zyss. Highly directional stadium-shaped polymer microlasers. *Applied Physics Letters*, 88(3):031108, 2006. ISSN 00036951. doi: 10.1063/1.2159099. URL `http://link.aip.org/link/APPLAB/v88/i3/p031108/s1&Agg=doi`.

[105] Liangmin Zhang, You-xiong Wang, Fajian Zhang, and Richard O Claus. Observation of whispering-gallery and directional resonant laser emission in ellipsoidal microcavities. *Journal of the Optical Society of America B*, 23(9), 2006. doi: 10.1364/JOSAB.23.001793. URL `http://www.opticsinfobase.org/josab/abstract.cfm?uri=josab-23-9-1793`.

[106] Qi Jie Wang, Changling Yan, Nanfang Yu, Julia Unterhinninghofen, Jan Wiersig, Christian Pflügl, Laurent Diehl, Tadataka Edamura, Masamichi Yamanishi, Hirofumi Kan, and Federico Capasso. Whispering-gallery mode resonators for highly unidirectional laser action. *Proceedings of the National Academy of Sciences of the United States of America*, 107 (52):22407–12, December 2010. ISSN 1091-6490. doi: 10.1073/pnas.1015386107. URL `http://www.pubmedcentral.nih.gov/articlerender.fcgi?artid=3012530&tool=pmcentrez&rendertype=abstract`.

[107] Naoki Tsujimoto, Tetsuya Takashima, Takashi Nakao, Kimihiro Masuyama, Akihiko Fujii, and Masanori Ozaki. Laser emission from spiral-shaped microdisc with waveguide of conducting polymer. *Journal of Physics D: Applied Physics*, 40(6):1669–1672, March 2007. ISSN 0022-3727. doi: 10.1088/0022-3727/40/6/015. URL `http://stacks.iop.org/0022-3727/40/i=6/a=015?key=crossref.36631d36ec135b3d16c9a0fd7c42acc7`.

[108] T. Ben-Messaoud and J. Zyss. Unidirectional laser emission from polymer-based spiral microdisks. *Applied Physics Letters*, 86(24):241110, 2005. ISSN

00036951. doi: 10.1063/1.1949708. URL http://link.aip.org/link/APPLAB/v86/i24/p241110/s1&Agg=doi.

[109] Kenichi Yamashita, Hisao Yanagi, and Kunishige Oe. Array of a dye-doped polymer-based microlaser with multiwavelength emission. *Optics letters*, 36 (10):1875–7, May 2011. ISSN 1539-4794. URL http://www.ncbi.nlm.nih.gov/pubmed/21593920.

[110] M Lu, B T Cunningham, S J Park, and J G Eden. Vertically emitting, dye-doped polymer laser in the green (λ536nm) with a second order distributed feedback grating fabricated by replica molding. *Optics Communications*, 281(11):3159–3162, 2008. ISSN 00304018. doi: 10.1016/j.optcom.2008.02.020. URL http://linkinghub.elsevier.com/retrieve/pii/S0030401808001284.

[111] Tashiyuki Komikado, Azusa Inoue, Koichi Mas, Takashi Ando, and Shins Umegaki. A Surface-Emitting Distributed-Feedback Dye Laser Fabricated by Spin-Coating Organic Polymers. *Conference on Lasers & Electro-Optics (CLEO)*, 3:2016–2018, 2005. doi: 10.1109/CLEO.2005.202353. URL http://ieeexplore.ieee.org/xpl/articleDetails.jsp?arnumber=1573419.

[112] Yuhua Huang, Tsung-Hsien Lin, Ying Zhou, and Shin-Tson Wu. Enhancing the laser power by stacking multiple dye-doped chiral polymer films. *Optics express*, 14(23):11299–303, November 2006. ISSN 1094-4087. URL http://www.ncbi.nlm.nih.gov/pubmed/19529545.

[113] Mads B Christiansen, Thomas Buß, Cameron L C Smith, Sidsel R Petersen, Mette M Jø rgensen, and Anders Kristensen. Single mode dye-doped polymer photonic crystal lasers. *Journal of Micromechanics and Microengineering*, 20(11):115025, 2010. ISSN 09601317. doi: 10.1088/0960-1317/20/11/115025. URL http://stacks.iop.org/0960-1317/20/i=11/a=115025?key=crossref.53583a3918a459550e64dbbbf0900fd7.

[114] Feng Jin, Chun-Fang Li, Xian-Zi Dong, Wei-Qiang Chen, and Xuan-Ming Duan. Laser emission from dye-doped polymer film in opal photonic crystal cavity. *Applied Physics Letters*, 89(24):241101, 2006. ISSN 00036951. doi: 10.1063/1.2404941. URL http://link.aip.org/link/APPLAB/v89/i24/p241101/s1&Agg=doi.

[115] Sø ren Balslev, Andrej Mironov, Daniel Nilsson, and Anders Kristensen. Micro-fabricated single mode polymer dye laser. *Optics express*, 14(6):2170–7, March 2006. ISSN 1094-4087. URL http://www.ncbi.nlm.nih.gov/pubmed/19503550.

[116] D Luo, X W Sun, H T Dai, Y J Liu, H Z Yang, and W Ji. Two-directional lasing from a dye-doped two-dimensional hexagonal photonic crystal made of holographic polymer-dispersed liquid crystals. *Applied Physics Letters*, 95 (15):151115, 2009. ISSN 00036951. doi: 10.1063/1.3251078. URL http://link.aip.org/link/APPLAB/v95/i15/p151115/s1&Agg=doi.

[117] S. Frolov, M. Shkunov, Z. Vardeny, and K. Yoshino. Ring microlasers from conducting polymers. *Physical Review B*, 56(8):R4363–R4366, August 1997. ISSN 0163-1829. doi: 10.1103/PhysRevB.56.R4363. URL http://link.aps.org/doi/10.1103/PhysRevB.56.R4363.

[118] S. V. Frolov, a. Fujii, D. Chinn, Z. V. Vardeny, K. Yoshino, and R. V. Gregory. Cylindrical microlasers and light emitting devices from conducting polymers. *Applied Physics Letters*, 72(22):2811, 1998. ISSN 00036951. doi: 10.1063/1.121466. URL http://link.aip.org/link/APPLAB/v72/i22/p2811/s1&Agg=doi.

[119] Martin Djiango, Takeyuki Kobayashi, Werner J. Blau, Bin Cai, Kyoji Komatsu, and Toshikuni Kaino. Near-infrared luminescent polymer waveguides and microlasers. *Proceedings of SPIE*, 6891:68910Y–68910Y–10, February 2008. doi: 10.1117/12.763225. URL http://proceedings.spiedigitallibrary.org/proceeding.aspx?doi=10.1117/12.763225.

[120] Tobias Grossmann, Simone Schleede, Mario Hauser, Mads Brokner Christiansen, Christoph Vannahme, Carsten Eschenbaum, Sonke Klinkhammer, Torsten Beck, Jochen Fuchs, G. Ulrich Nienhaus, Uli Lemmer, Anders Kristensen, Timo Mappes, and Heinz Kalt. Low-threshold conical microcavity dye lasers. *Applied Physics Letters*, 97(6):063304, 2010. ISSN 00036951. doi: 10.1063/1.3479532. URL http://link.aip.org/link/APPLAB/v97/i6/p063304/s1&Agg=doi.

[121] Aparna V Deshpande and Ebinazar B Namdas. Correlation between lasing and photophysical performance of dyes in polymethylmethacrylate. *Journal of Luminescence*, 91(1-2):25–31, September 2000. ISSN 00222313. doi:

10.1016/S0022-2313(00)00210-6. URL http://linkinghub.elsevier.com/retrieve/pii/S0022231300002106.

[122] Singapore — Sigma-Aldrich. URL http://www.sigmaaldrich.com/singapore.html.

[123] M Lebental, J S Lauret, J Zyss, C Schmit, and E Bogomolny. Directional emission of stadium-shaped micro-lasers. *October*, 1(3):4, 2006. URL http://arxiv.org/abs/physics/0609009.

[124] Myung-Woon Kim, Kyu-Won Park, Chang-Hwan Yi, and Chil-Min Kim. Directional and low-divergence emission in a rounded half-moon shaped microcavity. *Applied Physics Letters*, 98(24):241110, 2011. ISSN 00036951. doi: 10.1063/1.3598406. URL http://link.aip.org/link/APPLAB/v98/i24/p241110/s1&Agg=doi.

[125] Prakash Koonath, Tejaswi Indukuri, and Bahram Jalali. Vertically-coupled micro-resonators realized using three-dimensional sculpting in silicon. *Applied Physics Letters*, 85(6):1018, 2004. ISSN 00036951. doi: 10.1063/1.1781370. URL http://link.aip.org/link/APPLAB/v85/i6/p1018/s1&Agg=doi.

[126] Xiankai Sun, Xufeng Zhang, and Hong X. Tang. High-Q silicon optomechanical microdisk resonators at gigahertz frequencies. *Applied Physics Letters*, 100(17):173116, 2012. ISSN 00036951. doi: 10.1063/1.4709416. URL http://link.aip.org/link/APPLAB/v100/i17/p173116/s1&Agg=doi.

[127] G. Pucker, M. Ghulinyan, A. Pitanti, M. Xie, D. Navarro-Urrios, A. Lui, L. Pavesi, and A. Simoni. Silicon quantum dots in microdisk resonators:Whispering-gallery modes, stress-induced Q-factor tuning and enhancement. *Proceedings of SPIE*, 7366:73660M–73660M–12, May 2009. doi: 10.1117/12.821603. URL http://proceedings.spiedigitallibrary.org/proceeding.aspx?doi=10.1117/12.821603.

[128] E.J Teo, E.P Tavernier, M.B.H Breese, a.a Bettiol, F Watt, M.H Liu, and D.J Blackwood. Three-dimensional micromachining of silicon using a nuclear microprobe. *Nuclear Instruments and Methods in Physics Research Section B: Beam Interactions with Materials and Atoms*, 222(3-4):513–517, August 2004. ISSN 0168583X. doi: 10.1016/j.nimb.2004.04.159. URL http://linkinghub.elsevier.com/retrieve/pii/S0168583X04007189.

[129] OW YUEH SHENG. *Micromachining of Silicon via ION Irradiation with Porous Silicon Formation*. PhD thesis, National Univeristy of Singapore, 2010. URL http://scholarbank.nus.edu.sg/handle/10635/20958.

[130] V Lehmann and U Gijsele. Porous silicon formation: A quantum wire effect. *Applied Physics Letters*, 58(February):856–858, 1991. doi: 10.1063/1.104512. URL http://apl.aip.org/resource/1/applab/v58/i8/p856_s1.

[131] L. Jia, S. L. Zang, S. P. Wong, I. H. Wilson, and S. K. Hark. Further evidence for the quantum confined electrochemistry model of the formation mechanism of p?type porous silicon.pdf. *Applied Physics Letters*, 69:3399–3401, 1996. doi: 10.1063/1.117272. URL http://apl.aip.org/resource/1/applab/v69/i22/p3399_s1?isAuthorized=no.

[132] R S Weis and T K Gaylord. Lithium niobate: Summary of physical properties and crystal structure. *Applied Physics A Solids and Surfaces*, 37(4):191–203, 1985. ISSN 07217250. doi: 10.1007/BF00614817. URL http://www.springerlink.com/index/g645525436r81w04.pdf.

[133] L Arizmendi. Photonic applications of lithium niobate crystals. *Physica Status Solidi A*, 201(2):253–283, 2004. ISSN 00318965. doi: 10.1002/pssa.200303911. URL http://doi.wiley.com/10.1002/pssa.200303911.

[134] Ed L Wooten, Karl M Kissa, Alfredo Yi-yan, Edmond J Murphy, Senior Member, Donald A Lafaw, Peter F Hallemeier, David Maack, Daniel V Attanasio, Daniel J Fritz, Gregory J Mcbrien, and Donald E Bossi. A Review of Lithium Niobate Modulators for Fiber-Optic Communications Systems. *IEEE Journal of Selected Topics in Quantum Electronics*, 6(1):69–82, 2000. doi: 10.1109/2944.826874. URL http://ieeexplore.ieee.org/xpl/login.jsp?tp=&arnumber=826874&url=http://ieeexplore.ieee.org/xpls/abs_all.jsp?arnumber=826874.

[135] H Lu, B Sadani, N Courjal, G Ulliac, N Smith, V Stenger, M Collet, F I Baida, and M-P Bernal. Enhanced electro-optical lithium niobate photonic crystal wire waveguide on a smart-cut thin film. *Optics express*, 20(3):2974–81, January 2012. ISSN 1094-4087. URL http://www.ncbi.nlm.nih.gov/pubmed/22330535.

[136] S Mailis, P G Lagoudakis, M Paturzo, J D Mills, J Feldmann, and R W Eason. Second harmonic generation enhancement in lithium niobate micro-tips. *America*, pages 60–62, 2005. URL http://eprints.soton.ac.uk/65765/.

[137] C Y J Ying, G S Murugan, G Brambilla, C L Sones, E Soergel, J S Wilkinson, R W Eason, M N Zervas, and S Mailis. Surface tension reshaped lithium niobate whispering gallery mode micro-resonators. *CLEO 2011 Laser Science to Photonic Applications*, pages 1–2, 2011.

[138] Feng Chen. Photonic guiding structures in lithium niobate crystals produced by energetic ion beams. *Journal of Applied Physics*, 106(8):081101, 2009. ISSN 00218979. doi: 10.1063/1.3216517. URL http://link.aip.org/link/JAPIAU/v106/i8/p081101/s1&Agg=doi.

[139] Tzyy-Jiann Wang Tzyy-Jiann Wang and Chia-Hong Chu Chia-Hong Chu. Wavelength-Tunable Microring Resonator on Lithium Niobate, 2007. ISSN 10411135. URL http://ieeexplore.ieee.org/lpdocs/epic03/wrapper.htm?arnumber=4383199.

[140] Andrea Guarino, Gorazd Poberaj, Daniele Rezzonico, Riccardo Degl'Innocenti, and Peter Günter. Electrooptically tunable microring resonators in lithium niobate. *Nature Photonics*, 1(7):407–410, July 2007. ISSN 1749-4885. doi: 10.1038/nphoton.2007.93. URL http://www.nature.com/doifinder/10.1038/nphoton.2007.93.

[141] M Levy, R M Osgood, R Liu, L E Cross, G S Cargill, A Kumar, and H Bakhru. Fabrication of single-crystal lithium niobate films by crystal ion slicing. *Applied Physics Letters*, 73(16):2293, 1998. ISSN 00036951. doi: 10.1063/1.121801. URL http://link.aip.org/link/APPLAB/v73/i16/p2293/s1&Agg=doi.

[142] Manuel Koechlin, Frederik Sulser, Zlatko Sitar, Gorazd Poberaj, and Peter Günter. Free-Standing Lithium Niobate Microring Resonators for Hybrid Integrated Optics. *IEEE Photonics Technology Letters*, 22(4):251–253, 2010. doi: 10.1109/LPT.2009.2038174. URL http://ieeexplore.ieee.org/xpl/login.jsp?tp=&arnumber=5378532&url=http://ieeexplore.ieee.org/xpls/abs_all.jsp?arnumber=5378532.

[143] G Nunzi Conti, S Berneschi, F Cosi, S Pelli, S Soria, G C Righini, M Dispenza, and A Secchi. Planar coupling to high-Q lithium niobate disk resonators.

Optics Express, 19(4):3651–3656, 2011. doi: 10.1364/OE.19.003651. URL http://www.ncbi.nlm.nih.gov/pubmed/21369190.

[144] G. L. Destefanis, P. D. Townsend, and J. P. Gailliard. Optical waveguides in LiNbO3 formed by ion implantation of helium. *Applied Physics Letters*, 32(5):293, 1978. ISSN 00036951. doi: 10.1063/1.90025. URL http://link.aip.org/link/APPLAB/v32/i5/p293/s1&Agg=doi.

[145] G. L. Destefanis, J. P. Gailliard, E. L. Ligeon, S. Valette, B. W. Farmery, P. D. Townsend, and a. Perez. The formation of waveguides and modulators in LiNbO3 by ion implantation. *Journal of Applied Physics*, 50(12):7898, 1979. ISSN 00218979. doi: 10.1063/1.325982. URL http://link.aip.org/link/JAPIAU/v50/i12/p7898/s1&Agg=doi.

[146] Jon Orloff. Fundamental limits to imaging resolution for focused ion beams. *Journal of Vacuum Science & Technology B: Microelectronics and Nanometer Structures*, 14(6):3759, November 1996. ISSN 0734211X. doi: 10.1116/1.588663. URL http://link.aip.org/link/?JVB/14/3759/1&Agg=doi.

[147] H Hu, A P Milenin, R B Wehrspohn, H Hermann, and W Sohler. Plasma etching of proton-exchanged lithium niobate. *Journal of Vacuum Science Technology A Vacuum Surfaces and Films*, 24(4):1012, 2006. ISSN 07342101. doi: 10.1116/1.2207150. URL http://link.aip.org/link/JVTAD6/v24/i4/p1012/s1&Agg=doi.

[148] Deng Jun, Jia Wei, Ching Eng Png, Si Guangyuan, Jaesung Son, Hyunsoo Yang, and Aaron J. Danner. Deep anisotropic LiNbO3 etching with SF6/Ar inductively coupled plasmas. *Journal of Vacuum Science & Technology B: Microelectronics and Nanometer Structures*, 30(1):011208, 2012. ISSN 21662746. doi: 10.1116/1.3674282. URL http://link.aip.org/link/JVTBD9/v30/i1/p011208/s1&Agg=doi.

[149] Barbara a. Fairchild, Paolo Olivero, Sergey Rubanov, Andrew D. Greentree, Felix Waldermann, Robert a. Taylor, Ian Walmsley, Jason M. Smith, Shane Huntington, Brant C. Gibson, David N. Jamieson, and Steven Prawer. Fabrication of Ultrathin Single-Crystal Diamond Membranes. *Advanced Materials*, 20(24):4793–4798, December 2008. ISSN 09359648. doi: 10.1002/adma.200801460. URL http://doi.wiley.com/10.1002/adma.200801460.

[150] S.E Coe and R.S Sussmann. Optical, thermal and mechanical properties of CVD diamond. *Diamond and Related Materials*, 9(9-10):1726–1729, September 2000. ISSN 09259635. doi: 10.1016/S0925-9635(00)00298-3. URL http://linkinghub.elsevier.com/retrieve/pii/S0925963500002983.

[151] Qi Liang, Chih-Shiue Yan, Yufei Meng, Joseph Lai, Szczesny Krasnicki, Ho-Kwang Mao, and Russell J Hemley. Enhancing the mechanical properties of single-crystal CVD diamond. *Journal of physics Condensed matter an Institute of Physics journal*, 21(36):364215, 2009. URL http://stacks.iop.org/0953-8984/21/i=36/a=364215?key=crossref.7b563f40a177b074f5cf1818e5aea712.

[152] C E Nebel. Electronic properties of CVD diamond. *Semiconductor Science and Technology*, 18(3):S1–S11, 2003. ISSN 02681242. doi: 10.1088/0268-1242/18/3/301. URL http://stacks.iop.org/0268-1242/18/i=3/a=301?key=crossref.f5756e9f7f380746877c267e536471f7.

[153] Keith A Snail. Growth, processing and properties of CVD diamond for optical applications. *Optical Materials*, 1(4):235–258, 1992. ISSN 09253467. doi: 10.1016/j.optmat.2011.09.008. URL http://www.sciencedirect.com/science/article/B6TXP-46X4M90-1/2/0d5e1179ef99f0cfd3a068a747e3dd87.

[154] R S Balmer, J R Brandon, S L Clewes, H K Dhillon, J M Dodson, I Friel, P N Inglis, T D Madgwick, M L Markham, T P Mollart, N Perkins, G A Scarsbrook, D J Twitchen, A J Whitehead, J J Wilman, and S M Woollard. Chemical vapour deposition synthetic diamond: materials, technology and applications. *Journal of physics Condensed matter an Institute of Physics journal*, 21(36):364221, 2009. URL http://arxiv.org/abs/0909.1185.

[155] David S Dandy. DIAMOND CHEMICAL VAPOR DEPOSITION Nucleation and Early Growth Stages by. *Journal of Materials Research*, 07656(201): 3001–3009, 1995. ISSN 08842914. doi: 10.1557/JMR.1992.3001. URL http://books.google.com/books?id=FISeqXLmltIC.

[156] Yinan Zhang Tom M. Babinec Katie Martinick Murray McCutheon Phil R. Hemmer Marko Loncar Birgit J M HBirgit, Mughees Khan. Fabrication of diamond nnanowire for quantum information procesing applications. *Diamon & Related Materials*, 19:621–629, 2010.

[157] Birgit J M Hausmann, Thomas M Babinec, Jennifer T Choy, Jonathan S Hodges, Sungkun Hong, Irfan Bulu, Amir Yacoby, Mikhail D Lukin, and Marko Lončar. Single-color centers implanted in diamond nanostructures. *New Journal of Physics*, 13(4):045004, 2011. ISSN 13672630. doi: 10.1088/1367-2630/13/4/045004. URL http://stacks.iop.org/1367-2630/13/i=4/a=045004?key=crossref.a3c4d3da673b10b9522f2cdb777f306e.

[158] Mark P Hiscocks, Kumaravelu Ganesan, Brant C Gibson, Shane T Huntington, François Ladouceur, and Steven Prawer. Diamond waveguides fabricated by reactive ion etching. *Optics express*, 16(24):19512–9, November 2008. ISSN 1094-4087. URL http://www.ncbi.nlm.nih.gov/pubmed/19030037.

[159] Thomas M Babinec, Birgit J M Hausmann, Mughees Khan, Yinan Zhang, Jeronimo R Maze, Philip R Hemmer, and Marko Loncar. A diamond nanowire single-photon source. *Nature Nanotechnology*, 5(3):195–199, 2010. URL http://www.ncbi.nlm.nih.gov/pubmed/20154687.

[160] S. Lagomarsino, P. Olivero, F. Bosia, M. Vannoni, S. Calusi, L. Giuntini, and M. Massi. Evidence of Light Guiding in Ion-Implanted Diamond. *Physical Review Letters*, 105(23):233903–, December 2010. ISSN 0031-9007. doi: 10.1103/PhysRevLett.105.233903. URL http://link.aps.org/doi/10.1103/PhysRevLett.105.233903.

[161] Gemesis Diamond Company: Lab-Created Diamond Jewelry. URL http://gemesis.com/.

[162] P Olivero, S Rubanov, P Reichart, B Gibson, S Huntington, J Rabeau, A Greentree, J Salzman, D Moore, and D Jamieson. Characterization of three-dimensional microstructures in single-crystal diamond. *Diamond and Related Materials*, 15(10):1614–1621, 2006. ISSN 09259635. doi: 10.1016/j.diamond.2006.01.018. URL http://linkinghub.elsevier.com/retrieve/pii/S0925963506000227.

[163] C Uzan-Saguy, C Cytermann, R Brener, V Richter, M Shaanan, and R Kalish. Damage threshold for ion-beam induced graphitization of diamond. *Applied Physics Letters*, 67(9):1194, 1995. ISSN 00036951. doi: 10.1063/1.115004. URL http://link.aip.org/link/APPLAB/v67/i9/p1194/s1&Agg=doi.

[164] S. Azimi M. B. H. Breese J. Forneris J. Song, Z. Y. Dang and E. Vittone. On the formation of 50 nm diameter free-standing silicon wires produced by ion

irradiation. *ECS Journal of Solid State Science and Technology*, 1:P66–P69, 2012.

[165] B Naydenov, R Kolesov, A Batalov, J Meijer, S Pezzagna, D Rogalla, F Jelezko, and J Wrachtrup. Engineering single photon emitters by ion implantation in diamond. *Applied Physics Letters*, 95(18):181109, 2009. URL http://www.pubmedcentral.nih.gov/articlerender.fcgi?artid=2787064&tool=pmcentrez&rendertype=abstract.

[166] A M Zaitsev. *Optical properties of diamond: a data handbook*, volume 42. Springer, 2001. ISBN 354066582X. URL http://books.google.co.uk/books?id=msU4jkdCEhIC.

[167] S Lagomarsino, P Olivero, S Calusi, D Gatto Monticone, L Giuntini, M Massi, S Sciortino, A Sytchkova, A Sordini, and M Vannoni. Complex refractive index variation in proton-damaged diamond. *Optics express*, 20(17):19382–94, August 2012. ISSN 1094-4087. doi: 10.1364/OE.20.019382. URL http://www.opticsinfobase.org/oe/abstract.cfm?uri=oe-20-17-19382.

[168] Antonio Benayas, Ningning Dong, Yicun Yao, Feng Chen, Andrew Anthony Bettiol, and Daniel Jaque. Thermal optimization and erasing of Nd:YAG proton beam written waveguides. *Optics Letters*, 36(16):3278–3280, 2011. doi: 10.1364/OL.36.003278. URL http://www.ncbi.nlm.nih.gov/pubmed/21847233.

[169] S. Calusi L. Giuntini, M. Massi. The external scanning proton microprobe of firenze: A comprehensive description. *Nuclear Instruments and Methods in Physics Research Section A*, 576:266–273, 2007.

[170] Christos Grivas. Optically pumped planar waveguide lasers, part I: fundamentals and fabrication techniques. *Progress in Quantum Electronics*, 35(6):159–239, 2011. URL http://eprints.soton.ac.uk/201069/.

[171] D Kip. Photorefractive waveguides in oxide crystals: fabrication, properties, and applications. *Applied Physics B Lasers and Optics*, 67(2):131–150, 1998. ISSN 09462171. doi: 10.1007/s003400050485. URL http://www.springerlink.com/openurl.asp?genre=article&id=doi:10.1007/s003400050485.

[172] Andreas Jechow, Marco Schedel, Sandra Stry, Joachim Sacher, and Ralf Menzel. Highly efficient single-pass frequency doubling of a continuous-wave distributed feedback laser diode using a PPLN waveguide crystal at 488 nm. *Optics Letters*, 32(20):3035–3037, 2007. URL `http://www.ncbi.nlm.nih.gov/pubmed/17938691`.

[173] Yicun Yao, Yang Tan, Ningning Dong, Feng Chen, and Andrew A Bettiol. Continuous wave Nd:YAG channel waveguide laser produced by focused proton beam writing. *Optics Express*, 18(24):24516–24521, 2010. doi: 10.1364/OE.18.024516. URL `http://www.ncbi.nlm.nih.gov/pubmed/21164799`.

[174] S J Field, D C Hanna, A C Large, D P Shepherd, A C Tropper, P J Chandler, P D Townsend, and L Zhang. Ion-implanted Nd:GGG channel waveguide laser. *Optics Letters*, 17(1):52–54, 1992. URL `http://eprints.soton.ac.uk/78543/`.

[175] Yingying Ren Yingying Ren, Ningning Dong Ningning Dong, Yang Tan Yang Tan, Jing Guan Jing Guan, Feng Chen Feng Chen, and Qingming Lu Qingming Lu. Continuous Wave Laser Generation in Proton Implanted Nd:GGG Planar Waveguides, 2010. ISSN 07338724.

[176] William Paul Risk, Timothy R Gosnell, and Arto V Nurmikko. *Compact blue-green lasers*, volume 57. Cambridge University Press, 2003. ISBN 0521521033. doi: 10.1063/1.1688074. URL `http://books.google.com/books?id=rtLwj5H9JacC&pgis=1`.

[177] Chang-long Zhang, Ling-xiong Huang, Wei-ning Zhou, Ge Zhang, Han-de Hou, Qing-feng Ruan, Wei Lei, Shi-jie Qin, Fu-hua Lu, Yan-bin Zuo, Hong-yuan Shen, and Guo-fu Wang. Growth of KTP crystals with high damage threshold by hydrothermal method. *Journal of Crystal Growth*, 292(2):364–367, 2006. ISSN 00220248. doi: 10.1016/j.jcrysgro.2006.04.036. URL `http://linkinghub.elsevier.com/retrieve/pii/S002202480600354X`.

[178] O I Lavrovskaya. Effective non-linear second-order coefficient d(eff) for the type II interaction in KTP crystal. *Applied Optics*, 30(27):3790, 1991. doi: 10.1364/AO.30.003790.

[179] I Savatinova, I Savova, E Liarokapis, C C Ziling, V V Atuchin, M N Armenise, and V M N Passaro. A comparative analysis of Rb:KTP and Cs:KTP optical waveguides. *Journal of Physics D: Applied Physics*, 31(14):1667–1672, July

1998. ISSN 0022-3727. doi: 10.1088/0022-3727/31/14/009. URL http://iopscience.iop.org.libproxy1.nus.edu.sg/0022-3727/31/14/009.

[180] Feng Chen, Yang Tan, Lei Wang, Dong-Chao Hou, and Qing-Ming Lu. Optical channel waveguides with trapezoidal-shaped cross sections in KTiOPO4 crystal fabricated by ion implantation. *Applied Surface Science*, 254(6):1822–1824, January 2008. ISSN 01694332. doi: 10.1016/j.apsusc.2007.07.160. URL http://dx.doi.org/10.1016/j.apsusc.2007.07.160.

[181] Ningning Dong, Daniel Jaque, Feng Chen, and Qingming Lu. Second harmonic and raman imaging of He+ implanted KTiOPO4 waveguides. *Optics Express*, 19(15):13934–9, 2011. ISSN 10944087. URL http://www.ncbi.nlm.nih.gov/pubmed/21934753.

[182] Zheng Gang Lian, Weijian Pan, David Furniss, Trevor M Benson, Angela B Seddon, Tomas Kohoutek, Jiri Orava, and Tomas Wagner. Femtosecond laser writing of multifunctional optical waveguides in a Nd:YVO4 + KTP hybrid system. *Optics Letters*, 36(6):1234–1236, 2011. doi: 10.1364/OL.36.000975. URL http://www.ncbi.nlm.nih.gov/pubmed/21403747.

[183] J. Siebenmorgen, K. Petermann, G. Huber, K. Rademaker, S. Nolte, and A. Tünnermann. Femtosecond laser written stress-induced Nd:Y3Al5O12 (Nd:YAG) channel waveguide laser. *Applied Physics B*, 97(2):251–255, September 2009. ISSN 0946-2171. doi: 10.1007/s00340-009-3697-3. URL http://www.springerlink.com/index/10.1007/s00340-009-3697-3.

[184] A R Md Zain, N Johnson, M Sorel, and R M De La Rue. Ultra high quality factor one dimensional photonic crystal/photonic wire micro-cavities in silicon-on-insulator (SOI). *Optics Express*, 16(16):12084–12089, 2008. URL http://dx.doi.org/10.1364/OE.16.012084.

Appendix A

List of Publications

1. *"A microfluidic chip with integrated colloidal crystal for online optical analysis"* Siew-Kit Hoi, Xiao Chen, **Vanga S. Kumar**, Sureerat Homhuan, Chorng-Haur Sow and Andrew A. Bettiol Advanced Functional Materials 21 (2011) 2847-2853, DOI: 10.1002/adfm.201002632.

2. *"Proton beam writing of long, arbitrary structures for micro/nano photonics and fluidics applications"* Chammika Udalagama, E.J. Teo, S.F. Chan, **V.S. Kumar**, A.A. Bettiol, F. Watt Nuclear Instruments & Methods in Physics Research B 269 (2011) 2417-2421, DOI: 10.1016/j.nimb.2011.02.051.

3. *"Proton beam writing of Nd:GGG crystals as new waveguide laser sources"* Yicun Yao, Ningning Dong, Feng Chen, **Sudheer Kumar Vanga** and Andrew Anthony Bettiol, Optics Letters 36 (2011) 4173-4175, DOI: 10.1364/OL.36.004173.

4. *"Buried channel waveguides in KTiOPO4 nonlinear crystal fabricated by focused He+ beam writing"* Ningning Dong, Yicun Yao, Yuechen Jia, Feng Chen, **Sudheer Kumar Vanga**, Andrew Anthony Bettiol, Qingming Lu, Optical Materials 35-2 (2012) 184-186, http://dx.doi.org/10.1016/j.optmat.2012.07.007.

5. *"Fabrication of optical microresonators using proton beam writing"* **Vanga Sudheer Kumar**, Shuvan Prashant Turaga, Ee Jin Teo, Andrew A. Bettiol, Microelectronic Engineering 102 (2013) 33-35, http://dx.doi.org/10.1016/j.mee.2012.02.017.

6. *"Optical microcavities fabricated using direct proton beam writing"*, **Sudheer Kumar Vanga**, Shuvan Prashant Turaga, Ee Jin Teo and Andrew Bettiol, Proceedings of the SPIE - The International Society for Optical Engineering, v 8249, 824918 (7 pp.) (2012), DOI: 10.1117/12.908319.

7. *"Ion beam irradiation induced fabrication of vertical coupling waveguides"* Haidong Liang, **Sudheer Kumar Vanga**, Jianfeng Wu, and Mark Breese, Appl. Phys. Lett. 102, 131112 (2013), http://link.aip.org/link/doi/10.1063/1.4801307.

8. *"Modeling and experimental investigations of Fano resonances in free-standing LiNbO3 photonic crystal slabs"* Jun Deng, Sajid Hussain, **Vanga Sudheer Kumar**, Wei Jia, Ching Eng Png, Lim Soon Thor, Andrew A. Bettiol, and Aaron J. Danner, Optics Express, Vol. 21, Issue 3, pp. 3243-3252 (2013), http://dx.doi.org/10.1364/OE.21.003243.

9. *"Free-standing Monolithic LiNbO3 Photonic Crystal Slabs"* Deng Jun, **Sudheer Kumar Vanga** , Sajid Hussian, Gao Hongwei, Lim Soon Thor, Ching Eng Png, Xiang Ning, Andrew A. Bettiol, and Aaron J. Danner Proceeding of the SPIE, v 8632 (2013) DOI:10.1117/12.2004085.

10. *"Proton beam writing of three-dimensional microcavities"* **Sudheer Kumar Vanga**, Andrew Bettiol, NIMB (2013), http://dx.doi.org/10.1016/j.nimb.2012.12.058 (in press).

11. *"Three-dimensional metamaterials fabricated using proton beam writing"*, A. A. Bettiol, S. P. Turaga, Y. Yan, S. K. Vanga, and S. Y. Chiam, NIMB (2013), http://dx.doi.org/10.1016/j.nimb.2012.11.050 (in press).

Appendix B

Typical PBW procedure at CIBA

Turn on the accelerator

- Turn on the GVM and drive motor to get the accelerator voltage.
- Turn on the cooling system for the analyzing and the switching magnet.
- Increase the terminal voltage to the desired value of operation and introduce the gas into the ion source.
- Apply probe and extraction voltages to extract the beam from the accelerator system.

Target chamber preparation

- Attach the samples to the target holder along with the Ni grid and quartz sample. The quartz sample to locate the beam from its luminescence and observation of focusing, the Ni grid for measuring the beam spot size.
- Check the sample under microscope to record the height difference between the sample and the Ni grid. This is to move the sample to the beam focus during irradiation.
- Load the sample into the target chamber and pump down the chamber to 1.8×10^{-5} mbar pressure inside the chamber.

- Once the pressure in the chamber reached the desired value, turn the stage controller ON and open the IonScan software to move the stage to a metal to avoid unwanted irradiation of proton beam on the sample.
- Open the valves after the switching magnet and before the target chamber and connect the target current meter (pA) to observe the current in the chamber.

Obtain the beam in Target chamber

- Once the optimum pressure reached set the X and Y steerer currents to optimize the beam current by observing the beam current from Faraday cup 1.
- Apply current to 90° magnet to turn the beam normal to the the initial beam path and also to select the proton (H^+) or molecular beam(H_2^+). Apply current to switcher magnet to switch the to the desired beamline of operation.
- Obtain the maximum beam current in Faraday cup 2 by adjusting the 90° magnet and the magnetic steerer settings.
- Observe the beam profile monitor to align the beam in the centre of the beamline.
- Set the switcher magnet current value to select the 10° beamline.
- Observe the current in target current meter (pA) and adjust the switcher magnet current to obtain the beam in the chamber and observe the beam using oscilloscope to minimize the electronic noise in the system.

Focusing the proton beam

- Adjust the objective and collimator slits to reduce the current and select the maximum intensity region of the beam.
- Adjust the beam steering using collimator slits by observing the beam on the quartz.
- Focus the beam visually with the quadruple magnet current.
- Reduce the beam current to less than 1 pA and turn on the CEM detector and the beam blanking system.

- Move the beam onto the grid and turn on the scan amplifier.
- Adjust the magnetic quadrupole currents precisely by focusing the smallest size grid.
- Obtain the beam focus less than 100 nm in both lateral and vertical directions by adjusting the quadrupole magnet currents and the slits (usually an opening of 3 $\mu m \times 1$ μm objective slits and 150 $\mu m \times 150$ μm collimator slits) .
- Now perform the scan calibration by moving the stage in precise step of 10 μm, measuring the displacement of the grid image from its focus and by adjusting the scan parameters to obtain the same 10 μm displacement in both X and Y directions.

Dose Normalization

- Turn off the CEM detector and turn on the RBS detector and set bias of 20 V to the detector. Obtain the RBS spectrum on the sample and fit the spectrum using SIMNRA software package to obtain the incident number of particles.

Writing procedure

- Note the sample position and select the coordinates for beam irradiation.
- Load the .epl file into the IonScan software to calculate the update time for the irradiation.
- Correct the stage position to make the sample in the beam focused spot (adjust the Z position).
- Prepare the batch files with .els extension and load into the EPL exposure window and start scanning the desired patterns.

Appendix C

MATLAB Files

Different cavities designs used was generated using the MATLAB and the code is given here for each cavity design. And to calculate the propagation loss from the scattered images collected from the Diamond waveguide was also done using MATLAB and the code is given in this section.

C.1 Spiral disk resonator design

```
% This m-file generates a bmp file for creating a spiral laser
% indicate the number of pixels in the figure size
% Tries to make a figure and then saves the bmp.

x_range =650;
y_range = 650;

h = figure('Position',[100,100,x_range,y_range]);

a = gca;
axis([-x_range/2 x_range/2 -y_range/2 y_range/2]);
set(a,'Position',[0,0, 1, 1]);
set(a,'XTick',[],'YTick',[]) ;

spacing= 0.01;
phi = 0:spacing:2*pi;  % The angle
```

```
r0 = 300;               % Initial radius
epsilon = 0.1;          % Deformity parameter
%The equation for defining the spiral laser
r = r0.*(1 + epsilon/( 2*pi).*phi);


% polar(phi,r,'.');
% in cartesian coordinates
x = r.*cos(phi);
y = r.*sin(phi);
x(end+1) = x(1);
y(end+1) = y(1);
h1 = fill(x,y,'k');
set(a,'XTick',[],'YTick',[]) ;
I = getframe(h);
imwrite(I.cdata,'saveme.bmp','bmp');
```

C.2 Design file for Elliptical cavity with notch at the middle

```
% This Program makes the elliptical laser from inside out
% generates the co-ordinates for the pbeam
% to make the structure

clear ;
clc
% phi = 0 ;
ri= 1;
figure;
hold on;
x0 = 0;
y0 = 0;
xf = x0;
yf = y0;
```

```
filename = input('Enter the filename','s');
filename = strcat(filename,'.txt');
fid = fopen(filename,'w');
while ri < r0
    for phi = 0:pi/100 :2*pi

    x = a.*cos(phi);
    y = b.*sin(phi);

     fprintf(fid,'%d,%d\n',x,y);
    x0 = x;
    y0 = y;

    end
   ri = ri+1;

end

wvg_len = 800;
x1=r0;

while(x1<r0+r0*epsilon)

     fprintf(fid,'%d,%d\n',x1,0);
     fprintf(fid,'%d,%d\n',x1,wvg_len);

     fprintf(fid,'%d,%d\n',x1,wvg_len);
     fprintf(fid,'%d,%d\n',x1,0);

     x1 = x1 + 1;
end;

fclose(fid);
```

C.3 Propagation loss measurement

```
clear all
I1 = imread('1.tif');
I2 = imread('2.tif');
I3 = imread('3.tif');
I4 = imread('4.tif');
I5 = imread('5.tif');
I6 = imread('6.tif');
I7 = imread('7.tif');
I8 = imread('8.tif');
I9 = imread('9.tif');
I10 = imread('10.tif');
Ibg = imread('bg.tif');
I1a = double(I1) + 1;
I2a = double(I2) + 1;
I3a = double(I3) + 1;
I4a = double(I4) + 1;
I5a = double(I5) + 1;
I6a = double(I6) + 1;
I7a = double(I7) + 1;
I8a = double(I8) + 1;
I9a = double(I9) + 1;
I10a = double(I10) + 1;
Ibga = double(Ibg)+1;
Xmin = 515;        % crop the rectangular section of the waveguide
Ymin = 230;        % with starting x, y position with width w and bredth h
w = 330;
h = 55;
I1b = imcrop(I1a, [Xmin Ymin w h]);
I2b = imcrop(I2a, [Xmin Ymin w h]);
I3b = imcrop(I3a, [Xmin Ymin w h]);
I4b = imcrop(I4a, [Xmin Ymin w h]);
I5b = imcrop(I5a, [Xmin Ymin w h]);
I6b = imcrop(I6a, [Xmin Ymin w h]);
I7b = imcrop(I7a, [Xmin Ymin w h]);
```

```
I8b = imcrop(I8a, [Xmin Ymin w h]);
I9b = imcrop(I9a, [Xmin Ymin w h]);
I10b = imcrop(I10a, [Xmin Ymin w h]);
Ibgb = imcrop(Ibga, [Xmin Ymin w h]);
for j = 1:w-1
 C1 = 0;
 C2 = 0;
 C3 = 0;
 C4 = 0;
 C5 = 0;
 C6 = 0;
 C7 = 0;
 C8 = 0;
 C9 = 0;
 C10 = 0;
 Cbg = 0;
for i = 1:h-1
    C1 = C1 + I1b(i,j);
    C2 = C2 + I2b(i,j);
    C3 = C3 + I3b(i,j);
    C4 = C4 + I4b(i,j);
    C5 = C5 + I5b(i,j);
    C6 = C6 + I6b(i,j);
    C7 = C7 + I7b(i,j);
    C8 = C8 + I8b(i,j);
    C9 = C9 + I9b(i,j);
    C10 = C10 + I10b(i,j);
    Cbg = Cbg +Ibgb(i,j);
end
C = (C1+C2+C3+C4+C5+C6+C7+C8+C9+C10-10*Cbg)./10;
Y(j,1) = 10*log10(C);
L(j,1) = j*(470/720)*1e-4;
end
% Calibration of length   907 um = 1317 pix
% 1 pix = 0.6886*e-4 cm
polyfit(L,Y,1)
```

```
plotedit on
plot(L,Y)
xlabel('Length(cm)'),ylabel('10logI'),title('Propagation Loss');
```